EPFL

Supercontinuum generation in silicon nitride (Si$_3$N$_4$) waveguides for middle infrared spectroscopy

Eirini TAGKOUDI

■ École
polytechnique
fédérale
de Lausanne

2021

To Leonidas

Acknowledgements

Many people contributed significantly and in different ways during my Ph.D. journey, some during the actual writing period and others on a much longer time scale, constantly supporting and encouraging me during these four and a half years.

First of all, I would like to express my sincere gratitude to my supervisor, Prof. Camille-Sophie Brès, for giving me the opportunity to work on a fascinating project in a multicultural environment and a prestigious university such as EPFL. I am grateful for being privileged to be part of your team and for all your support during my Ph.D. Apart from that, I want to thank you for being such a great mentor. You were always there for me, listening and guiding me. You always believed in me and kept my motivation high until the end of the journey.

I would also like to acknowledge Prof. Tobias Kippenberg from EPFL and Goëry Genty from the Tampere University of Finland for their valuable collaboration during these years and the insightful discussions.

My sincere thanks go to the president of the jury, Prof. Luc Thévenaz, and the jury members, Prof. Hatice Altug, Prof. Delphine Marris-Morini and Prof. Christelle Monat for taking the time to review my work and providing helpful comments and suggestions in my thesis.

Moreover, I would like to sincerely thank the post-docs I collaborated with: Dr. Davide Grassani, Dr. Fan Yang, and Dr. Caroline Amiot. You have taught me a lot while working with you, and I appreciate your valuable help in simulations. Specifically, I want to thank Caroline for our great discussions and our runs in the sunny winter days.

The former and current Photonic Systems Laboratory (PHOSL) members deserve to be acknowledged since I enjoyed working with them during my Ph.D. I want to thank Adrien, Boris, Davide, Edgars, Ezgi, Florent, Jianqi, Nikolay, Ozan, Sida, Simon, and Svyatoslav for our fruitful scientific conversations and the time spent together. Especially, I want to thank Moritz and Arman for our coffee breaks and our great discussions and Nikolay for his thoughtful chocolate gifts. I already miss our Friday nights, eating burgers and dancing Macarena after an exhausting day in the lab. Finally, I could not forget to thank our secretary, Françoise, for always helping me with every administrative issue and giving me great suggestions for weekend getaways in beautiful Switzerland.

I want to thank my officemate and very good friend, Ivan, separately. Since the first day I arrived at PHOSL, you have been a great support for me and a motivation to start running (better late than ever in this life!).

Acknowledgements

Finally, this part is dedicated to the most important people in my life. First and foremost, I want to thank my parents, Despoina and Vassilis, and my brother Apostolos for their unconditional love and support throughout my entire life. Without you supporting my choices and without your sacrifices, I wouldn't have reached that far in my studies and in my life.

Special thanks go to my partner, Leonidas – who, in the meantime, became my husband – for his love, his constant support, and patience. He is always standing by my side, cheering me up and giving me the courage to continue. Thank you for taking care of me, especially during the long run of this thesis's writing. It would not have been possible to make it without you. I can write so many things, but I feel that words are not enough to thank you. I am just so grateful we have been able to grow together through the years. I am looking forward to our new travel – and life – adventures, like our unforgettable trip to the USA and many other everyday moments!

My best friends in Greece: Maria, Georgia, and Vivi, deserve special mention. Companions to my journey since the first year of high school, were only just a phone call away. I appreciate your encouragement and tremendous support during all these years, and I feel very lucky to have you in my life. Best friends are the family we choose for ourselves, and you are my family.

Amalia and Aliki, thank you for being there for me, despite the distance and the different time zones separating us, for your huge support and encouragement during my entire studies.

Lastly, I would like to thank my close friends in Switzerland: Maya, Vicky, Natalie, Harry, and Matina. Thank you for the great moments we shared –and we will continue sharing, your constant support and your understanding. Particularly, I thank my very good friend Vicky for her everyday supportive messages that made me smile during the intense writing period.

I could not forget to thank my friend Kriton for all his help before and after my arrival in Lausanne, especially for his great hospitality during the very first days. I will never forget that.

Lisbon and Barcelona would have been unexplored without my travel buddies: Maya, Eirini, and Iliana. Thank you for the great moments we spent together. Traveling around Europe and exploring new places before the pandemic hit the earth is something I have missed a lot.

Eirini Tagkoudi

Gland, 23 May 2021

Abstract

The middle-infrared (mid-IR) spectral range (2 - 10 µm) hosts the most intense roto-vibrational absorption lines of many important molecules. Particularly, mid-IR spectroscopy constitutes a unique tool for identifying and quantifying molecular species through their mid-IR spectral "fingerprints." As a result, exploiting efficient ways to access the mid-IR is of paramount importance for spectroscopic applications and environmental monitoring.

Supercontinuum (SC) sources have been a common way to access this spectral region, using compact femtosecond fiber lasers and optical fibers as the broadening medium. However, in the past few years, emphasis has shifted towards compact SC sources based on integrated platforms. Among the different material platforms studied for the integration of SC generation, stoichiometric silicon nitride (Si_3N_4) is one of the most promising. With a transparency window extending from the visible to the mid-IR, CMOS compatibility, and a mature fabrication technology combined with flexibility in design, Si_3N_4 waveguides represent an attractive solution for on-chip SC generation.

This thesis's main aim is to develop a tunable mid-IR SC source based on Si_3N_4 waveguides that can efficiently reach the spectral region between 3 – 4 µm, enabling mid-IR spectroscopy experiments. Towards this goal, nonlinear SC dynamics based on anomalous and all-normal-dispersion (ANDi) pumping regimes are explored in different Si_3N_4 waveguide designs.

In the first part of the thesis, the design and development of a compact and tunable mid-IR source are presented. Starting from a turn-key femtosecond short-wave infrared (SWIR) fiber laser located in the anomalous dispersion regime of a SiO_2-cladded large cross-section Si_3N_4 waveguides, mid-IR soliton-induced dispersive waves (DWs) are generated. A synergy of the proper waveguide geometry and pump positioning enables favorable dispersion profiles towards the mid-IR, while suppressing the generation into the visible. Moreover, by switching to a waveguide with different dimensions, the DW can be tuned with lithographic precision between the entire 3 – 4 µm spectral region, reaching record efficiencies up to 35 %. The milliwatt output powers estimated for all generated mid-IR DWs guarantee their utilization in gas spectroscopy.

In the second part of the thesis, the application of the on-chip generated mid-IR source in direct absorption spectroscopy is demonstrated. The most efficient DW generated at 3.0 µm is used to detect acetylene (C_2H_2) through a long gas cell in a proof-of-principle spectroscopic experiment. However, due to the limited bandwidth of the DW, parallel gas detection is not possible using this scheme. By leveraging a waveguide that generates a

DW centered at 3.5 µm and fine-tuning the pump wavelength, a larger bandwidth of the DW source is achieved, enabling simultaneous detection of multiple gas-phase species. Using this broad mid-IR DW from a single Si_3N_4 waveguide, detection of acetylene (C_2H_2), methane (CH_4), and ethane (C_2H_6) has been successfully achieved, with hundreds of parts-per-million (ppm) detection limit.

Finally, an extremely polarization-sensitive SWIR SC source based on an air-cladded Si_3N_4 waveguide is studied. The waveguide is engineered to yield all-normal-dispersion (ANDi) at near-infrared (NIR) wavelengths for the transverse magnetic (TM) mode and anomalous dispersion regime for transverse electric (TE) mode excitation. A flat and highly coherent ANDi SC or an octave-spanning soliton-fission-driven SC source can be selectively generated by simply switching between the pump's polarization states. As a result, the SC has the potential for versatile applications, from broadband on-chip sensing to pulse compression.

Overall, this dissertation explores new capabilities of Si_3N_4 waveguides, even beyond the enhanced efficiency to the mid-IR. For the first time, on-chip generated mid-IR DW is used as a tool for driving spectroscopy.

Keywords

Résumé

Le domaine spectral de l'infrarouge moyen (2 - 10 µm) abrite les lignes d'absorption roto-vibrationnelles les plus intenses de nombreuses importantes molécules. En particulier, la spectroscopie dans l'infrarouge moyen constitue un outil unique pour identifier et quantifier les espèces moléculaires grâce à leurs "empreintes" spectrales dans l'infrarouge moyen. Par conséquent, l'exploitation de moyens efficaces pour accéder à l'infrarouge moyen est d'une importance capitale pour les applications spectroscopiques et la surveillance de l'environnement.

Les sources supercontinuum (SC) ont été un moyen courant d'accéder à cette région spectrale, en utilisant des lasers fibrés compacts délivrant des impulsions femtoseconde et des fibres optiques comme moyen d'élargissement spectral. Cependant, au cours des dernières années, l'accent a été mis sur les sources SC plus compactes basées sur des plateformes intégrées. Parmi les différentes plateformes de matériaux étudiées pour l'intégration de la génération de SC, le nitrure de silicium stœchiométrique (Si_3N_4) est l'un des plus prometteurs. Avec une fenêtre de transparence s'étendant du visible à l'infrarouge moyen, une compatibilité CMOS, et une technologie de fabrication mature combinée à une flexibilité dans la conception, les guides d'ondes Si_3N_4 représentent une solution attractive pour la génération de SC sur puce.

L'objectif principal de cette thèse est de développer une source SC accordable dans l'infrarouge moyen basée sur des guides d'ondes Si_3N_4 qui peuvent atteindre efficacement la région spectrale entre 3 et 4 µm, permettant des expériences de spectroscopie dans l'infrarouge moyen. Dans ce but, la dynamique non linéaire de SC basé sur les régimes de pompage en dispersion anormale et normale (ANDi) est explorée dans différentes conceptions de guides d'ondes Si_3N_4.

Dans la première partie de la thèse, la conception et le développement d'une source compacte et accordable dans l'infrarouge moyen sont présentés. À partir d'un puits laser à fibre infrarouge à ondes courtes (SWIR) femtoseconde clé en main situé dans le régime de dispersion anormale d'un guide d'ondes Si_3N_4 à grande section transversale revêtu de SiO_2, des ondes dispersives (ODs) induites par des solitons dans l'infrarouge moyen sont générées. Une synergie entre la géométrie appropriée du guide d'ondes et le positionnement de la pompe permet d'obtenir des profils de dispersion favorables vers l'infrarouge moyen tout en supprimant la génération dans le visible. De plus, en passant à un guide d'ondes de dimensions différentes, l'OD peut être réglée avec une précision lithographique entre toute la région spectrale de 3 - 4 µm, atteignant des efficacités record jusqu'à 35 %. Les puissances de sortie en milliwatt estimées pour toutes les ODs générées dans l'infrarouge moyen garantissent leur utilisation en spectroscopie de gaz.

Dans la deuxième partie de la thèse, l'application de la source mid-IR générée sur puce en spectroscopie d'absorption directe est démontrée. L'OD la plus efficace générée à 3.0 µm est utilisée pour détecter de l'acétylène (C_2H_2) à travers une longue cellule de gaz dans une expérience spectroscopique. Cependant, en raison de la largeur de bande limitée de l'OD, la détection simultanée de différents gaz n'est pas possible avec cette configuration. En utilisant un guide d'ondes qui génère une OD centrée à 3.5 µm et en ajustant finement la longueur d'onde de la pompe, une plus grande largeur de bande de l'OD est obtenue, permettant la détection simultanée de plusieurs espèces en phase gazeuse. En utilisant cette large OD dans l'infrarouge moyen à partir d'un seul guide d'ondes Si_3N_4, la détection de l'acétylène, du méthane (CH_4) et de l'éthane (C_2H_6) a été réalisée avec succès, avec une limite de détection de centaines de parties par million (ppm).

Enfin, une source SC SWIR extrêmement sensible à la polarisation basée sur un guide d'ondes Si_3N_4 recouvert d'air est étudiée. Le guide d'ondes est conçu pour produire un régime de dispersion normale (ANDi) aux longueurs d'onde du proche infrarouge (NIR) pour le mode magnétique transverse (TM) et un régime de dispersion anormale pour l'excitation du mode électrique transverse (TE). En passant simplement la pompe d'un état de polarisation à l'autre, il est possible de générer sélectivement une source SC ANDi plate et hautement cohérente ou une source SC générée par fission solitonique s'étendant sur une octave. Par conséquent, le SC a le potentiel pour des applications polyvalentes, de la détection à large bande sur puce à la compression d'impulsions.

Dans l'ensemble, cette thèse explore les nouvelles capacités des guides d'ondes Si_3N_4, même au-delà de l'efficacité améliorée dans l'infrarouge moyen. Pour la première fois, l'OD dans l'IR moyen sur puce est utilisée comme outil de spectroscopie.

Mots-clés

Génération de supercontinuum (SCG), ondes dispersives (ODs), optique non linéaire, ingénierie de la dispersion, guides d'ondes en nitrure de silicium (Si_3N_4), photonique intégrée, infrarouge moyen (mid-IR), spectroscopie d'absorption mid-IR, détection d'un seul gaz, détection simultanée de gaz

Contents

Contents

List of publications

Peer-reviewed journal articles

- **E.Tagkoudi,** C.G.Amiot, G.Genty, C.S.Brès, "Extreme polarization-dependent supercontinuum generation in an uncladded silicon nitride waveguide," **Optics Express**, vol. 29, issue 14, pp. 21348-21357, (2021)

- **E. Tagkoudi**, D.Grassani, F.Yang, C.Herkommer, T.J.Kippenberg, C.S.Brès, "Parallel gas spectroscopy using mid-infrared supercontinuum from a single Si_3N_4 waveguide," **Optics Letters**, vol. 45, issue 8, pp. 2195-2198, (2020)

- D.Grassani, **E.Tagkoudi**, H.Guo, C.Herkommer, F.Yang, T.J.Kippenberg, C.S.Brès "Mid infrared gas spectroscopy using efficient fiber laser driven photonic chip-based supercontinuum," **Nature Communications** vol. 10, no.1553, (2019)

Conference proceedings

- **E.Tagkoudi,** C.G.Amiot, G.Genty, C.S.Brès, "Extreme polarization-dependent infrared supercontinuum generation in uncladded silicon nitride waveguide," CLEO-Europe, (2021).
- **E. Tagkoudi** D.Grassani, F.Yang, C.Herkommer, T.J.Kippenberg, C.S.Brès, "*Multi-gas spectroscopy using tailored mid-IR dispersive wave generated in Si_3N_4 waveguide,*" High-brightness Sources and Light-driven Interactions Congress, paper MF1C.3. (2020)
- **E. Tagkoudi** D.Grassani, F.Yang, C.Herkommer, T.J.Kippenberg, C.S.Brès, "*Gas Spectroscopy Using Low Threshold Mid-Infrared Radiation Generated in Si_3N_4 Waveguides,*" Conference on Lasers and Electro-Optics (CLEO), San Jose, CA, U.S.A., paper STh1F.4., (2019)
- **E. Tagkoudi** D.Grassani, C.Herkommer, T.J.Kippenberg, C.S.Brès "*Efficient mid-infrared dispersive wave generation in dispersion-engineered Si_3N_4 waveguides pumped at 2 µm,*" *Conference on Lasers and Electro-Optics (CLEO),* San Jose, CA, U.S.A., paper SW3A.8. (2018)

List of figures

List of tables

Acronyms

ANDi: All-normal dispersion

CE: Conversion efficiency

CEO: Carrier-envelope offset

CEP: Carrier-envelope phase

CMOS: Complementary metal-oxide-semiconductor

DFG: Difference frequency generation

DW: Dispersive wave

DWG: Dispersive wave generation

EM: Electro-magnetic

FEM: Finite-element method

FT-OSA: Fourier-transform optical spectrum analyzer

FWHM: Full-width at half maximum

GNLSE: Generalized nonlinear Schrödinger equation

GVD: Group velocity dispersion

HITRAN: High-resolution transmission

HOD: High-order dispersion

HWP: Half wave plate

ICL: Interband cascade laser

IR: Infrared

LED: Light-emitting diode

LPCVD: Low-pressure chemical vapor deposition

LTO: Low-temperature oxide

MFD: Mode field diameter

MLL: Mode-locked laser

MMF: Multimode fiber

OFC: Optical frequency comb

OPO: Optical parametric oscillator

OSA: Optical spectrum analyzer

OWB: Optical wave breaking

QCL: Quantum cascade laser

QWP: Quarter wave plate

SC: Supercontinuum

SCG: Supercontinuum generation

SNR: Signal-to-noise ratio

SPM: Self-phase modulation

SRS: Stimulated Raman scattering

SWIR: Short-wave infrared

TE: Transverse electric

TM: Transverse magnetic

TOD: Third-order dispersion

TPA: Two-photon absorption

UV: Ultra-violet

VOA: Variable optical attenuator

ZDW: Zero dispersion wavelength

Chapter 1

Introduction

Introduction

1.1 Thesis Motivation

The middle-infrared (mid-IR) spectral region (2–20 µm) of the electromagnetic (EM) spectrum has attracted significant attention because it hosts characteristic molecular absorption lines which correspond to the fundamental vibrational and rotational energy transitions of many molecules [1,2]. A plethora of important organic and inorganic molecules appear to have orders of magnitude stronger absorption lines lying into the mid-IR compared to their overtone transitions in the visible and near-IR spectral regions, enabling easier identification through their mid-IR absorption spectra. The characteristic resonant wavelengths which appear in the spectrum under illumination correspond to the transition energies of vibrating bonds or a group of bonds [2–4]. Fig. 1.1 displays the absorption spectra of some of the most important gas molecules in the mid-IR spectral region between 2 and 16 µm [4]. Mid-IR absorption lines of molecules – also known as molecular "fingerprints" – need to be identified and quantified accurately, especially when they originate from greenhouse gases and other air pollutants [5,6], hazardous vapors [7,8], or gases emitted by cancer cells [9,10]. Therefore, the mid-IR region possesses significant technological importance for molecular gas spectroscopy and biological sensing applications [11,12]. Characteristic examples of applications concerning mid-IR include indoor [13,14] and outdoor [15] environmental monitoring, security [15–17], food quality control [18–20], industrial process control [21,22], exoplanet detection [23–25] as well as early-stage medical diagnosis [26–29].
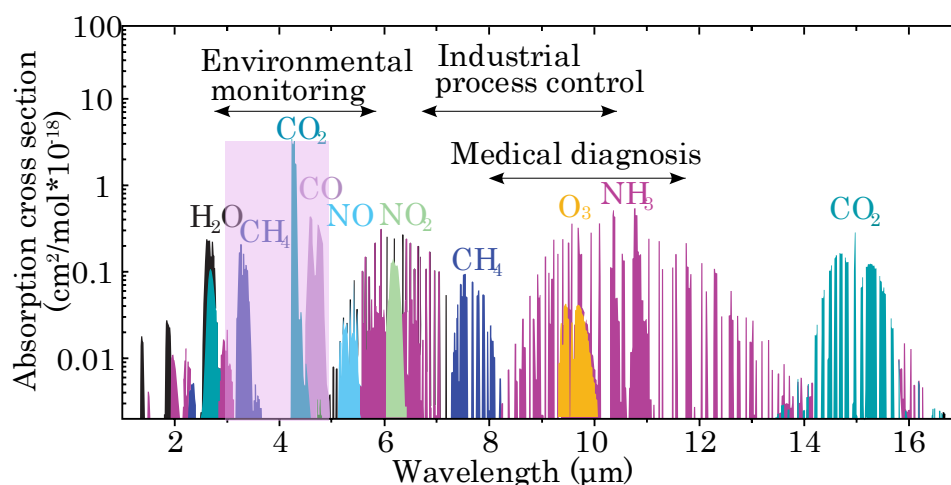
Figure 1.1 Mid-IR molecular fingerprints of selected molecules. The individual line intensities are extracted based on HITRAN 2016 database. The atmospheric window between 3 - 5 µm is highlighted for clarity. Reproduced from [4].

The mid-IR spectral region also has several windows of transparency in Earth's atmosphere. Particularly, the second mid-IR atmospheric window between 3 – 5 µm (2000 – 3300 cm^{-1}), also known as the functional group window, is of high interest.

It contains the molecular fingerprint of many hydrocarbons (CH bonds), molecules with oxygen (OH) or nitrogen (NH) stretching vibration, as well as molecular specimens detectable in breath analysis [30].

An essential component for gas detection and spectroscopy is a light source suited for the spectral range of interest. Laser-based spectroscopy has been a well-established and powerful technique for resolving molecular linewidths since the early 1980s [31]. Particularly mid-IR molecular spectroscopy has progressed significantly during the last two decades, owing to the invention and development of a novel and unique photonic tool, the optical frequency comb (OFC) [32–36]. Although lasers have existed since the 1960s, OFCs were introduced after 2000 by John L. Hall and Theodor W. Hänsch. Thanks to their discovery, they were awarded with a 2/3 part of the Nobel Prize in Physics in 2005 [37]. Optical frequency combs are broadband sources that present sharp and discrete evenly spaced spectral lines. Fig. 1.2 shows the time and frequency domain respectively a frequency comb [32]. In the time domain, a train of ultrashort equally spaced pulses with a repetition rate f_{rep} and a period of the pulse envelope $1/f_{rep}$ is produced. This corresponds to a spectrum of many narrow lines in the frequency domain, the so-called "teeth" of the comb, separated by the pulse repetition rate f_{rep} [32]. The carrier-envelope offset frequency f_0 (or f_{CEO}) determines the nth comb line's frequency, f_n, to be a harmonic of the pulse repetition frequency $f_n = nf_{rep} + f_0$.
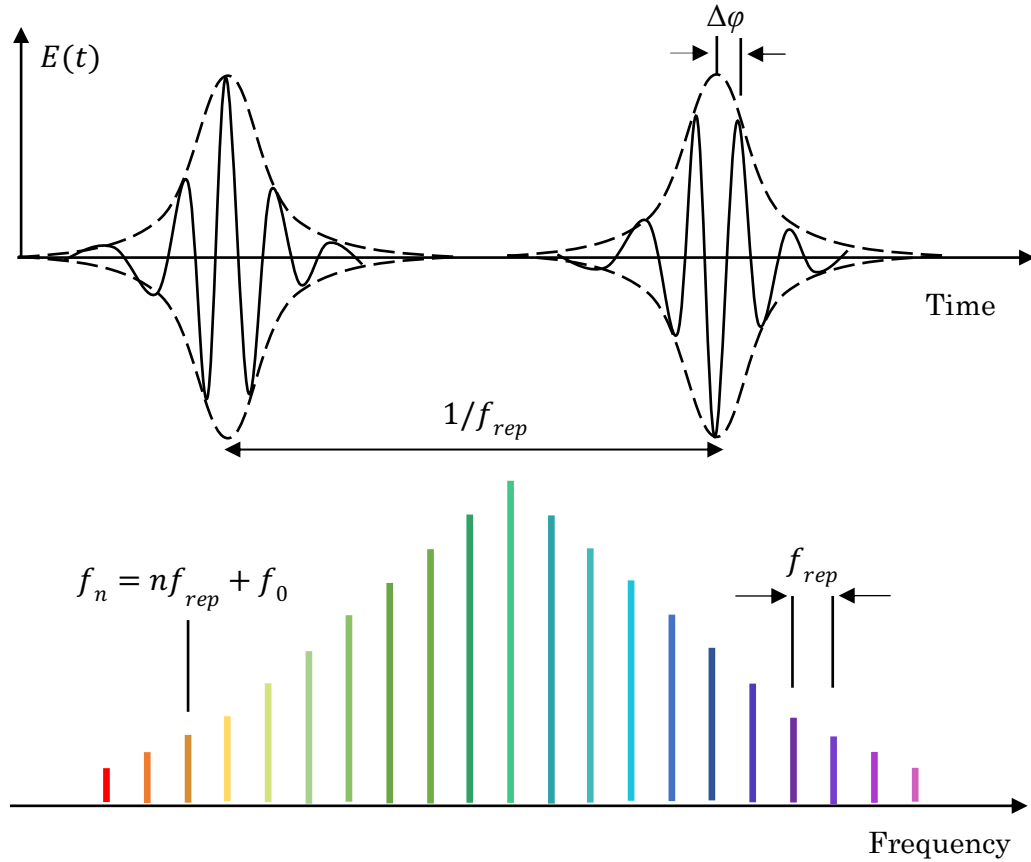
Figure 1.2 Optical frequency comb representation in time and frequency domain. A train of ultrashort pulses of period $1/f_{rep}$ (top) and the equivalent spectrum of narrow lines (bottom), the "teeth," of a frequency comb. Adapted from [32].

The observed pulse-to-pulse constant phase slippage $\Delta\varphi$ between the underlying carrier wave and the envelope of the pulse's electric field is an outcome of the different group and phase velocity and can be controlled utilizing different carrier-envelope phase (CEP) stabilization techniques, such as self-referencing method [38]. The CEP stabilization enables maximum stability of the frequency comb. Therefore, it is paramount to use a mode-locked laser (MLL) - which also generates a repetitive train of ultrashort pulses that must be stabilized to be transformed to an OFC - with the highest performance and reduced noise levels [38–40].
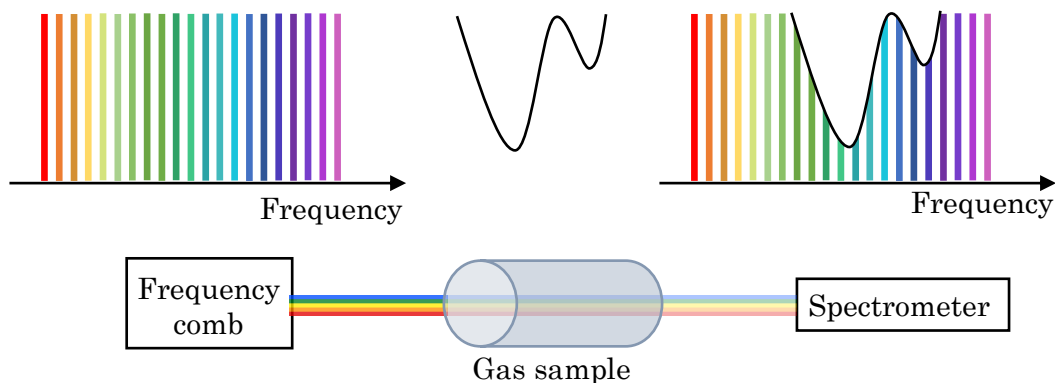
Figure 1.3 Absorption spectroscopy using frequency combs in its most straightforward approach. The broadband source interrogates the sample, and the transmission spectra are recorded with a spectrometer. Adapted from [32].

Since their inception, frequency combs have mainly been used for frequency metrology, leveraging the direct and precise link between microwave and optical frequencies and for molecular spectroscopy [35]. Due to their narrow teeth linewidths and precise frequency spacing, OFCs can probe narrow molecular transitions offering a substantial advantage over conventional spectroscopy techniques. In the simplest configuration, like in Fig. 1.3, a frequency comb directly interrogates the sample, and the spectral response of this molecular excitation is recorded using a spectrometer. Linear absorption is the simplest yet efficient type of molecular spectroscopy using frequency combs [32].

A variety of methods have been proposed for frequency comb generation, such as MLLs [41–45], electro-optic modulators [46–48], nonlinear frequency conversion [49–54], and micro-resonator-based frequency comb generation [55–59], with the latter one playing a pivotal role in comb synthesis owing to their miniaturized nature, low power consumption and stability [60].

For mid-IR spectroscopy, detecting molecular signatures in the mid-IR requires a significant field intensity achieved through numerous advanced techniques. OFCs constitute a powerful mid-IR spectroscopy tool, with dual-comb spectroscopy gaining continuous interest within the scientific community by offering rapid, accurate, ultra-high resolution and broad bandwidth detection [61]. While in the last five years dual-comb spectroscopy has been established as the workhorse in the field of mid-IR spectroscopy [62–65], this scheme requires two comb laser systems having slightly different repetition rates. Moreover, temporal synchronization between the two combs with interferometric precision is necessary for their high-performance operation. Thus, the dual-comb

configuration makes the system bulky and challenging to synchronize - the only weakness into its incomparable superiority.

Apart from OFCs, different approaches for reaching the mid-IR spectral range are the direct mid-IR generation with quantum cascade lasers (QCLs) [66,67] as well as with interband cascade lasers (ICLs) [68,69]. An efficient alternative to these tools, which can provide extra tunability, is mid-IR light generation through nonlinear frequency conversion. Mid-IR radiation used for spectroscopic applications can be generated through nonlinear conversion techniques, with the most essential being optical parametric oscillation (OPO) [70–72] and difference frequency generation (DFG) [73,74], which offer unprecedented tunability but tend to be bulky.

Accessing the mid-IR spectral range can also be effectively achieved by supercontinuum generation (SCG) in optical fibers [75–79] or photonic integrated waveguide platforms [80–84]. SCG represents a well-established and powerful technique to produce ultra-broadband light based on extreme nonlinear interactions when a pulsed pump laser propagates inside a nonlinear medium [85]. Since the discovery of SCG in 1970 in bulk media such as BK-7 glass [86], optical fibers, and especially photonic crystal fibers (PCFs) have had a leading role in the SCG research playground, benefiting from enhanced modal confinement and considerable flexibility on the dispersion engineering [87]. Moreover, on-chip nanophotonic waveguides have the strong advantage of precise lithographic control of the dispersion, which is very sensitive to the waveguide cross-section and enhanced nonlinearity in shorter interaction lengths due to their micrometric or sub-micrometric scale effective mode area. As a consequence, exploiting new platforms such as integrated waveguides for generating SC sources is nowadays an active area of research that tends to take over the field of PCFs. Integrated solutions also offer a path towards fully integrated photonic devices that merge multiple functionalities in single chip-based platforms that can be utilized in sensing and spectroscopy [88].

Several materials have been recognized as ideal platforms for broadband mid-IR light generation in optical fibers. Chalcogenide (AsSe, AsS, GeAsSe) [89,90], telluride (GeTe, Ge-As-Se-Te) [91,92], and fluoride (ZBLAN - ZrF_4-BaF_2-LaF_3-AlF_3-NaF) [93] glasses are the main hosting materials for mid-IR SC in optical fibers, with powers reaching tens of watts in the output [94].

Table 1.1 summarizes all recently published results on mid-IR SC generated in different optical fiber platforms. A comparison of the SC bandwidth, the pump wavelength, and the dispersion regime at the pumping wavelength are presented for each hosting material. The required pump powers for driving the SC are also reported in Table 1.1 for a detailed comparison.

Supercontinuum in optical fiber platforms

Material	SCG bandwidth (µm)	Pump wavelength (µm)	Pump GVD regime	Power (P_{in}/P_{out}) or pulse energy (E_p) [1]	Ref.
As_2S_3	1 – 3.7	2.04	anomalous	450 mW/15 mW	[75]
As_2Se_3	1.8 – 9.5	2.9	normal	4.2 kW/30 mW	[90]
$AsSe_2$	1.6 – 3.7	2.6	normal	10.12 kW/NA	[79]
$As_{40}Se_{60}$	1.4 – 13.3	6.3	anomalous	760 mW / 150 µW	[89]
	1.5 – 11.7	4.5	normal	350 mW	
InF_3	2.4 – 5.4	2.75	anomalous	978 mW/16.3 mW	[76]
InF_3	1.9 – 4.9	2.2	anomalous	17.5 W/11.7 W	[78]
Ge-As-Se-Te	1.5 – 11.6	4.65	normal	36 mW/6.5 mW	[77]
TeO_2-ZnO-Na_2O	0.75 – 2.8	1.75	anomalous	112 mW/10 mW	[91]
TeO_2-BaF_2-Y_2O_3	0.95 – 3.93	1.98	anomalous	15.9 W/10.4 W	[94]
Ge-Te-AgI	2 – 16	7	normal	11.5 mW/16 µW	[92]
ZBLAN	0.38 – 4	2	anomalous	0.5 µJ	[93]

Table 1.1 Literature experimental data of mid-IR SC sources developed on fiber-based platforms. The table contains the material, the total SC bandwidth, the pump wavelength and dispersion regime at this wavelength, as well as input (P_{in}) and output (P_{out}) power parameters.

Focusing on integrated platforms, aluminum nitride (AlN) [95,96], lithium niobate (LiNbO$_3$) [97], silicon-on-insulator (SOI) [98], silicon [99,100], silicon-rich nitride (SRN) [101], and silicon-germanium (SiGe) [102–104] are systematically investigated and have shown great potential for octave-spanning SCG extended to the mid-IR. Even though silicon nitride (Si$_3$N$_4$) supports multi-octave SCG [105–109], the mid-IR extension is not extensively explored in this material. All the aforementioned integrated platforms are compact, and they can benefit from large-scale manufacturing. Among the common characteristic of these various platforms, materials compatible with silicon photonics hold the promise of co-integration with electronics while preserving a low cost.

A summary of the available SC sources developed in integrated platforms is presented in Table 1.2, following the same model of Table 1.1. Experimental results on SCG in Si$_3$N$_4$ waveguides presented in previous studies are compared with the results obtained in this thesis. The power comparison should be treated carefully since it can be reported using either injected or coupled pump powers.

---

[1]Power comparison is not straightforward, since the reported values may differ in terms of the given power. For example, some works report the peak pump power P_{in} (usually in kW) injected into the material, or the coupled pump powers - either in kW (for peak powers) or in mW (for average powers). Moreover, some works express the requirements for driving SC using the energy of the pulse (E_p) in J. Reported average output powers P_{out} are usually measured in the output of the fiber considering the entire SC spectrum. In some cases, total output powers are not reported at all, and the acronym "NA" stands for not available data.

Supercontinuum in integrated platforms

Material	SCG bandwidth (µm)	Pump wavelength (µm)	Pump GVD regime	Power (P_{in}/P_{out}) or pulse energy (E_p)[2]	Ref.
SOS	1.9 – 6	3.7	anomalous	2.5 kW/NA	[80]
Si	1.1 – 2.76	2.2	anomalous	70 mW/NA	[82]
AlGaAsOI	1.3 – 1.8	1.56	anomalous	3.1 pJ	[83]
Ta_2O_5	0.75 – 2.4	1.56	anomalous	90 mW/NA	[84]
AlN	0.75 – 3.75	1.56	anomalous	140 mW/NA	[96]
LiNb	0.35 – 4.1	1.55	anomalous	240 pJ/NA	[97]
SOI	1.2 – 4	2.10	anomalous	200 W/NA	[98]
	1.3 – 3	2.10	normal		
SOI	1.5 – 3.6	2.5	anomalous	125 W/NA	[99]
SOI	2 – 5	4	anomalous	28.8 mW/NA	[100]
SRN	0.82 – 2.25	1.55	anomalous	105 pJ/NA	[101]
SiGe	3 – 8.3	4	anomalous	25 mW/12.5 mW	[102]
	2.6 – 6.2	4	anomalous	16 mW/7.25 mW	
SiGe	3 – 13	8.5	anomalous	8 mW/	[103]
SiGe	3.19 – 5.65	4.6	anomalous	23 mW/2.2 mW	[104]
	3.39 – 6.02	4.6	normal	23 mW/4.4 mW	
Si_xN_y	0.75 – 2.4	1.56	anomalous	20 kW/0.5 µW	[81]
SiN	0.66 – 2.02	1.3	anomalous	160 pJ/NA	[105]
Si_3N_4	0.67 – 1.75	1.05	anomalous	36 pJ/NA	[106]
Si_3N_4	0.52 – 2.6	1.56	anomalous	1.4 nJ/NA	[107]
Si_3N_4	0.48 – 0.98	0.795	anomalous	874 W /NA	[108]
Si_3N_4	0.47 – 2.13	1.064	anomalous	590 pJ/NA	[109]
Si_3N_4	0.5 – 4	1.55	anomalous	1 nJ/100 µW	[110]
Si_3N_4	**0.5 – 4**	**2.10**	**anomalous**	**25 mW/8.4mW**	**[thesis]**
Si_3N_4	**0.5 – 2.9**	**2.10**	**anomalous**	**24 mW/7.5 mW**	**[thesis]**
	1.6 - 2.3	**2.10**	**normal**	**15 mW/9 mW**	

Table 1.2 Comparison of recently developed SC sources based on various integrated platforms. The table contains the hosting material, the total bandwidth of generated SC, the pumping wavelength, and the dispersion regime at that wavelength. Input and output power parameters are also presented.

---

[2]Power comparison is difficult, considering the different ways it can be expressed. The majority of studies report the injected pump powers (or pulse energies) without considering the in-coupling losses, while others report the power (or pulse energy) coupled into the waveguide. In most of cases, output power values are not reported. However, when output powers are measured, the on-chip powers are usually reported, considering the out-coupling losses. The reported thesis powers are the maximum estimated average coupled powers and the maximum achieved on-chip powers. However, it must be noted that the on-chip measured power corresponds only to the mid-IR part, and not the entire SC source.

Moreover, a comparison between the most common materials widely used in silicon photonic integrated device compatible with complementary-metal-oxide-semiconductor (CMOS) fabrication processes is presented in Table 1.3. Silicon, silicon nitride, and silicon-germanium are used as waveguide core materials, while silicon and silicon dioxide are typically the waveguide substrate materials. Even though silicon constitutes an ideal platform for broad on-chip SCG, it is affected by strong two-photon absorption (TPA) and free-carrier absorption (FCA) at the telecommunication wavelengths (near-IR region) and up to 2 µm area [111]. This fact limits its performance by increasing the nonlinear losses at these particular wavelengths. On the other hand, silicon germanium has a huge transparency window extended to far mid-IR. However, this material is not transparent in the visible and telecom/near-IR portion of the spectrum. As a result, it cannot be pumped with commercially available femtosecond laser sources [112].

Unlike other CMOS-compatible materials, silicon nitride in its stoichiometric composition (Si_3N_4) has a large energy bandgap (E_g) of 5 eV [113,114], thereby does not suffer from the undesirable nonlinear losses caused by TPA at telecom and from multi-photon absorption at short-wave-IR (SWIR) wavelengths which usually serve as pumping sources for SCG. As a result, silicon nitride has recently appeared as a promising alternative material for nonlinear optics, complemented by its wide transparency window from visible to the mid-IR (0.4 – 7 µm), ten times higher nonlinearity than SiO_2, CMOS compatibility, and excellent linear optical properties. [115]. The high refractive index contrast between the Si_3N_4 core and the SiO_2 lower-index substrate leads to strong mode confinement.

Silicon photonics materials	Refractive index (at 2 µm)	Bandgap E_g (eV)	Transparency window (µm)	n_2 (at 2 µm) [m²/W]
$Si_{1-x} Ge_x$	4	0.68 – 2.25	2 – 14	0.1 – 0.2 x 10 $^{-18}$
Si	3.45	1.15	1 – 8.5	3 x 10 $^{-18}$
Si_3N_4	2	5	0.4 – 7	0.24 x 10 $^{-18}$
SiO_2	1.45	8.9	0.3 – 3.5	0.025 x 10 $^{-18}$

Table 1.3 Comparison between some widely used CMOS compatible materials in terms of refractive index, energy bandgap, transparency window, and nonlinear refractive index n_2. The values of this table are extracted by a literature review [112–115].

Relying on its excellent optical properties, Si_3N_4 constitutes a superior candidate for demonstrating broadband on-chip SCG. Waveguide dispersion engineering is also possible by flexibly tailoring the waveguide geometry. However, Si_3N_4 thin films are prone to cracking when depositing a layer of thickness above ~ 1 µm. This limits the operational wavelength on such waveguides, particularly in the mid-IR, where a large-size waveguide is usually required for providing mode confinement while preserving the required dispersion engineering. Fortunately, this hurdle has now been overcome by outstanding progress in Si_3N_4 waveguide fabrication techniques such as the photonic Damascene process [116] that operates beyond cracking limitations and achieves large cross-section waveguides, as we will see in the last section of the chapter.

In SCG based on nanophotonic waveguides, the hosting material and the waveguide's dispersion engineering plus the underlying SC dynamics play a significant role in the extension into the mid-IR. Specifically, beyond the self-phase modulation (SPM) induced broadening, soliton fission-driven dispersive wave (DW) generation is the phenomenon that enables coherent and efficient light transfer from the pump to the well-located DWs [117]. This mechanism, the result of the higher-order dispersion-induced Cherenkov radiation [118] –commonly known as DW–, can extend the injected pump source's bandwidth and accomplish octave-spanning SCG by proper dispersion engineering of the waveguide.

1.2 Overview of Broadband Sources used in Spectroscopy

As discussed in the previous section of the introduction, spectroscopy based on broadband sources constitutes a valuable tool for detecting molecular species. Specifically, a source with a larger spectral bandwidth capable of identifying and quantifying multiple gas species simultaneously is required for environmental trace-gas detection. On the other hand, if we target enhanced sensitivity for spectroscopy, a higher brightness source is needed. An overview of the EM spectrum regions from ultra-violet (UV) up to THz frequencies with spectroscopic interest and the different types of available light sources are presented in Fig. 1.4 [119]. On the top part of the graph, molecular cross-sections are shown, while in the bottom part, the available broadband source corresponds to each wavelength region. As we can observe, the absorption lines are much stronger and richer in the mid-IR, far-IR, and THz areas. However, there is a lack of sources covering these parts.

On the other hand, in the visible and near-IR, we observe that sources are well developed, but there are not such strong absorption signals. Apart from their spectral coverage, broadband sources have many differences between each other, such that a fair direct comparison is complicated. Generally, they can be categorized into three main categories: incoherent broadband sources, supercontinuum sources, and optical frequency combs. The latter two groups have already been introduced in 1.1. Spatially incoherent light sources such as gas discharge lamps (xenium arc (Xe-arc), deuterium arc (D-arc)), Globar, and light-emitting diodes (LED) prevail in terms of spectral coverage and simplicity. On the other hand, their limited power per spatial mode leads to divergence and efficiency deprivation [119]. Frequency combs are an imperative tool in the broadband source foreground. However, they appear bulkier in the mid-IR – OPOs and DFG schemes – and have limited portability.

Finally, broadband SC sources generated either in optical fibers or waveguides via nonlinear interactions are desirable platforms from an application point of view due to their small footprint and versatility. There are, of course, weak points in the SC source we must consider, such as the noise amplification. However, there are many trade-offs that can be made by a balanced selection between the input pulse parameters and the nonlinear medium characteristics. Another trade-off, and potential weak point, of

broadband sources' performance, also depicted in Fig. 1.4, is between the spectral coverage and the spectral intensity.

Considering the advantages of SCG, we focus only on the development of broadband SC sources and their utilization in mid-IR spectroscopy. Therefore, the work presented in this thesis focuses on a relatively small yet significant part of the EM spectrum between 2 – 4 µm, as seen from the highlighted part of Fig. 1.4. As we notice, this region has been reached using incoherent lamps, SC and OPOs until now, leaving significant space for the development of new mid-IR sources.
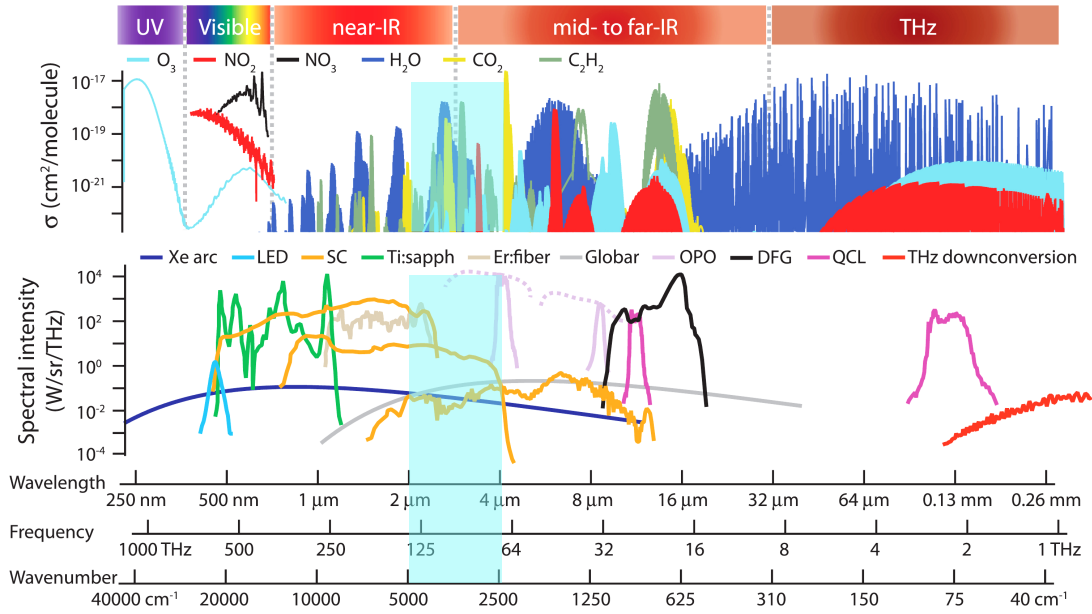
Figure 1.4 Overview of broadband sources used in gas-phase spectroscopy from UV to THz. The mid-IR spectral region covered in the thesis is shaded for clarity. Adapted from [119].

1.3 Towards the mid-IR – Thesis Goal

On-chip platforms offer the advantage of a miniaturized SC source which opens the path towards the development of compact, robust, low cost and mass-producible integrated devices. The generation of light inside a chip promises as well lower power consumption and energy-saving devices. Among all of the approaches presented in the first part of the chapter, SCG is undoubtedly one of the most versatile methods to generate mid-IR light that can be easily tuned by leveraging the dispersion properties of the pumped waveguides. Although many on-chip SC sources have already been demonstrated, the majority of them operate in the near-infrared (near-IR) spectral range. At the same time, the extension into the mid-IR remains relatively unexplored and still technically challenging. Very few platforms managed to achieve tight light confinement at long wavelengths and, at the same time, low losses. These few demonstrations rely mostly on pumping the waveguide already with a mid-IR source, such as an OPO. Nowadays, dispersion engineered Si_3N_4 waveguides have shown great potential for on-chip multi-octave spanning SCG in the near-IR part of the spectrum. There is an impressive number

of studies reporting SC in Si_3N_4 platforms [105-110]. However, light generation within the mid-IR range (2.5 – 4.0 μm) has never been successfully achieved in Si_3N_4, and the longest part of radiation could not exceed 2.5 μm. The main limitation is linked to the low mode confinement of the mid-IR part.

Recently, an important first step towards the coveted mid-IR generation in Si_3N_4 waveguides was established by pumping large cross-section Si_3N_4 waveguides with a telecom-band (1.55 μm) erbium (Er)-doped fiber femtosecond laser [110]. Si_3N_4 waveguides fabricated with the photonic Damascene process have strong mode confinement at mid-IR. At the same time, the increased geometric space allows for suitable dispersion engineering to support soliton fission-driven SCG. The tunability of the generated mid-IR radiation in the forms of DWs can be precisely adjusted by lithography. The wavelengths at which the GVD crosses zero can be set by varying the waveguide cross-section dimensions (width x height). Therefore, dispersion control is crucial for the location of the converted radiation, and the locations of generated DWs are determined by dispersion and phase-matching parameters. Indeed, with the large cross-section Si_3N_4 waveguides, the functional group region between 2.5 – 4.0 μm has been covered [110].

Moreover, a high level of phase coherence is transferred from the seed laser to the generated mid-IR radiation. A remaining obstacle that limits the performance of these telecom-pumped waveguides is the mid-IR efficiency. The generated mid-IR DW has very low power. Thus, it cannot be used as a molecular spectroscopy source. Another interesting observation is that the nonlinear phenomena in the SCG process convert part of the pump energy over unwanted spectral bands, further decreasing the conversion efficiency (CE) in the spectral region of interest.

This discussion's outcome is that reaching efficient wavelength conversion beyond 3 μm is still tricky when fiber pump lasers are utilized, so there is a demanding need to push the limits in terms of both reach and efficiency of the chip-based light sources into the mid-IR.

The dissertation's primary goal is to design and develop small footprint chip-based devices based on the SCG process inside dispersion engineered Si_3N_4 waveguides, which can be utilized in actual spectroscopy measurements. The advantage of an SCG approach lies in the comfort of operation and the simplicity. In fact, it is a single-pass configuration that does not require any additional seed laser or temporal synchronization. For that purpose, two different types of waveguides are investigated for SCG as we will see in the following chapters: cladded Si_3N_4 waveguides (where the Si_3N_4 core is buried into SiO_2) and fully un-cladded where the air-cladding design further offers the possibility to deposit a substance directly on-chip for sensing applications.

In the thesis, the hurdles of spectral coverage and efficiency mentioned above are tackled by shifting the pump wavelength at 2 μm and using dispersion engineered large cross-section Si_3N_4 waveguides. Pumping with SWIR femtosecond laser pulses, *efficient* and *tunable* mid-IR radiation is generated. A breakthrough conversion efficiency of up to 35 % is reported for energy transferred from 2 μm to the entire 3 - 4 μm spectral range. Starting from a proof-of-concept spectroscopy experiment, this tunable 3 – 4 μm source

is used for simultaneous detection of multiple gas species such as acetylene (C_2H_2), methane (CH_4), and ethane (C_2H_6). This is the first time that light generated inside a single Si_3N_4 waveguide can detect and quantify multiple gas-phase species. The thesis presents a detailed experimental and numerically simulated study on DWG and CE and SCG dynamics in Si_3N_4 waveguides.

In the effort to reach the mid-IR and develop versatile SC sources for molecular sensing, extreme polarization-sensitive SC in an uncladded Si_3N_4 waveguide design is also studied. Leveraging the different dispersion regimes, anomalous and normal, while pumping in the transverse electric (TE) or in transverse magnetic (TM) mode, soliton-fission driven and all-normal dispersion (ANDi) SC is generated respectively, reaching wavelengths up to 3 µm.

Overall, this thesis has accomplished the following objectives:

i. The development of a new type of compact and tunable mid-IR SC source that consists of a standard SWIR fiber MLL and a 5 mm long chip with different cross-sectional geometries of Si_3N_4 waveguides. Lithographic control of the waveguide dispersion by varying the waveguide's dimensions enables tailored infrared dispersive wave generation across the entire bandwidth between 3 – 4 µm.

ii. Improvement of the CE in the mid-IR while significantly suppressing unwanted parts of the spectrum such as the visible part. The device sets a new benchmark for mid-IR efficiency with up to 35% power conversion and achieved milliwatt-level output powers. This is the highest reported mid-IR CE in Si_3N_4 platform generated by merging mature chip fabrication technology and compact turn-key 2 µm laser source.

iii. Application of the on-chip generated mid-IR source in a proof-of-principle direct absorption spectroscopy experiment. Successful detection of gas acetylene (C_2H_2) presence and concentration with an 11 parts-per-million (ppm) detection limit in a 1 m long gas cell has also been achieved.

iv. Extend the toolkit for mid-IR spectroscopy by detecting and quantifying multiple gas-phase species using a single Si_3N_4 waveguide and a single fiber pump. For the first time, a mid-IR DW generated in a single dispersion tailored Si_3N_4 nanophotonic waveguide provides such a broad spectral coverage (up to 1000nm) that can demonstrate successfully simultaneous detection of multiple gas-phase species within the spectral region from 2.95 to 3.4 µm, an essential window for mid-IR greenhouse gas spectroscopy, however, not easily accessible with other table-top laser sources. The on-chip device is capable of achieving simultaneous detection of acetylene (C_2H_2), methane (CH_4), and ethane (C_2H_6) with several hundreds of parts-per-million (ppm) detection limit, using direct absorption spectroscopy with only a 5 cm long gas cell.

v. Experimental demonstration of extreme polarization-sensitive SWIR SC in uncladded Si_3N_4 waveguides extended up to 2.9 µm. The specific air-cladded design is dispersion engineered to provide ANDi SCG at near-IR for TM polarization mode. In contrast, the dispersion falls into the anomalous regime for TE mode excitation. Leveraging the different dispersion profiles, we switch from an octave-spanning

soliton fission-driven SC to a flat and smooth SPM-dominated ANDi SC by simply adjusting the input polarization state.

Apart from the detailed experimental results presented in this thesis, numerical simulations support and validate the dissertation's importance and give insights into the physical mechanisms of the SCG in different Si_3N_4 waveguide designs.

1.4 Structure of the Thesis

The remainder of the thesis is organized based on the following chapters:

Chapter 2: The dissertation's theoretical background is presented in the second chapter, divided into three main sections. Starting from the basic formulas for optical waveguide modes inside silicon nitride, emphasis is given to the group velocity dispersion (GVD), a driving parameter of the SC process. Subsequently, we introduce the mathematical model used for numerical simulations of Chapter 3 and Chapter 5, based on the well-known Nonlinear Schrödinger equation (NLSE), which describes the nonlinear pulse propagation inside the Si_3N_4 waveguides. Unraveling the different phenomena that take part in the complicated SCG - such as self-phase modulation (SPM) and soliton-fission that results in the emission of DWs - we get better insights into the femtosecond pulse propagation inside different waveguide geometries. The last section of the chapter is devoted to linear absorption spectroscopy and some theory behind molecular absorption line analysis presented in Chapter 4.

Chapter 3: This chapter presents the inception and development of an efficient and tunable mid-IR source generated through the SC process in stoichiometric large cross-section Si_3N_4 waveguides. The chapter contains the design of such a mid-IR source and experimental results and a numerically simulated study of the dynamics. The richness of soliton dynamics such as soliton fission and dispersive wave generation (DWG) and their underlying role in the SCG process are investigated. Trade-offs between spectral coverage and conversion efficiency into the mid-IR are also discussed. The whole energy transfer process is based on DWG, which guarantees coherence transfer from the pump wavelength to the generated waves.

Chapter 4: The fourth chapter focuses on the application part, the mid-IR direct absorption spectroscopy. Using the generated tunable mid-IR radiation in the form of DWs between 3 – 4 µm, a proof-of-principle detection of acetylene (C_2H_2) was initially achieved. The system was further engineered to perform parallel gas-phase species spectroscopy using a single dispersive wave and a single laser pump, achieving simultaneous detection of acetylene (C_2H_2), methane (CH_4), and ethane (C_2H_6). Trade-offs between the SNR and the power of the generated DW are also being discussed. The device's reliability is established by an excellent agreement between measured absorption lines and the HITRAN database.

<u>Chapter 5</u>: Another type of Si_3N_4 waveguides is studied in this chapter, fully air-cladded waveguides which exhibit extreme polarization sensitivity while pumped at 2.1 μm. Leveraging TM/TE dispersion engineering, we can switch between a flat SPM-dominated ANDi SCG and an octave-spanning soliton-fission driven SC that extends to almost 3 μm. This uncladded design, which sustains long propagation, can further offer direct interactions with substances on-chip, making it a promising approach for sensing applications.

<u>Chapter 6</u>: The last chapter summarizes the results obtained in this thesis and suggests possibilities for future improvements of the investigated devices.

Chapter 2

Theoretical background

Theoretical background

In this chapter, basic principles and theory involved in the experimental part of the thesis are introduced. Starting from the theory of optical modes in the waveguides and the group velocity dispersion (GVD), we go through the most critical nonlinear phenomena behind supercontinuum generation (SCG) in Si_3N_4 waveguides under femtosecond pulse duration pumping: self-phase modulation (SPM), optical wave breaking (OWB) and soliton fission. Dispersive wave generation (DWG), the principal wavelength conversion mechanism in this dissertation, is also discussed. Conventionally, ultrafast pulse propagation within a nonlinear medium is simulated using the Generalized Nonlinear Schrödinger Equation (GNLSE). The numerical simulations presented in Chapter 3 and Chapter 5 are based on the GNLSE numerical model. The last part of the chapter is devoted to linear absorption spectroscopy basics and gives a better understanding of different broadening types of molecular lines.

2.1 Basic Principles of Optical Waveguides

2.1.1 Optical modes in Si_3N_4 waveguides

The building block of a device designed for on-chip supercontinuum generation (SCG) is the optical waveguide that can guide the coupled light and convert it through nonlinear processes to different wavelengths. In the most common form, an optical waveguide consists of two dielectric materials with different refractive indices. The core material of the waveguides studied in the presented dissertation is stoichiometric silicon-nitride (Si_3N_4) and is surrounded by a lower refractive index material, the cladding or substrate, which is silicon dioxide (SiO_2). There are also air-cladded designs where the core is simply not covered by SiO_2. Light is confined in the Si_3N_4 core and is guided by total internal reflection at the core-cladding interface. The waveguide geometry implies a preferential propagation direction. We will consider pulse propagation in the *z*-axis and *x* and *y*, the two primary waveguide's axes [120,121].

At a given frequency ω, the optical waveguides can support a finite number of guided modes in the core, the eigenmodes, whose spatial distribution is a solution of the wave equation (2.1) and satisfies the appropriate boundary conditions. Starting from the well-known Maxwell's equations that govern all electromagnetic phenomena, a general inhomogeneous wave equation is derived, having the form of the Helmholtz equation [117,122]:

$$\nabla^2 \tilde{E} + n^2(\omega) \frac{\omega^2}{c^2} \tilde{E} = 0 \qquad (2.1)$$

where $\tilde{E}$ is the Fourier transform of the electric field, $n(\omega)$ the frequency-dependent refractive index and c is the speed of light in the vacuum. Although there is an analogous equation (2.1) for the magnetic field, we typically solve the wave equation using the

electric field version. Both fields are correlated to each other through Maxwell's equations.

One step further, we assume that the dielectric materials (Si_3N_4 and SiO_2) have a lack of free charges and current as well as a translation-invariant amplitude in the z-direction of the electric field. Using these simplifications, we end up in the following form of the initial wave equation: the modal vector wave equation [122]:

$$(\nabla_{x,y}^2 + k^2 n_{x,y}^2 - \beta^2)E_{x,y} = -(\nabla_{x,y} + i\beta\hat{z})(E_{x,y}\nabla_{x,y} \, ln \, n^2) \qquad (2.2)$$

where $k = 2\pi/\lambda$ is the wavenumber of the electric field, $n(x,y)$ the transverse distribution of the refractive index for the waveguide, β the propagation constant of the mode, $\hat{z}$ the unit vector in the direction of propagation axis, $E_{x,y}$ the electric field distribution, and $\nabla_{x,y}^2$ is the transverse vector Laplacian operator [122].

The optical modes of the waveguide are eigen-solutions of the eigenvalue equation (2.2) expressed through the spatial distributions of the mode field, $E(x,y)$. As a result, by solving this equation, the propagation constant β of the individual optical modes can be calculated for a specific wavelength λ and a refractive index distribution $n(x,y)$.

The effective refractive index n_{eff} of each optical waveguide mode is related to β and is calculated by the equation:

$$n_{eff} = \frac{\beta}{k} = \frac{\beta\lambda}{2\pi} \qquad (2.3)$$

while the equation (2.4) calculates the effective mode area of a given mode:

$$A_{eff} = \frac{(\iint_{-\infty}^{+\infty}|E(x,y)|^2 dx \, dy)^2}{\iint_{-\infty}^{+\infty}|E(x,y)|^4 dx \, dy} \qquad (2.4)$$

Both n_{eff} and A_{eff} are essential for the pulse propagation inside the waveguide that is discussed later in this chapter.

For the simulation of the optical modes in the Si_3N_4 waveguides and the calculation of n_{eff} and A_{eff}, we use the finite-element method (FEM) software COMSOL Multiphysics to solve the governing Maxwell's equations. Using a two-dimensional (2D) schematic of our waveguide cross-section, equation (2.2) is solved by applying specific boundary and continuity conditions at each material's interfaces while considering core and cladding as a set of finite elements. The density of elements is defined by the mesh in COMSOL and determines the calculation accuracy. The fundamental transverse magnetic (TM_{00}) and the fundamental transverse electric (TE_{00}) modes are considered for numerical simulations in this study while coupling to higher-order modes during propagation inside the waveguide is neglected. TM and TE modes' properties depend on the symmetry and the geometry of the waveguides [122]. To distinguish between the TM and the TE waveguide modes in the model, we clarify that TM modes are polarized in the y-direction while the TE modes are polarized in the x-direction.

The integrated optical waveguides used in the dissertation are presented in Fig. 2.1. They can be divided into two main categories based on their design and fabrication: the first

one is Si_3N_4 waveguides completely buried in SiO_2, and the second category considers uncladded or air-cladded Si_3N_4 waveguides.
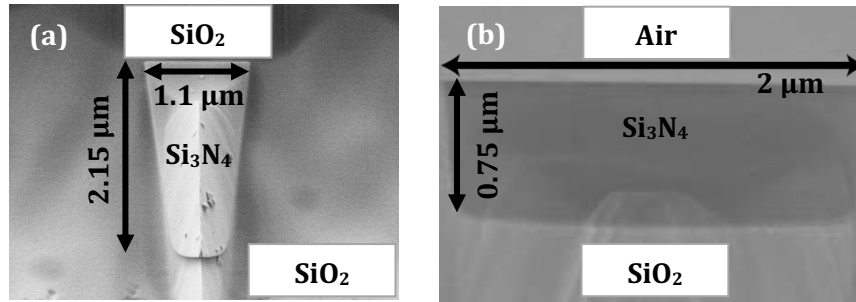
Figure 2.1 Scanning electron microscopy (SEM) images of (a) SiO_2-cladded waveguide with a cross section of 1.10 x 2.15 μm^2 (width x height) and (b) air-cladded Si_3N_4 waveguide with a 2.00 x 0.75 μm^2 geometry.

Figure 2.2 shows the simulated electric field profiles for the fundamental TM mode of the buried Si_3N_4 waveguide used in chapters 3 and 4 of the thesis having a core width of w = 1.10 μm and a height of h = 2.15 μm. The field profiles correspond to different wavelengths from 2 μm to 4.5 μm, showing excellent mode confinement to the Si_3N_4 core region up to 4 μm. High modal confinement in the waveguide's core guarantees strong nonlinear interaction in the waveguide as well as less propagation losses even at longer wavelengths. The already introduced effective mode area, A_{eff}, can express the degree of modal confinement. The lowest value of A_{eff} corresponds to maximum modal confinement at a particular wavelength.
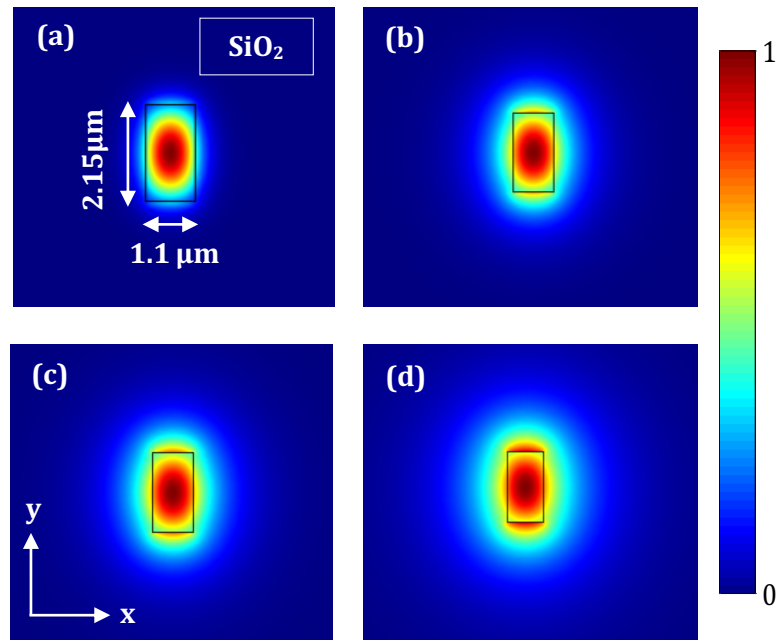
Figure 2.2 Simulated electric field distribution of optical modes for the fundamental TM_{00} propagation mode calculated with COMSOL in a Si_3N_4 waveguide with a width of 1.10 μm and a height of 2.15 μm for four different wavelengths, (a) 2 μm, (b) 3.5 μm, (c) 4 μm and (d) 4.5 μm. Mode is highly confined for wavelengths up to 4 μm.

Figure 2.3 shows the simulated electric field profiles of the fundamental TE mode ((a),(b),(c)) and the fundamental TM mode ((d),(e),(f)) of the uncladded Si_3N_4 waveguide design used in Chapter 5 of the thesis with a core width of w = 2.00 μm and a height of h = 0.75 μm. The field profiles correspond to three different wavelengths from 2 μm to 4.5 μm, showing excellent mode confinement to the Si_3N_4 core region up to 4 μm for the TE mode, while for the TM mode high degree of confinement can be preserved until 3 μm. Beyond this wavelength, TM mode is highly leaky in the SiO_2 cladding, while a tiny portion of the mode leaks in the air.
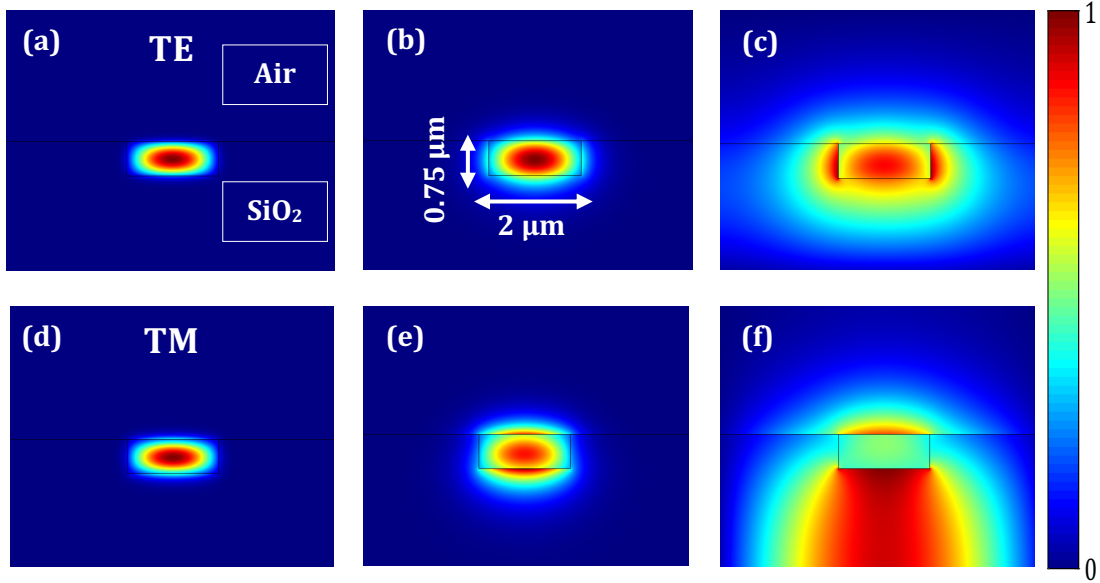
Figure 2.3 Simulated electric field distribution of optical modes for the fundamental TE_{00} mode calculated with COMSOL in a Si_3N_4 waveguide with a width of 2.00 μm and a height of 0.75 μm for three different wavelengths, (a) 2 μm, (b) 3 μm, and (c) 4.5 μm and for the TM_{00} mode (d), (e) and (f) for the same wavelengths, respectively.

Both cladded and uncladded waveguide geometries include short, tapered sections in the input and in the output. The inverse nanotapers ensure optimum coupling to the fundamental TE and TM polarization modes and as a result, we consider our waveguides as single mode. The waveguides can in theory support higher order modes, however their tapered sections ensure single mode operation.

2.1.2 Group Velocity Dispersion (GVD)

The response of a dielectric medium to an incident electromagnetic wave is expressed through the frequency dependence of the refractive index $n(\omega)$. This property is called material dispersion and leads to different refractive indices on each wavelength, which can be calculated using the Sellmeier equation [117]:

$$n^2(\omega) = 1 + \sum_{j=1}^{m} \frac{B_j \omega_j^2}{\omega_j^2 - \omega^2} \qquad (2.5)$$

where ω_j is the resonance frequency and B_j is the strength of jᵗʰ resonance. In the case of optical waveguides, these parameters can be experimentally measured and end up in a modified Sellmeier equation for a particular material.

Material dispersion is a crucial parameter in the propagation of ultrashort pulses since it results in frequency-dependent phase velocity inside a medium, given by: v_{phase}=c/$n(\omega)$.

Apart from the material dispersion, there is a frequency dependence on the mode propagation constant β in a waveguide structure, which can be expressed through the nonlinear refractive index n_{eff} presented in equation (2.3) as:

$$\beta = n_{eff}\frac{2\pi}{\lambda} \qquad (2.6)$$

The waveguide dispersion is thus strongly linked to the waveguide geometry, as it comes from the distribution of a waveguide mode at different wavelengths.

The chromatic dispersion, a combination of the material dispersion and the waveguide dispersion, can be explained through the dependence of the propagation constant β on the refractive index $n(\omega)$ and the angular frequency ω. It can be mathematically expressed as a Taylor series expansion of the frequency-dependent propagation constant of a waveguide mode $\beta(\omega)$ around a given central frequency ω_0:

$$\begin{aligned}
\beta(\omega) = n(\omega)\frac{\omega}{c} \\
= \beta_0 + \beta_1(\omega - \omega_0) + \frac{1}{2}\beta_2(\omega - \omega_0)^2 \\
+ \frac{1}{6}\beta_3(\omega - \omega_0)^3 + \ldots.\frac{1}{m!}\beta_m(\omega - \omega_0)^m \qquad (2.7)
\end{aligned}$$

where β_m is the mᵗʰ order of dispersion given by :

$$\beta_m = \left(\frac{d^m\beta}{d\omega^m}\right)$$

The individual terms of equation (2.7) play a significant role in the propagation of an optical pulse through the waveguide. Starting from β_0, which is the inverse of the phase velocity (v_{phase}), β_1 is the inverse of the group velocity of the pulse envelope (v_g=1/β_1). Group velocity is calculated by v_g= $d\omega/d\beta$ and is the velocity at which the carrier-envelope of an optical pulse is moving.

The β_2 term is the differential of group velocity v_g over frequency. This parameter is called group velocity dispersion (GVD) and represents the broadening of optical pulses while propagating in the waveguide.

The first two orders of dispersion in equation (2.7), the coefficients β_1 and β_2, are also linked to the frequency-dependent refractive index $n(\omega)$ through the equations [117]:

$$\beta_1 = \frac{1}{v_g} = \frac{n_g}{c} = \frac{1}{c}\left(n + \omega\frac{dn}{d\omega}\right) \qquad (2.8)$$

$$\beta_2 = \frac{1}{c}\left(2\frac{dn}{d\omega} + \omega\frac{d^2n}{d\omega^2}\right) \quad (2.9)$$

From the GVD, the dispersion parameter D can also be calculated:

$$D(\lambda) = \frac{d\beta_1}{d\lambda} = -\frac{2\pi c}{\lambda^2}\beta_2 = -\frac{\lambda}{c}\frac{d^2n}{d\lambda^2} \quad (2.10)$$

The GVD coefficient β_2 or GVD describes the relative difference between the v_g of higher and lower frequency components of an optical pulse and thus is a critical waveguide parameter for understanding how a pulse propagates in a nonlinear medium. Third β_3 and fourth β_4 order dispersion coefficients may also play an important role in ultrashort pulse propagation, especially the coefficient β_3 which is called third-order dispersion (TOD). The GVD can be either positive or negative, and its sign determines the underlying dynamics in SCG, as will be discussed in the next section of the chapter. When $\beta_2 > 0$, the dispersion falls in the normal regime, which means that the shorter wavelengths (high frequencies) of the pulse are propagating slower than the longer wavelengths (low frequencies). That means that the red-shifted wavelengths arrive earlier than the blue ones at the end of the waveguide length, and as a result, a positive chirp -or an up-chirp- is developed across the broadening pulse. On the other hand, when $\beta_2 < 0$ the dispersion is anomalous, and in this regime, the shorter wavelength components of the pulse travel faster than the longer wavelengths. As a result, the pulse develops a negative chirp -or down-chirp. When the condition $\beta_2 = 0$ is fulfilled, the material dispersion cancels the waveguide dispersion, and this position is widely known as zero-dispersion wavelength (ZDW). However, the dispersive effects do not vanish entirely at this wavelength and the TOD coefficient β_3 of the equation (2.7) comes into play [117,123]. Not only the ZDW can be shifted, but the actual dispersion curve can also be sculpted by varying the waveguide dimensions, enabling flexible dispersion engineering, as we'll see in the following figures.
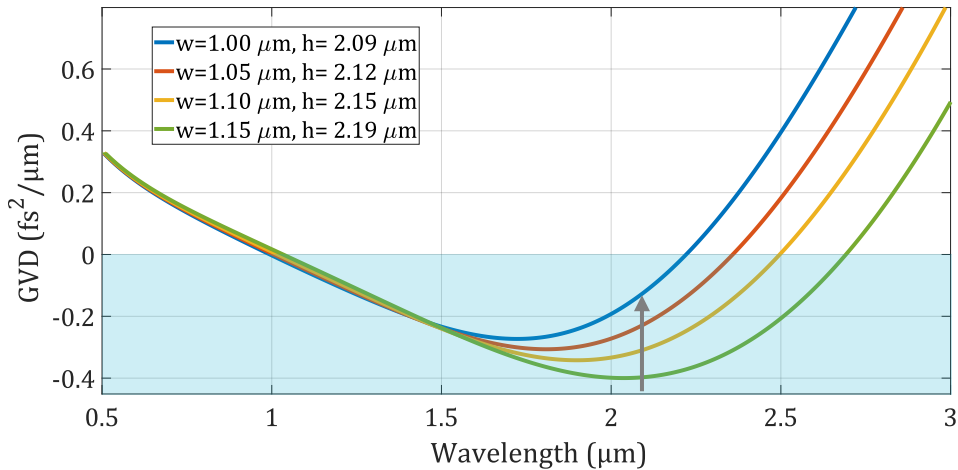
Figure 2.4 Simulated GVD curves for the fundamental TM$_{00}$ mode of four different waveguide geometries. The investigated waveguides have a width of 1.00 μm, 1.05 μm, 1,10 μm, and 1.15 μm respectively and slightly varying heights. The grey arrow indicates the pump's position, and the light blue shaded area represents the anomalous dispersion region.

In Fig. 2.4, the GVD curves of the first category of SiO_2 cladded Si_3N_4 waveguides studied in the thesis are presented. The curves are derived from the wavelength-dependent n_{eff} extracted from the model in COMSOL for the fundamental TM_{00} mode.

We can clearly observe that two ZDWs appear within the spectral range between 0.5 μm and 3 μm, and the ZDW lying in the mid-IR region beyond 2 μm can be red-shifted by increasing the waveguide's cross-section. Moreover, the dispersion is anomalous for the entire spectral region between the two ZDWs. The pump used in the experiments presented in chapter 3 falls into the anomalous regime, determining the underlying SCG dynamics. Similar behavior is observed for the fundamental TE_{00} mode so that the waveguides exhibit anomalous GVD for the pump wavelength in both TM/TE modes.

On the other hand, in Fig. 2.5, the GVD curves corresponding to the second category of air-cladded waveguides studied in the last part of the thesis are shown. As we can observe, two ZDWs appear again in the same wavelength range. However, the interesting thing is that for this uncladded Si_3N_4 design, the TE and the TM mode's dispersion sign changes at the pump wavelength of interest. The dispersion falls into an anomalous regime for TE mode excitation while it is normal for the TM polarization mode. This enables switching between different dispersion profiles and consequently SCG mechanisms by simply adjusting the polarization state.
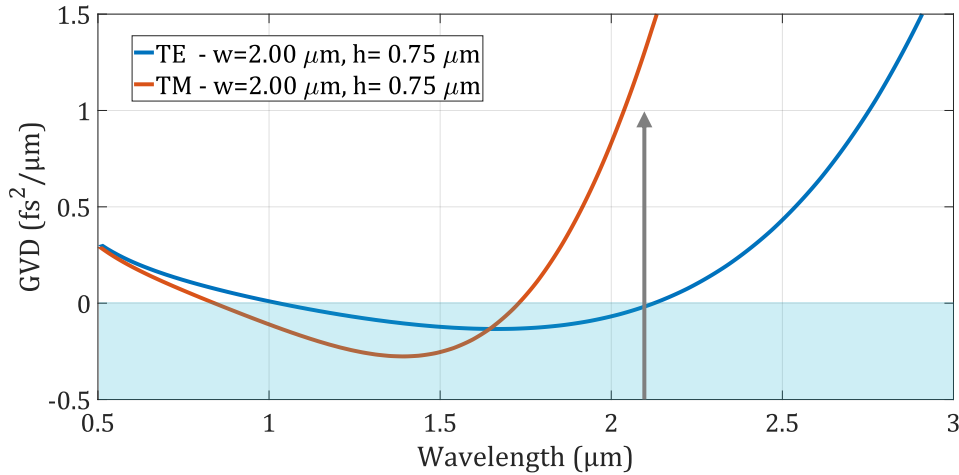
Figure 2.5 Simulated GVD curves for the fundamental TE_{00} and TM_{00} modes for the uncladded waveguide design. The investigated waveguide has a width of 2.00 μm and a height of 750 nm. The grey arrow indicates the position of the pump, and the light blue shaded area highlights the anomalous dispersion region.

As we have seen, these simple rectangular Si_3N_4 waveguide structures allow remarkable control of the dispersion by simply varying the waveguide's dimensions and design, and this is the definition of dispersion engineering: the ability to design and precisely control the dispersion profile of a waveguide through its geometry [124].

2.2 Supercontinuum Generation (SCG)

Supercontinuum generation (SCG) has become an unambiguously important phenomenon of modern nonlinear optics, as seen in the first chapter of the thesis. Nowadays, the prospect of miniaturizing SC light sources is driving experiments in different integrated platforms such as our dispersion engineered Si_3N_4 waveguides. In general, SC is generated when an ultrashort and sufficiently intense pulse is injected into a nonlinear medium. The result of this interaction is the generation of new frequencies around the pump wavelength and thus a very broad spectrum [117]. The physical mechanisms responsible for SCG are highly dependent on the pump pulse duration and the dispersion profile of the pumping medium. In our case, the study is focused only on femtosecond pulses. An interplay of multiple nonlinear optical effects such as the self-phase modulation (SPM), optical wave breaking (OWB), soliton fission with dispersive wave generation (DWG), and stimulated Raman scattering (SRS) contributing to the SCG increases the whole process's complexity. As a result, it is not straightforward to estimate a SC source's key properties such as the optical bandwidth, the temporal coherence, and the spectral density on a specific wavelength region. All of these properties are strongly dependent on the SCG's governing nonlinear mechanisms, and their optimization relies on proper dispersion engineering, suitable for the particular application of the SC source.

This section of the chapter presents the general form of the equation describing the pulse propagation in an optical waveguide and gives insights into the dominant nonlinear mechanisms responsible for SCG under femtosecond pulse excitation. The underlying SCG dynamics are the basis for explaining the experimental results presented in Chapters 3 and 5 of the dissertation.

2.2.1 Generalized Nonlinear Schrödinger equation (GNLSE)

To model the nonlinear pulse propagation in optical waveguides, it is necessary to include both linear and nonlinear optical effects. To do so, starting from Maxwell's equations in the slowly varying amplitude approximation and a modified version of the wave equation, one can derive the generalized nonlinear Schrödinger equation (GNLSE).

The GNLSE is used to simulate the pulse propagation in a waveguide and can be written in the form of [125] :

$$\frac{\partial A}{\partial z} = \underbrace{- \frac{\alpha}{2}A}_{\text{linear loss}} + \underbrace{\sum_{m \geq 2} \frac{i^{m+1}}{m!} \beta_m \frac{\partial^m A}{\partial T^m}}_{\text{dispersion}}$$

$$\underbrace{+i\gamma}_{\text{Kerr effect}} \underbrace{\left(1 + i\tau_s \frac{\partial}{\partial T}\right)}_{\text{Self-steepening}} \left(A(z,t) \underbrace{\int_{-\infty}^{+\infty} R(T')|A(z,T-T')|^2}_{\text{Raman effect}}\right) dT' \qquad (2.11)$$

where $A(z,t)$ is the pulse envelope along the z-axis of propagation in the waveguide in the co-moving time frame $T = t - \beta_1 z$.

The different terms in the GNLSE equation are underlined with brackets of different colors to explain the physical representation of each term. The first term over the blue bracket corresponds to the linear loss α during propagation, while the term underlined with red bracket corresponds to the mth order of dispersion, β_m, calculated by equation (2.7). Terms on yellow and purple brackets correspond to the third-order nonlinear effects and self-steepening effects, respectively. The nonlinear parameter γ, which expresses the strength of the third-order nonlinear effects, is linked to the effective mode area and is calculated by:

$$\gamma = \frac{n_2 \omega}{A_{eff}\, c} \qquad (2.12)$$

The shock term τ_s characterizes the self-steepening effect -an effect originating from the intensity-dependent refractive index- and is calculated by the frequency dependence of A_{eff} and the effective refractive index n_{eff} as:

$$\tau_s = \tau_0 - \left[\frac{1}{n_{eff}(\omega)}\frac{dn_{eff}(\omega)}{d\omega}\right] - \left[\frac{1}{A_{eff}(\omega)}\frac{dA_{eff}(\omega)}{d\omega}\right] \qquad (2.13)$$

The last term (green bracket) of the GNSE describes the Raman effect, which is linked to the photon-phonon interaction in the optical material when the injected photons interact with the molecular vibrational modes. As a consequence of this interaction, part of the photon energy is transferred to an optical phonon, causing a red-shifting in its wavelength. Raman effect is represented by the delay term in the response function $R(T)$ [87]:

$$R(T) = (1 - f_R)\delta(T) + f_R h_R(T) \qquad (2.14)$$

where f_R is the contribution of the delayed Raman response to the instantaneous electronic response of the material, $\delta(T)$ is the delta function and h_R is the Raman response function. The Raman response function is extracted by the Raman shift of the material.

In this thesis, the GNLSE is used to model SCG (Chapter 3 and 5). We do not consider Raman response in the particular model since the Raman effect in Si_3N_4 is negligible compared to SiO_2 [126]. In other words, the Raman effect is neglected in the present thesis' simulations and the f_R is set to zero. As a consequence, $R(T) = \delta(T)$ and the equation (2.11) remains with a simplified term $A(z,t)$ in the integral of the Raman effect. The GNLSE is numerically solved using a split-step Fourier method which solves nonlinear partial differential equations.

The Kerr effect (yellow bracket) and the dispersion term (red bracket) will be discussed in detail in the following sections, since they dominate in our SCG dynamics. Generally, the Kerr effect term includes the self-phase modulation (SPM), and the optical wave breaking (OWB) discussed in subsections 2.2.2 and 2.2.4, respectively. On the other hand, the dispersion term comes strongly into play in the soliton-fission and dispersive wave generation (DWG) presented in 2.2.3.

2.2.2 Self-phase Modulation (SPM)

The response of any dielectric material to an external electromagnetic (EM) field is considered to be linear for low intensities. This response is expressed through the medium's polarization, the dipole moment per unit volume [127]. On the other hand, when the field that interacts with the medium is sufficiently intense, the induced polarization $\vec{P}$ appears to have a nonlinear response to the applied electric field $\vec{E}$ described by the following equation:

$$\vec{P} = \varepsilon_0 \left(\chi^{(1)}\vec{E} + \chi^{(2)} \vec{E}^2 + \chi^{(3)} \vec{E}^3 + \dots\dots \right) \quad (2.15)$$

where ε_0 is the permittivity of the vacuum and $\chi^{(n)}$ is the nth order susceptibility of the material. [117,127,128].

Stoichiometric silicon nitride (Si_3N_4) is an amorphous material with inversion symmetry. As a centrosymmetric material $\chi^{(2)} = 0$ in the dipole approximation, and second-order nonlinear effects can be neglected. In these materials, the dominant nonlinearity originates from the cubic term $\chi^{(3)}$, the third-order nonlinearity. In this dissertation, only the regime of third-order nonlinearities is being explored, neglecting the processes that can cause inversion symmetry breaking in Si_3N_4 and, as a consequence, inducing an effective $\chi^{(2)}$ [129].

The third-order nonlinearity $\chi^{(3)}$ quantifies the strength of various nonlinear processes such as the optical Kerr effect, which is the intensity-dependent refractive index and can be mathematically described, in its simplest form, as:

$$n(\omega, I) = n(\omega) + n_2 I \quad (2.16)$$

where I is the intensity of the electric field E, $n(\omega)$ is the linear refractive index of the material discussed in section 2.1 and n_2 is the nonlinear refractive index given by:

$$n_2 = \frac{3 \chi^{(3)}}{4c\varepsilon_0 n^2} \quad (2.17)$$

The intensity-dependent refractive index of the material, the Kerr effect, produces an additional change in the optical pulse phase when it propagates through the medium. This phase change is proportional to the pulse intensity, and the effect is called self-phase modulation (SPM). This phenomenon leads to the spectral broadening of the initially injected optical pulse as a result of the varying nonlinear phase, φ_{NL} by the temporal intensity profile.

To better understand the SPM effect as a spectral broadening mechanism, we start from the GNSE that governs the pulse propagation in optical waveguides, described by equation (2.11), considering several simplifications. First of all, we consider negligible GVD so that the dispersion term in the equation (2.11) can be set to zero. As a result, the normalized amplitude $A(z, T)$ defined as:

$$A(z, t) = \sqrt{P_0} e^{(-\alpha z/2)} A(z, t) \quad (2.18)$$

can be described by:

$$\frac{\partial A}{\partial z} = \frac{ie^{-\alpha z}}{L_{NL}}|A|^2 A \quad (2.19)$$

We introduce here the nonlinear length, L_{NL} :

$$L_{NL} = \frac{1}{\gamma P_0} \quad (2.20)$$

as well as the dispersion length, L_D:

$$L_D = \frac{T_0^2}{|\beta_2|} \quad (2.21)$$

Different behaviors upon pulse propagation depend on the values of L_{NL} and L_D. Such propagation in a loss-free nonlinear medium results in a power-dependent nonlinear shift $\varphi_{NL}(L, T)$, which accumulated proportionally to power and distance, giving rise to new frequency components:

$$\varphi_{NL}(L, T) = |A(0, T)|^2 \frac{L_{eff}}{L_{NL}} \quad (2.22)$$

The maximum nonlinear phase-shift, φ_{max}, occurs at the center of the pulse, where T=0, and is given by:

$$\varphi_{max} = \frac{L_{eff}}{L_{NL}} = \gamma P_0 L_{eff} \quad (2.23)$$

where P_0 is the peak power of the optical pulse, γ the nonlinear parameter and L_{eff} is the effective length of a waveguide's length L defined as:

$$L_{eff} = [1 - e^{(-\alpha L)}]/\alpha \quad (2.24)$$

We can see now that the nonlinear length is the length resulting in an additional nonlinear phase shift of 1. The spectral changes and the creation of new frequencies induced by SPM are a direct consequence of the power and time dependence of the phase-shift φ_{NL}. The instantaneous frequency is given by:

$$\partial\omega\,(T) = -\frac{\partial\varphi_{NL}}{\partial T} = -\varphi_{max}\,\frac{\partial}{\partial T}\,|A(0, T)|^2 \quad (2.25)$$

where $A(0, T)$ is the normalized pulse shape at the input ($z = 0$).

The instantaneous frequency $\partial\omega\,(T)$ is usually referred to as the frequency chirp of the pulse. As a consequence, the frequency is shifting, driven by the slope of the pulse power at a time T, and the pulse transfers part of its energy to the spectral sidebands $\omega_0 \pm \delta\omega$ which broadens the pulse spectrum.

In Fig. 2.6, a schematic of the SPM is illustrated for a sech[2] pulse profile.
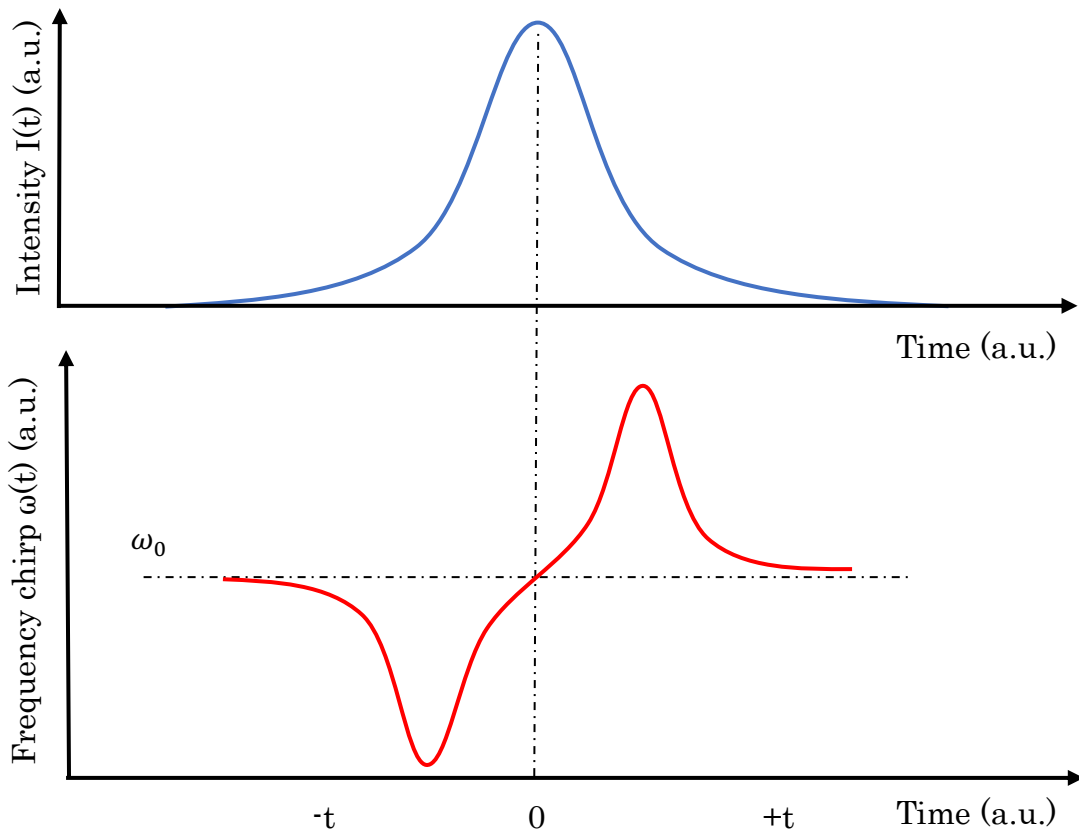
Fig. 2.6 (a) The temporal profile of a sech^2 pulse and (b) the corresponding chirp for a π nonlinear phase shift.

In general, SPM plays a crucial role in various pulse compression processes and optical soliton formation. SPM usually dominates in the first few millimeters of propagation in the waveguide when the pump is located in the anomalous dispersion regime. Simultaneously, it is the principal broadening mechanism in the entire propagation length while pumping in the all-normal dispersion (ANDi) regime.

2.2.3 Soliton-Fission and Dispersive Wave Generation (DWG)

Optical solitons are self-stabilized wave packets that arise from the delicate balance between nonlinear and dispersive effects. Solitons play a fundamental role in nature due to their ability to propagate undistorted -fundamental soliton- over long distances. Their unique properties escape from the boundaries of optics so that solitons can be found in numerous areas of physics, such as hydrodynamics [130,131], astrophysics [132], and biology [133]. Focusing on optics, the rich dynamics of non-dispersing solitons enable the generation of supercontinuum spectra covering ultra-wide wavelength ranges from the ultraviolet to the middle infrared [134]. In the anomalous dispersion regime of an optical waveguide, the nonlinear chirp induced by SPM and the linear chirp from GVD can be combined in such a way that they support stable or periodic evolution of optical solitons.

When an ultrashort pulse with a high peak power propagates inside a waveguide in the anomalous GVD regime, the initial pulse evolves in solitons -fundamental or higher-order

depending on the soliton order- which breaks up into a number of fundamental solitons during propagation. The soliton propagation can be perturbed due to high-order dispersion (HOD), leading to a phenomenon called soliton fission, resulting in the breaking up of the initial soliton. Soliton fission is induced by perturbations of the soliton-like pulse, such as HOD, self-steepening, and SRS. However, the self-steepening parameter is the smallest, so usually, HOD initiates the fission and, in our case, the third-order dispersion (TOD) [117]. The behavior of the propagating soliton due to HOD perturbations is highly dependent on its order, N, which can be expressed as a ratio between the nonlinear L_{NL} and the dispersive length L_D.

The soliton number is therefore given by:

$$N^2 = \frac{L_D}{L_{NL}} = \frac{\gamma P_0 T_0^2}{|\beta_2|} \quad (2.26)$$

where T_0 is the pulse duration at full-width at half maximum (FWHM) and P_0 the peak power of the injected pulse. Typically, the ultrashort pulses we refer to are pulses with durations, at full-width at half maximum (FWHM) around 150 fs or even shorter.

Physically, the soliton regime requires the input pump to be in the anomalous GVD region of the waveguide, and at the same time the L_D to be larger than the L_{NL}, $L_D > L_{NL}$. Consequently, when the soliton number exceeds $N = 1$ where we have the lowest-order soliton solution, soliton-fission can occur. The first soliton-fission point, or compression point, is where the SC starts to get generated. The characteristic length at which the first soliton is compressed is calculated by [135] :

$$L_{fiss} = \frac{L_D}{N} = \frac{T_0}{\sqrt{\gamma P_0 \beta_2}} \quad (2.27)$$

The emission of resonant dispersive waves (DWs) by soliton-like pulses -the analogous of Cherenkov radiation in nonlinear optics- is one of the principal mechanisms of nonlinear wavelength conversion in an optical waveguide [136]. After the soliton fission, the higher-order soliton is split, and the main high power soliton ejected can lead to the generation of DWs.

DWs are linear waves that can propagate in-phase with a soliton pump inside any dispersive medium. However, their amplitude is negligible until the phase-matching condition is fulfilled, so their resonant amplification appears in the spectrum.

The phase-matching condition between the DW of a frequency ω, located in the normal dispersion, and the soliton-like pulse of a frequency ω_s is given by [117] :

$$\beta(\omega) - \beta(\omega_s) - \frac{1}{v_g}(\omega - \omega_s) = \frac{\gamma P_0}{2} \quad (2.28)$$

where β is the propagation constant as we have already seen, ω_s the central frequency of the solitonic pulse, v_g the group velocity of the soliton and γ is the nonlinear parameter calculated by (2.12).

In the phase-matched locations predicted by equation (2.28), the group velocity of the soliton pulse equals the velocity of the linear generated waves. The nonlinear phase shift is minor in the case of anomalous dispersion pumping, and the term γP_0 is usually neglected. The left side of equation (2.28) is called integrated dispersion, β_{int} and can be rewritten as a Taylor expansion in the form of the following equation, where m is the mth order of dispersion:

$$\beta_{int} = \sum_{m \geq 2} \frac{(\omega - \omega_s)^m}{m!} \frac{\partial^m \beta}{\partial \omega^m} \bigg| \cong 0 \quad (2.29)$$

The integrated dispersion curves play a crucial role in the efficiency of the nonlinear wavelength conversion process, as will be discussed in chapter 3. This is because they not only theoretically predict the positions of the generated DWs, but they give an indication if the conversion efficiency towards the DW wavelengths will be increased or decreased.

Moreover, the locations where the phase-matched DWs will appear are highly sensitive to the waveguide's geometry and dimensions, as shown in the next chapter of the thesis. Finally, it is worth mentioning that the number of ZDW points in the GVD profile of a particular waveguide indicates the number of possible DWs when pumping with femtosecond pulses in the anomalous GVD regime [137].

Generally, SCG based on dispersive wave generation (DWG) is much broader than an SPM-driven one. This extended bandwidth enables multi-octave-spanning SC sources for soliton-driven underlying dynamics and limited spectral bandwidth in SPM dominated ones. However, they are much more sensitive to the noise, such that the coherence of an anomalous-dispersion SC can be degraded while SPM-based SC maintains a high level of coherence for most short pulse regimes. Trade-offs between the different generation regimes are discussed in chapter 5.

2.2.4 Optical Wave Breaking (OWB)

Last but not least, the broadening mechanism of optical wave breaking (OWB) is briefly discussed. This phenomenon arises from a combination of the SPM and GVD effects when the pump wavelength is in the all-normal dispersion regime (ANDi) of the waveguide. Both GVD and SPM impose a frequency chirp as a pulse travels in the waveguide. However, as seen by equations (2.20) and (2.25), despite the fact that the GVD-induced chirp is linear in time, the SPM-induced chirp is far from being linear across the entire pulse [117]. As a result, in the case of normal GVD ($\beta_2 > 0$) the red-shifted part near the leading edge travels faster and overtakes the forward tail of the pulse, while the opposite happens for the blue-shifted wavelengths. When SPM and GVD act together, the GVD acts on the already increased spectral width caused by the SPM to increase the pulse's temporal width further. This results in a quite rectangular temporal pulse shape and a linear frequency chirp over most of the pulse. It has been shown that the OWB phenomenon is advantageous for pulse compression with a grating pair [138].

2.3 Absorption Spectroscopy

Spectroscopy is a fundamental tool that studies the interaction between matter and electromagnetic radiation. Spectroscopy is thus crucial for identifying the signatures of molecules and determining precisely their concentration. Specifically, since its inception in the early 1980s, laser absorption spectroscopy has been a well-established and powerful technique for quantitatively resolving molecular linewidths [31,139]. Generally, when a sample interacts with an incoming light at a specific wavelength, part of the energy is absorbed by the sample. As a result, the molecules will be excited to higher energy levels. Molecules possess discrete quantized vibrations and rotations, which lead to unique absorption spectra and intensities and are known as spectral signatures or "fingerprints," as we introduced in the first chapter. Absorption spectroscopy has been rigorously studied in gas-phase species, enabling their identification and concentration quantification. One of the most common and most straightforward approaches for spectroscopy is the direct (or conventional) absorption spectroscopy based on a light source that interrogates a cell containing the gas-phase sample and measuring the power intensity at the cell's output. This simple technique was schematically presented in Fig. 1.3 of chapter 1.

2.3.1 Beer-Lambert law

Direct absorption spectroscopy is governed by the Beer-Lambert law, the most critical law in optical spectroscopy for the qualitative and quantitive interpretation of the spectroscopic data. It links the transmitted optical intensity to the initial laser intensity used to interrogate the sample and the absorbing medium's concentration. The law is expressed in the form of the following equation:

$$I(\lambda) = I_0(\lambda)e^{-\alpha(\lambda)L} \quad (2.30)$$

where $I_0(\lambda)$ is the incident light intensity at a given wavelength λ , $I(\lambda)$ is the intensity transmitted through a medium with a length L (usually a cell unit which contains the gas-phase species) and $\alpha(\lambda)$ is the wavelength-dependent absorbance of the sample [139].

The absorption coefficient $\alpha(v)$ for a molecular transition between energy levels with population densities N_i and N_k and statistic weights g_i and g_k is related to the absorption cross-section $\sigma(v)$ and is given by the following equation:

$$\alpha(v) = [N_i - (g_i/g_k)N_k]\sigma(v) \quad (2.31)$$

where $\sigma(v)$ is the absorption cross-section of the molecule (in cm^2) for the fundamental transition $E_i \rightarrow E_k$ and N_i and N_k are the population densities at the energy levels E_i and E_k of the absorbing molecule. The statistical weights g_i and g_k determine the molecular transition from the lower to the upper level [139]. The absorbance that is frequently used is the absorption coefficient normalized to the cell's length as:

$$\alpha(v) = -ln\left(\frac{I(v)}{I_0(v)}\right)/L \quad (2.32)$$

HITRAN (high-resolution transmission) is the most famous molecular absorption database [140]. This online library of spectroscopic parameters is widely used to simulate a particular gas-phase molecule's absorption (or emission) lines. Parameters given in HITRAN are the frequency of a specific molecular transition given in wavenumber v units (cm^{-1}), the intensity of the transition - which is proportional to the strength S of the transition- and the broadened half-widths. Having extracted all these parameters and applying the aforementioned Beer-Lambert law, the absorption spectra of a targeted molecule can be simulated in a given path/cell. The reference temperature in HITRAN is 296 K. There are other molecular databases such as HITEMP [141], however in the thesis, we use HITRAN's parameters to simulate the molecular absorption lines in chapter 4.

2.3.2 Spectral linewidths and types of broadening – Natural, Doppler, and pressure broadening

The spectral lines corresponding to a distinct energy transition, either absorption or emission, are not entirely monochromatic: they possess a non-zero linewidth. Therefore, they can be broadened and have a specific linewidth around a resonant frequency v_0 where the absorption reaches its maximum. The absorption profile is determined by the frequency-dependent absorption line shape function $I(v)$, which is also known as line profile in the vicinity of v_0 [139].

We introduce here the full-width at half-maximum (FWHM) of a spectral line, which is commonly known as the spectral linewidth, defined as the difference $|\delta v| = v_1 - v_2$ such that: $I(v_1) = I(v_2) = I(v_0)/2$ (138). The spectral linewidth can also be expressed in terms of angular frequency $\omega = 2\pi v$.

One source of broadening is the *natural broadening* or natural linewidth, which arises from the lifetime of the excited states involved in the energy transition. The natural broadening line shape, the basis of absorption line shapes, can be described by the normalized Lorentzian profile given by the following equation:

$$L(\omega - \omega_0) = \frac{\gamma/2\pi}{(\omega - \omega_0)^2 + (\gamma/2)^2} = \frac{1}{\pi} \frac{\delta v_L}{(v - v_0)^2 + {\delta v_L}^2} \quad (2.33)$$

where v_0 is the central frequency of the absorption profile of a molecule, $\gamma = \delta\omega_L$ is the FWHM and $\delta v_L = \gamma /2\pi$.

However, the real molecular absorption linewidth is broader than the natural linewidth. Generally, the natural linewidth described by the Lorentzian profile cannot be observed because of the broadening effects which dominate in most environments. One of the significant contributions to the spectral linewidth at low gas pressures is the Doppler width, which results from the absorbing molecules' thermal motion [139].

The atoms of gas have a distribution of velocities. Each absorbed photon will be shifted by the Doppler effect depending on the atom's velocity relative to the observer. The absorption frequency will be Doppler-shifted according to: $\omega_0' = \omega_0 + \vec{k} . \vec{v}$

where $\vec{k}$ is the wave vector and $\vec{v}$ is the velocity at which the molecule is moving. At the thermal equilibrium, the velocity of the gas molecules follows Maxwell's law of velocity distribution. At a temperature T, the number of molecules $n_i(v_z)dv_z$ in an energy level E_i per unit, volume is given by:

$$n_i(v_z)dv_z = \frac{N_i}{v_p\sqrt{\pi}} \, e^{-(v_z/v_p)^2} dv_z \quad (2.34)$$

where N_i is the density of molecules (total number of atoms) at an energy level E_i, $v_p = (2k_BT/m)^{1/2}$ is the most probable velocity with m the mass of the molecule, k_B Boltzman's constant, and T the temperature. When the temperature of a gas is increased, the distribution of velocities in it becomes wider, and as a result, the spectral line becomes broader.

The absorption frequency will be shifted once the molecules have a velocity component v_z linked to the frequency like this: $\omega_0' = \omega_0(1 + v_z/c)$. This results in an inhomogeneous type of broadening, the *Doppler broadening*, and the intensity profile of a Doppler broadened spectral line will be determined by the Gaussian-like line profile:

$$I(\omega) = I_0 exp\left[-\left(\frac{(\omega - \omega_0)}{v_p \, \omega_0}\right)^2\right] \quad (2.35)$$

with a FWHM $\delta\omega_D = 2\omega_0\sqrt{ln2} \; (v_p/c) = (2\omega_0/c)\sqrt{2RTln2}/M$

where $R = N_A k$ is the gas constant and $M = N_A \, m$ is the mass of a mole where N_A is the number of molecules per mole.

The collisions between the atoms in a gas molecule result in a homogeneous type of broadening of the absorption lines. This collision-induced line broadening is known as *collisional broadening* or *pressure broadening*. The collision probability between the particles is increased as the pressure increases.

Two different types determine the pressure broadening coefficient, the self-broadened HWHM γ_{self} and the air broadened HWHM γ_{air} that are both extracted directly by the HITRAN database. Consequently, the value of collisional broadening δv_c of a gas at a pressure p (atm) at a temperature T and partial pressure of p_{part} is given by [3]:

$$\delta v_c = \gamma_{air}(p - p_{part}) + \gamma_{self}p_{part} \quad (2.36)$$

Broadening mechanisms can act either independently or as a combination. The combination of the thermal broadening (Doppler) with the natural or collision (pressure) broadened line profile is called *Voigt* profile and is a convolution of a Lorentz profile and a Doppler profile. The Voigt line profile is used for the spectroscopic analysis in chapter 4 [142].

$$P(x,y) = \frac{1}{\delta v_D}\sqrt{\frac{ln2}{\pi}} \, V(x,y) \quad (2.37)$$

where the Voigt function $V(x, y)$ is given by [142]:

$$V(x, y) = \frac{y}{\pi} \int_{-\infty}^{+\infty} \frac{e^{-y^2}}{y^2 + (x - y)^2} \, dy \quad (2.38)$$

where x is the normalized frequency deviation from the center normalized by the Doppler width $\delta\omega_D$ and y is the ratio of the Lorentzian (natural) width to the Doppler width given by $\sqrt{ln2}\ \delta\omega_L/\delta\omega_D$ [142].

2.3.3 Signal-to-noise ratio (SNR)

One of the essential goals in acquiring accurate spectroscopic measurements is achieving the highest possible signal-to-noise ratio (SNR). SNR provides a way to estimate and quantify the quality of the signal. Noise, in general, is the sum of all the unwanted signals of a measurement arising from several sources, either electrical or optical. Many factors can contribute to the noise and, as a result, to a lower SNR value. In spectroscopy applications, the sources of noise that contribute can be divided into three main categories, as we can see in the denominator of equation (2.39). The SNR compares the average signal power to the average noise power coming from all the possible sources.

The SNR is calculated from the following equation:

$$SNR = \frac{i_{AS}}{\sqrt{i_{th}^2 + i_{sh}^2 + i_{fl}^2}} \quad (2.39)$$

where i_{AS} is the detection signal for spectroscopy, i_{th} is the thermal noise of the detector and the electronics-also known as dark noise, i_{sh} is the shot noise arising from the statistical variation of the number of photons incident to the photodetector, i_{fl} is the flicker noise due to the laser excess noise.

Equation (2.39) can be modified depending on the dominant term in noise contribution while the other terms can be neglected in the SNR calculation.

In absorption spectroscopy, the SNR can be calculated using the peak of an absorption line as the numerator and the square root of the mean square (RMS) of the background signal as the denominator [143].

2.4 Conclusions

In the second chapter, the theory related to the thesis' investigated phenomena is presented, providing the necessary background to understand the effects discussed in later chapters where experimental results are presented. Section 2.1 is devoted to optical modes in nanophotonic waveguides, and then GVD is introduced due to its importance in femtosecond pulse propagation inside waveguides. The significance of dispersion engineering is highlighted because of its role in the tunability of the generated radiation and the dynamics initiating the SCG. In section 2.2, starting from the GNLSE, which is used to simulate the pulse propagation in the waveguide, we review the main underlying mechanisms behind SCG in the femtosecond regime, SPM, soliton fission inducing DWG, and OWB. The last part of the chapter is dedicated to absorption spectroscopy, and some fundamental theory of absorption molecular lines' broadening mechanisms is briefly discussed. The basic theory used in gas detection analysis is presented as well.

Chapter 3

Development of efficient mid-IR supercontinuum in $\mathrm{Si_3N_4}$ waveguides

Development of efficient mid-IR supercontinuum in Si₃N₄ waveguides

The content of this chapter is mainly based on the following publications:

- **E. Tagkoudi** et al. "Efficient mid-infrared dispersive wave generation in dispersion-engineered Si₃N₄ waveguides pumped at 2 µm," *Conference on Lasers and Electro-Optics (CLEO)*, San Jose, CA, USA, paper SW3A.8 (2018) [144].
- D. Grassani, **E. Tagkoudi** et al. "Mid-infrared gas spectroscopy using efficient fiber laser driven photonic chip-based supercontinuum," **Nature Communications**, vol. 10, no.1553, (2019) [145].

3.1 Introduction

Accessing the middle infrared (mid-IR), the molecular functional group spectral region, based on supercontinuum generation has sparked huge research interest. Driving such nonlinear processes based on fiber lasers offers the undeniable advantage of simplicity and robustness: it is a single pass geometry that does not require any additional seed laser and temporal synchronization. Moreover, when CMOS compatible materials are employed, SC-based sources can also be fabricated with lithographic precision and high yield. Recently, mid-IR frequency comb generation based on dispersive waves in silicon nitride (Si₃N₄) waveguides pumped at telecom wavelength established an essential first step towards such compact systems. Yet, the spectral reach and efficiency still fall short for practical implementation, as we have already seen in [110].

In this thesis, the hurdles mentioned above are overcome. A simple turn-key mid-IR SC source made of waveguide components is demonstrated. The mid-IR source is generated on-chip via dispersive wave generation (DWG) in dispersion-engineered stoichiometric silicon nitride (Si₃N₄) waveguides. For the first time, such a source can perform successful mid-IR absorption spectroscopy, as we'll see in chapter 4. In this chapter of the thesis, the efficient and tunable mid-IR SC source development is presented in detail. The synergy between enhanced waveguide design and optimized pumping regime from a femtosecond mode-locked fiber laser that drives the SC process is required to realize the mid-IR source. In particular, this synergy is leveraged to specifically and preferably target the mid-IR, such that most of the light is transferred from the pump to the selected spectral region while less light is lost to unwanted wavelengths. The design focuses on two main parameters. The first one is pumping at the waveguide's anomalous dispersion regime to enable soliton-driven SC dynamics and, thus, a broader spectral coverage. The second parameter is utilizing large-cross section Si₃N₄ waveguides that ensure optimized long-wavelength confinement and successful power transfer up to 4 microns. A record conversion efficiency (CE) of up to 35 % has been recorded by applying this approach.

In the present chapter, four different Si₃N₄ waveguide widths are extensively studied, providing DWs covering the entire 3 – 4 µm spectral range while being pumped at the anomalous dispersion regime with a 2 µm MLL. The chapter focuses on the CE to quantify the useful energy transfer from the seed laser to the DW locations. The wavelength tunability of the generated mid-IR DWs is both experimentally and theoretically predicted, while numerical simulations of the SCG dynamics support the experimental findings.

3.2 Design of efficient mid-IR supercontinuum source

Propagation of sufficiently powerful femtosecond laser pulses in the anomalous GVD region of a nonlinear waveguide induces high-order soliton-driven dynamics. The soliton number N of the pulse is defined as $N^2 = L_D/L_{NL}$, as we have already seen in the second chapter of the thesis, and is linked to the pulse characteristics (the injected power and the pulse width) as well as the medium characteristics (the nonlinearity and the GVD-β_2) [87]. High-order soliton dynamics lead to an initial spectral broadening caused by SPM and subsequent temporal compression proportional to the N number [135]. During this stage, the higher-order soliton can easily decay following any perturbations to the GLNSE, such as by HOD or nonlinear terms, resulting in the fission into fundamental solitons. At this fission –or compression– point, the spectrum is extensively broadened and with the soliton being at its shortest temporal duration, making it highly susceptible to such perturbations. As a result of the perturbation, energy can be transferred from the fundamental soliton to the linear DWs, spectrally shifted from the pump, and located in the normal dispersion regime [87].

The DW generation process can occur at the frequency where the phase velocity of the soliton pulse equals one of the linear waves and is given by the phase-matching condition introduced by equation (2.28) of chapter 2 [118]. The pump wavelength is used in the phase-matching equation to calculate the central angular frequency of the soliton pulse ω_s. To generate DW, the first negative term of integrated dispersion β_{int} of the equation (2.29) has to be compensated by HOD terms (m>2), which affect the amount of power that can be transferred to the DWs [146,147], while the bandwidth of the soliton at the compression point has to overlap this phase matching region. The GVD determines the location of the phase-matching locations, and it has been proven that the number of the generated phase-matched DWs coincides with the number of ZDWs in the GVD curve [147].

The material dispersion of Si₃N₄ can easily lead to a first ZDW point in the near-IR for the fundamental waveguide mode, which is responsible for the DW generation in the visible spectral region. However, in the mid-IR, the large anomalous material GVD has to be compensated by the waveguide's dispersion to reach a second ZDW on the longer wavelength spectral side. This poses two challenges for the efficient light generation of mid-IR DW radiation. The first is that unwanted visible DW is typically efficiently and automatically generated when pumping with fiber lasers due to the first ZDW point. The second challenge is that the weak mid-IR mode confinement significantly increases absorption losses originating from the silica cladding surrounding Si₃N₄ and spectral

broadening up to the long wavelength DW is difficult. As a result, to reach the mid-IR efficiently, the energy transfer towards the visible has to be limited and better long wavelength confinement has to be guaranteed to limit cladding absorption. These requirements can be simultaneously fulfilled by combining a specific waveguide geometry and proper positioning of the pump wavelength.

Large-cross section waveguides are used to tackle the limitations mentioned above, providing better potential for dispersion engineering and satisfying the necessary improvement in mid-IR confinement, compared to more standard cross-sections. In addition, the pump wavelength must be accurately located to carefully shape the integrated dispersion landscape to favor light transfer towards the mid-IR DW at the expense of the visible DW, such shaping is being linked to the signs of the HOD term at the pump wavelength.

In Fig. 3.1, the GVD curves are presented for two different Si₃N₄ waveguide geometries. The procedure of the GVD calculation is described in detail in chapter 2. The blue GVD curve corresponds to the "standard" fabricated waveguides extensively studied in [110], where the height of the waveguide is typically less than 1 micron and the width is larger than the height. With this standard geometry, such waveguides are typically operated in the TE polarization mode. The magenta curve corresponds to a large cross-section Si₃N₄ waveguide with a width of 1 micron and a height that can reach up to 2.2 μm. With this thick geometry, we preferably operate in the TM polarization. Both geometries exhibit two ZDW. The first ZDW is mainly dominated by material properties, and as a consequence, barely differs between the two designs, located near 1 μm. However, for the thick Si₃N₄ waveguide design, the second ZDW is much further red-shifted, located at 2.6 μm, compared to the standard ones, which is at 2.23 μm. This can lead to a mid-IR DW generation deeper in the mid-IR for the same pump wavelength.
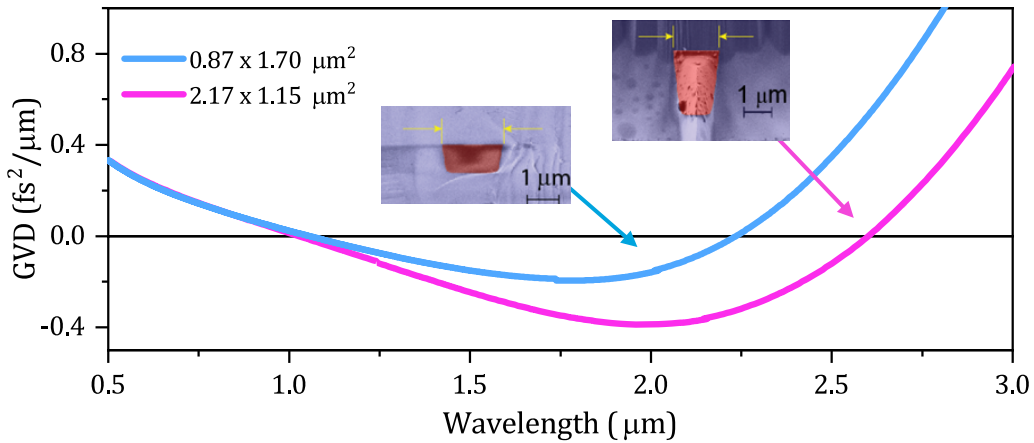
Figure 3.1 Group velocity dispersion (GVD) for the TE fundamental mode of a standard silicon nitride (Si₃N₄) waveguide with cross-section 0.87 × 1.70 μm² (blue) and the TM fundamental mode of a large cross-section waveguide with dimension 2.17 × 1.15 μm² (magenta). The insets show the scanning electron microscope (SEM) images of the waveguide cross-section.

Both waveguide geometries are designed to feature anomalous dispersion at pump wavelengths in the near-IR, easily accessible with fiber lasers.

Simultaneously, the improved mode confinement that large cross-section waveguides exhibit can significantly reduce the mid-IR absorption by the silica cladding. This can be seen in Fig. 3.2, where the absorption losses α as a function of wavelength are computed by including the imaginary part of the refractive index of silica in the COMSOL's numerical simulations [148]. Furthermore, the well-confined mode even beyond 4 µm in the thick waveguide design guarantees a more efficient mid-IR source compared to previously studied designs [110].
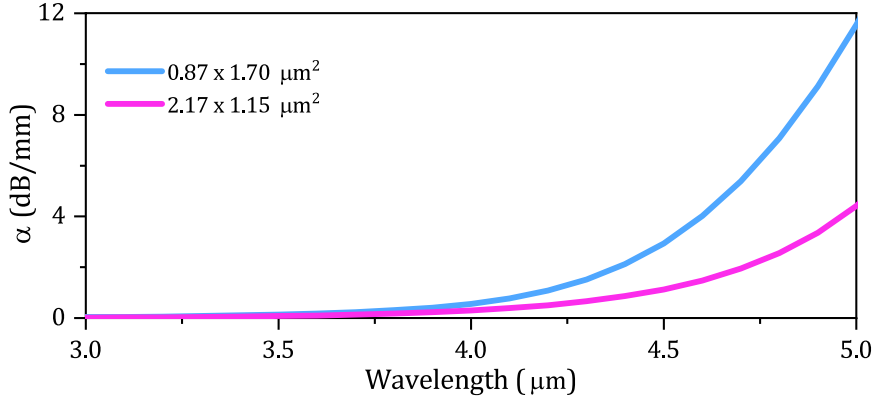
Figure 3.2 Attenuation coefficient α as a function of wavelength for standard (blue) and large cross-section (magenta) waveguides.

High-order dispersion terms also affect the amount of total power transfer to the DWs [146,147]. Specifically, the odd-order dispersion terms lead to an increase -or decrease- of the accumulated integrated dispersion towards one of the two sides of DWG. They favor either the blue or the red-shifted DW, depending on if they are positive or negative valued, respectively [149]. To get a better intuition on the possible efficiency of the power transfer from the pump to the DW either in the visible or in the mid-IR, the integrated dispersion β_{int} is first simulated for different waveguide geometries and for a pump wavelength of 1.55 µm. Fig. 3.3 illustrates the β_{int} curves for a standard (blue) and two different large cross-section waveguide geometries (magenta and yellow for a 1.00 µm and 1.15 µm widths, respectively). This choice is motivated by the previous work done in part in our laboratory ([110]), where a femtosecond erbium-doped fiber laser operating at 1.55 µm was initially used as the pump source.

For the standard waveguide cross-section, the behavior of the integrated dispersion in terms of strength is identical on both sides of the pump: the depth of the "dispersion barrier" is relatively shallow and identical on the blue and red side of the pump. One could expect that the amount of energy transferred from the pump to the phase-matching positions will be close to equally distributed between the visible and the mid-IR generated DWs. From now on, we define symmetry and symmetry breaking as the equally and not equally distributed depth of the integrated dispersion barrier.

On the other hand, pumping the large cross-section waveguides at the same wavelength induces a slight symmetry breaking of the β_{int} curve, more accentuated for the smaller width of large cross-section waveguides. However, at the same time, the mid-IR

dispersion barrier is increased compared to the standard geometry, and thus the power transfer towards the mid-IR will be limited. A break of the symmetry in the integrated dispersion curves means that the amount of the energy transferred from the soliton-like pump to the dispersive waves is not equally distributed and the one dispersive wave is favored against the other. In Fig. 3.3 is clear that the β_{int} curve is symmetric for the standard waveguides, while for the large cross section waveguides is not symmetric anymore in the y-axis.

Moreover, Fig. 3.3 also shows that by pumping a large waveguide with a 1.10 μm width, a mid-IR DW can be generated around 5 μm. Unfortunately, this comes with the price of a much stronger mid-IR dispersion barrier, a large required spectral broadening of the pump as to reach this phase matching point, which means that the pump power would need to be much higher than for the regular cross-section waveguide and as a result, a limited efficiency.
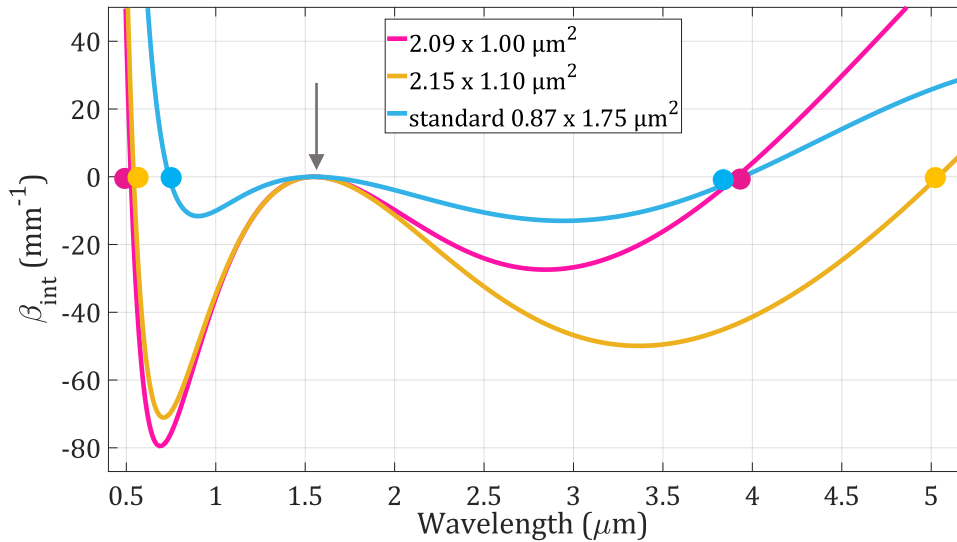
Figure 3.3 Integrated dispersion as a function of wavelength for the standard waveguide pumped at 1.55 μm (blue), and the large cross-section waveguides pumped at 1.55 μm with a cross-section of 2.09 x 1.00 μm² (magenta) and 2.15 x 1.10 μm² (yellow). The phase-matching points lie in the same region for both standard and the smaller large cross-section waveguides. The grey arrow indicates the position of the pump. Bullet points indicate the predicted phase-matching locations.

Simulated pulse propagation spectra presented in Fig. 3.4 confirm this behavior. All simulations are performed for 5 mm long straight waveguides with a cross-section of 0.87 x 1.75 μm², 2.09 x 1.00 μm² and 2.15 x 1.10 μm², corresponding to the ones used in Fig. 3.3. The different waveguide geometries are pumped with a 1.55 μm pump laser with pulse duration (FWHM) of 65 fs and a 5 kW peak power.

As seen in Fig. 3.4 (a), a mid-IR DW is generated at 3.5 μm from a standard waveguide geometry, as predicted from the phase-matched position. Moreover, Fig. 3.4 (b) and (c) show a clear mid-IR generation around 3.7 μm and 4.6 μm for the 1.00 and 1.10 μm wide waveguides, respectively, in clear agreement with the expected spectral positions obtained from the integrated dispersion. Thus, in both cases, even though the DW can be

shifted further into the mid-IR, the efficiency towards this spectral region is very limited. Such behavior was confirmed experimentally [110]: the power transferred to the mid-IR with this scheme was too low to estimate the actual conversion efficiency and limited the use of the source.
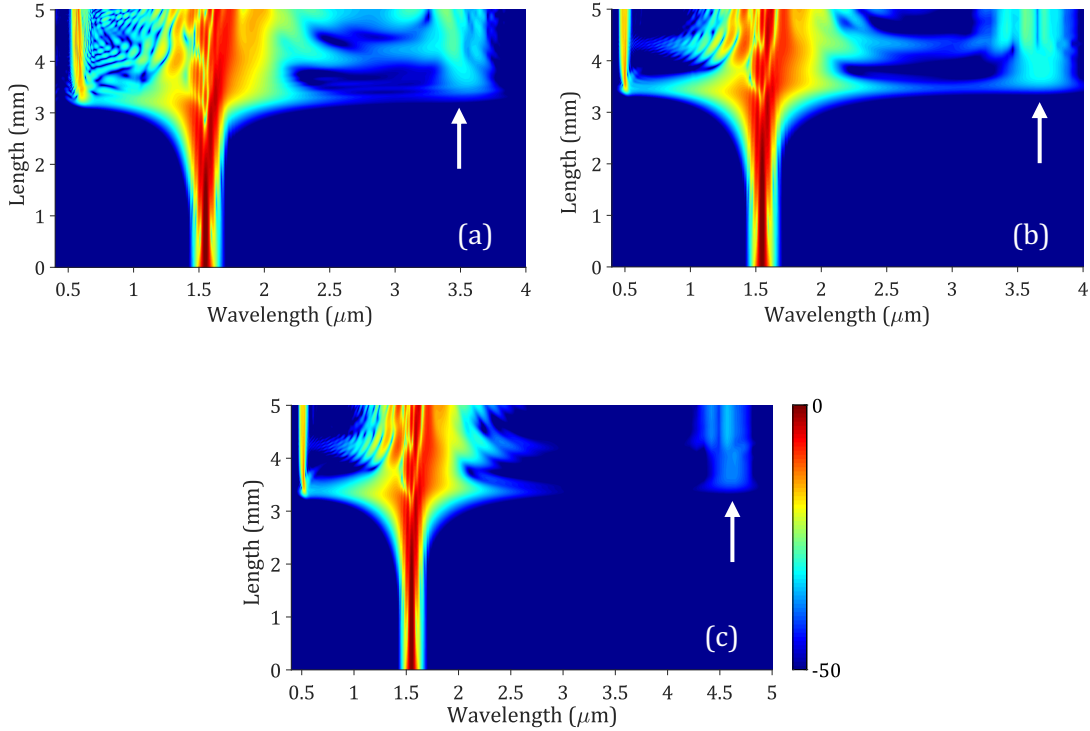
Figure 3.4 Simulated spectral evolution for (a) a 0.87 x 1.75 μm² (height x width) standard cross-section, (b) a 2.09 x 1.00 μm² large cross-section and (c) a 2.15 x 1.10 μm² Si$_3$N$_4$ waveguide pumped at 1.55 μm for a propagation distance of 5 mm. The white arrows indicate the positions of the generated mid-IR dispersive waves. Numerical simulations are performed by solving the GNLSE for the same peak pump power of 5 kW.

In an effort to increase the mid-IR DW generation efficiency and at the same time reduce the visible one, the use of another pump wavelength is investigated. The ideal pump has to both reduce the amount of the accumulated dispersion for the mid-IR DW generation and at the same time provide the required spectral broadening to reach the DW phase matching locations. As such, a longer pump wavelength is needed, and we take advantage of the recent progress in the development of thulium-doped fiber laser operating in the 1.9 – 2.1 μm. The profiles of the β_{int} for a pump positioned at 2.09 μm are simulated and presented at Fig. 3.5 for the same waveguide geometries investigated above. The amount of integrated dispersion separating the pump from the phase-matched DW wavelengths clearly illustrates a much stronger symmetry breaking induced by appropriately positioning the pump wavelength beyond near-infrared wavelengths.

In Fig. 3.5, it is shown that the 2.09 μm pump induces a huge dispersion barrier towards the visible for the two investigated large-cross section waveguides. At the same time, the mid-IR integrated dispersion barrier is much lower for both waveguide cross-sections. As a result, power transfer to the mid-IR spectral region is favored, while the energy transfer towards the visible should be significantly suppressed. For the standard waveguides, the

symmetry breaking is not as pronounced, especially towards the visible DW generation, and as a result, a significant amount of energy could still be transferred to the "unwanted" visible part, as confirmed by simulation presented in Fig. 3.6 (a).
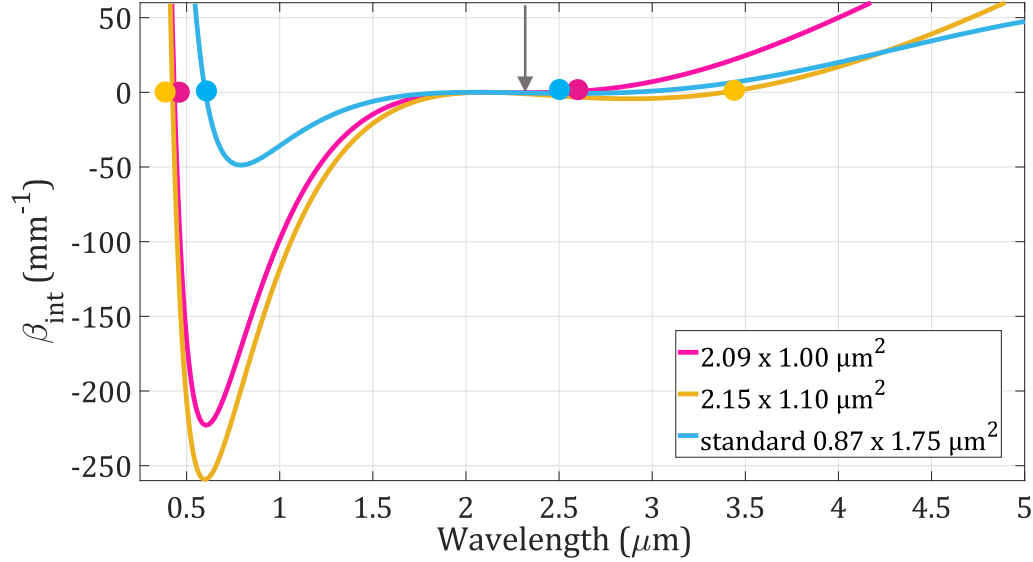
Figure 3.5 Integrated dispersion as a function of wavelength for the standard waveguide pumped at 2.09 μm (blue), and the large cross-section waveguides pumped at 2.09 μm with a cross-section of 2.09 x 1.00 μm² (magenta) and 2.15 x 1.10 μm² (yellow). The grey arrow indicates the position of the pump. Bullet points indicate the theoretically predicted phase-matching positions.

Once again, numerical simulations of the pulse propagation in the waveguides using a 2.09 μm pump with the same 5 kW of peak power and a pulse duration of 78 fs (FWHM) support the correlation between symmetry breaking in β_{int} and power transfer. Fig. 3.6 presents the simulated spectral evolution for standard (a) and large cross-section (b)-(c) waveguide geometries. It is noticeable that pumping the large cross-section waveguides at 2.09 μm, mid-IR DWs are generated at the same wavelength range as for the 1.55 μm pumping. However, for the case of a 2.09 μm pump, the generated mid-IR DWs are highly efficient while much less light is transferred on the short wavelength side, as seen in Fig. 3.6 (b), (c). On the contrary, for a standard waveguide geometry, a 2.09 μm pump results in a weak mid-IR DW and a very strong visible spectral part.

To summarize, there is a clear trade-off between spectral reach and energy transfer linked to the pump positioning. Generally, the larger is the spectral span that must be covered, the lower is the power transferred in the targeted region for a given pump power and, thus, the conversion efficiency. With a careful selection of the pump wavelength, the energy tunneling from the pump to unwanted spectral bands can be significantly reduced. At the same time, the power transfer in a region of high interest, such as the mid-IR, can be enhanced considerably. We can note that a similar approach could also be followed to favor the visible side of the spectrum compared to the mid-IR if a targeted application should require such behavior.
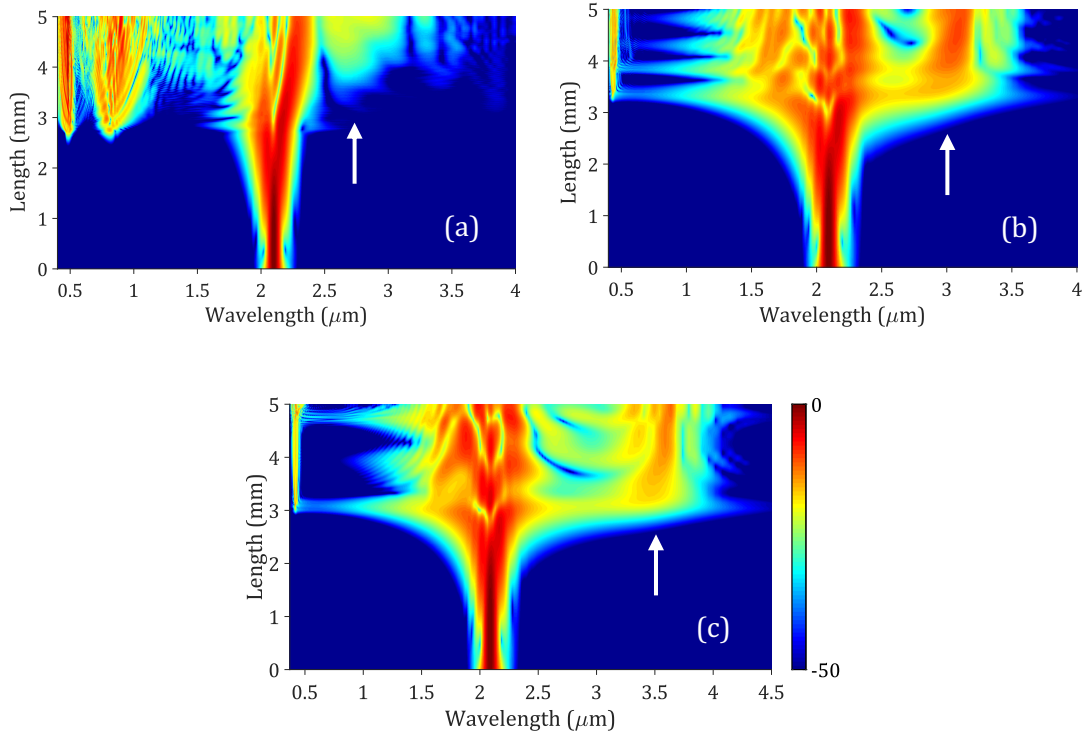
Figure 3.6 Simulated spectral evolution for (a) a 0.87 x 1.75 μm² (height x width) standard cross-section, (b) a 2.09 x 1.00 μm² large cross-section and (c) a 2.15 x 1.10 μm². Si₃N₄ waveguides pumped at 2.09 μm for a propagation distance of 5 mm. The white arrows indicate the positions of the generated mid-IR dispersive waves. Numerical simulations are performed by solving the GNLSE for the same peak pump power of 5 kW.

3.3 Experimental Implementation

3.3.1 Experimental setup

The experimental setup used for confirming the expected behavior of the supercontinuum source is presented in Fig. 3.7. The pump source is a commercial, turn-key soliton self-frequency shifted Thulium-doped fiber MLL (NOVAE Brevity λ+,) with a pulse duration at full width at half maximum (FWHM) of approximately 78 fs and a measured repetition rate of 19 MHz. Polarization management of the injected beam is carried out through a combination of a quarter-wave plate (QWP) and a half-wave plate (HWP). Output power is controlled by a variable optical attenuator (VOA).

Light is coupled in and out of the waveguide's inverse taper mode converters through two identical aspheric black diamond lenses. The beam size after the chalcogenide lens is optimized to match the waveguide's mode field diameter (MFD) as better as possible. The collimated light is focused at the device output using a parabolic mirror collimator into an indium fluoride (InF₃) multimode fiber (MMF). Afterward, the spectra are recorded with a Fourier-Transform Optical Spectrum Analyzer (FT-OSA) spanning the entire 1 – 5 μm range (Thorlabs OSA 205C). The chip consists of 5 mm long straight Si₃N₄ waveguides. The top view of the device is acquired with a microscope objective which projects the

image on a visible camera. The scattered green light glowing at the top and in the chip's output confirms the presence of the generated visible DW. The chip is placed on a micrometric translation change, so it is straightforward and convenient to pump an adjacent waveguide of the same chip.
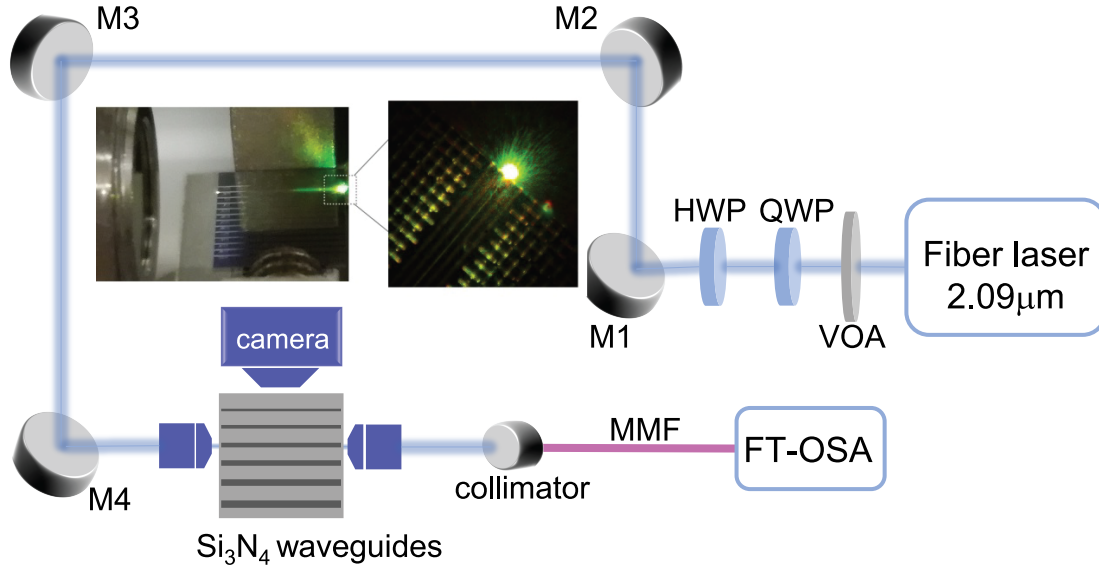
Figure 3.7 Experimental setup. HWP: half-wave plate, QWP: quarter-wave plate, M: mirror, MMF: multimode fiber. The left inset is a picture of the chip and input coupling lens, while the right one is an image of the output of the waveguide taken with the visible top camera. Intense green light scattered out of the waveguide is a signature of the visible DW at 532 nm. Both photos are taken under the same pumping condition for maximum pump power.

The pump laser is coupled in the waveguide's fundamental transverse magnetic (TM) polarization mode to obtain all the experimental results presented in this chapter.

3.3.2 Waveguide fabrication

The chip consists of straight Si₃N₄ waveguides fully buried in SiO₂ cladding, as we can see from the scanning electron microscope (SEM) images presented in Fig. 3.8. The waveguides are 5 mm long, including the two inverse tapered sections for optimum in and out-coupling. In the current thesis, Si₃N₄ waveguides with four different nominal widths are investigated: 1.00 μm, 1.05 μm, 1.10 μm, and 1.17 μm. Thus, the height of the waveguides under test is 2.09 μm, 2.12 μm, 2.15 μm, and 2.19 μm, respectively.

The large cross-section waveguides are fabricated by the K-lab at EPFL according to the photonic Damascene process, which consists of a conformal low-pressure chemical vapor deposition (LPCVD) of Si₃N₄ [150]. The novel fabrication process relies on substrate pre-patterning before the Si₃N₄ core material deposition and the subsequent planarization. In addition to the waveguides, a dense filler pattern is patterned into the silicon (Si) hard mask on a 4 μm thick wet thermal oxide layer of the SiO₂ substrate. This pattern efficiently releases the tensile stress while ensures Si₃N₄ thin film crack prevention. However, even

with such a stress release scheme, the subtracting processing technique can not allow the deposition of a field with thicknesses as shown here. Therefore, utilizing the Damascene process provides a clever solution for fabricating waveguides with larger depth than width, thanks to the conformal deposition. Finally, the Si$_3$N$_4$ core channels are covered by a cladding layer of low-temperature oxide (LTO), and the chip side facets are dry-etched before separating the wafer into individual chips [150].
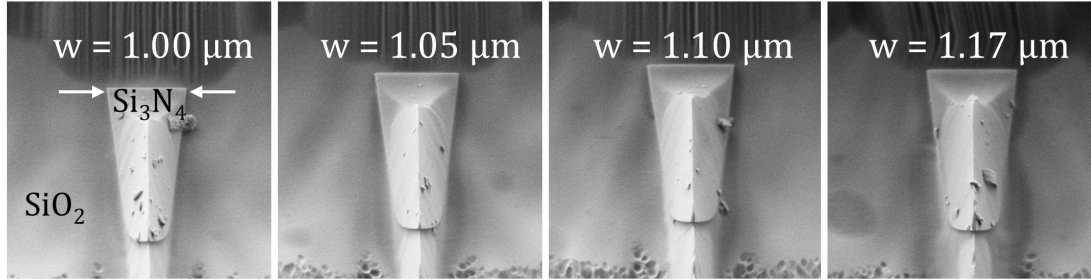
Figure 3.8. Scanning electron microscope (SEM) images of the four investigated Si$_3$N$_4$ waveguides with varying widths from 1.00 μm to 1.17 μm and corresponding heights ranging from 2.09 μm to 2.19 μm, respectively.

The total losses of the waveguides fabricated using the aforementioned technique, including input/output coupling losses and propagation losses, are measured to be 11 dB for the wider cross-section geometries (1.10 μm and 1.17 μm), and 12.5 and 13.5 dB for the 1.05 μm and 1.00 μm waveguides, respectively. Coupling losses are assumed to be equally distributed between input and output waveguide facets. On the other hand, total propagation losses are estimated to be approximately 0.2 dB/cm for the TM propagation mode.

3.4 Evolution and efficiency of dispersive wave generation

In this section of the chapter, the conversion efficiency (CE) of the mid-IR dispersive wave generation is discussed for all four waveguides under test. Before the experimentally measured CE is analyzed, the simulated integrated dispersion curves β_{int} are presented in Fig.3.9 for the four investigated waveguides. From the β_{int} curves, it can be seen that the mid-IR DW phase-matching point is continuously shifted towards longer wavelengths into the mid-IR as the waveguide's width increases. Significantly, in all waveguides, the pump wavelength at 2.09 favors mid-IR DWG, while the large dispersion barrier on the blue side significantly reduces the visible DWG.
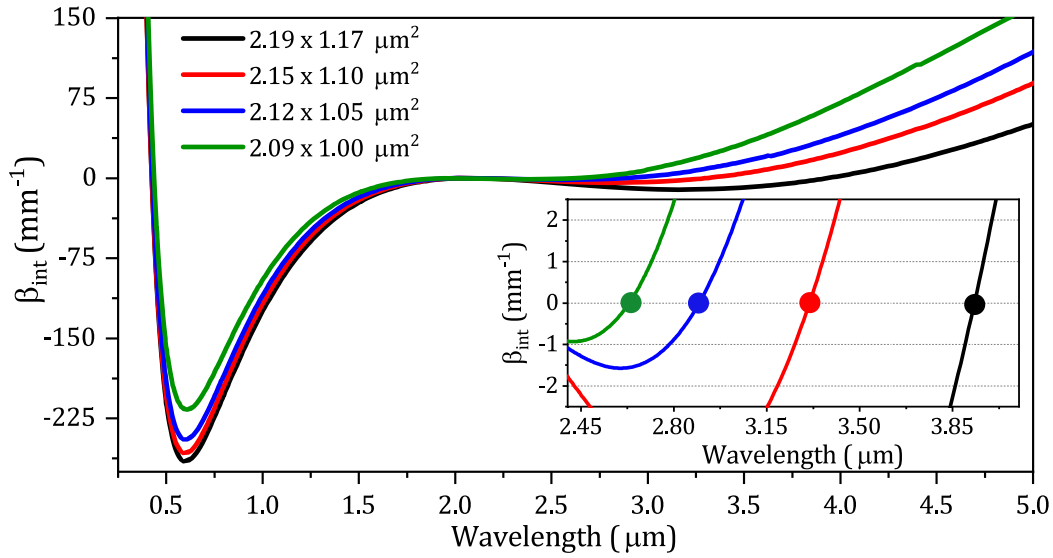
Figure 3.9 Integrated dispersion for the four waveguides under test: 2.09 x 1.00 µm² (green), 2.12 x 1.05 µm² (blue), 2.15 x 1.10 µm² (red) and 2.19 x 1.17 µm² (black). The inset is a zoom-in of the main graph, showing the predicted mid-IR phase-matching points.

The experimental spectra collected at the output of the chip for all the investigated waveguides are presented below. The coupled pump power is estimated to be 13.6 mW. The spectra illustrated in Fig. 3.10 experimentally confirm the theoretically predicted phase-matched positions for the generation of mid-IR DW. In addition, a constant shift of the DW's central wavelength towards the mid-IR is observed by increasing the waveguide's width. The experimentally generated DWs are centered at 3.00 µm (green spectra), 3.22 µm (blue), 3.53 µm (red) and 3.95 µm (black) and correspond to 1.00 µm, 1.05 µm, 1.10 µm, and 1.17 µm waveguide widths respectively.
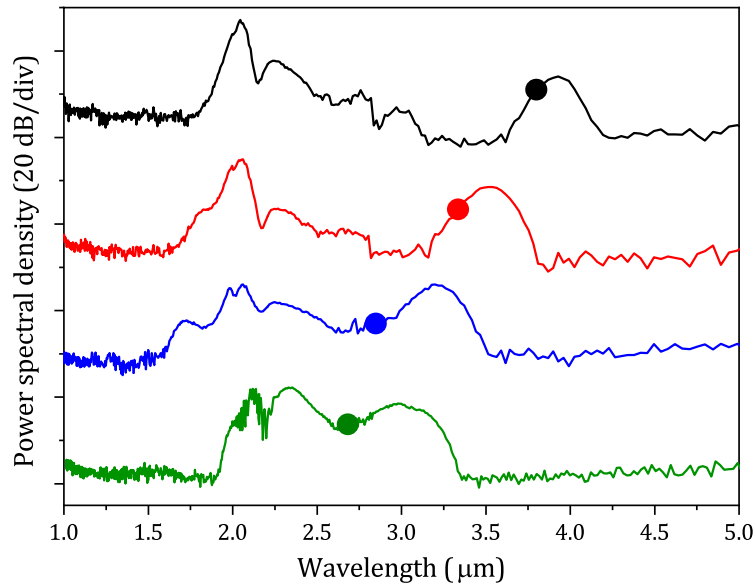
Figure 3.10 Experimental spectra recorded at an estimated average coupled power of 13.6 mW for the four different waveguides under test (same color convention as for Fig. 3.9). Bullet points show the mid-IR phase-matching points predicted by simulations. The results are plotted as a waterfall for clarity.

As a result, by selecting the waveguide width appropriately, the 3 to 4 µm spectral region can be covered entirely on the same chip. However, a mismatch is observed between the theoretically predicted phase-matched wavelengths for the smaller waveguides. This can be attributed to possible variations in the actual waveguide dimensions and uncertainty in the GVD calculation, as obviously the theoretical position of the DW is quite sensitive to the dimensions, and a fabrication tolerance of +/- 20 nm is typical. In Fig. 3.10 presented below, the visible part of the spectrum is not shown, limited by the FT-OSA spectral range. However, measurements of the visible DW are also performed, as will be shown later, confirming that very little light is transferred towards the visible side. The experimental spectra of Fig. 3.10 also show that, apart from the pump broadening due to SPM around the pump wavelength, most of the converted pump energy lies within the mid-IR DW bandwidth. Therefore, to estimate the actual DW power and conversion efficiency (CE), we placed a long pass filter with a cut-on wavelength at 2.5 µm at the waveguide's output before the collimator (see Fig. 3.7).

To quantify the efficiency of the DWG process, the on-chip CE is experimentally retrieved and numerically simulated for all the measured waveguides. The CE expresses the energy percentage seeded from the solitonic pulse to both mid-IR and the visible DWs. To that end, the mid-IR DW power at the chip's output is calculated by integrating the recorded spectrum of the entire DW bandwidth. In this effort, the power measurement in the FT-OSA has to be carefully calibrated.

Utilizing the VOA, the attenuated 2.09 µm pump is coupled in the MMF through the parabolic mirror and is directly sent to the FT spectrometer. Afterward, the value obtained by integrating the entire laser bandwidth in the FT-OSA (P_{FT-OSA}) is compared to the power detected using an InGaAs photodetector (P_{PD}) at the output of the MMF. The ratio $c = P_{PD}/P_{FT-OSA}$ is the calibration coefficient for the measurement. The mid-IR DWs are then integrated over their entire spectral extend, specifically between the frequency ranges of 86–113 THz, 80–110 THz, 76–105 THz, and 70–90 THz for the 1.00 µm, 1.05 µm, 1.10 µm, and 1.17 µm wide waveguides, respectively. These values are multiplied after integration with the calibration coefficient c at the pump wavelength to retrieve the mid-IR DW power at the MMF output. It is crucial to notice that c is constant over the entire FT-OSA's spectral range. Finally, to estimate the total out-coupling losses, transmission through the MMF and the output lens are included, resulting in the on-chip DW power P_{DW}.

The experimental on-chip CE is therefore calculated as the ratio between the on-chip mid-IR DW power over the coupled pump power, $CE = P_{DW}/P_{coupled}$. The coupled pump power, $P_{coupled}$, is estimated by directly measuring the power of the pump laser before the chip, considering only the coupling losses from the input lens. The estimation of the in-coupling losses is under the assumption of symmetric total coupling losses from the in and out-coupling lens.

The experimental results for the on-chip mid-IR DW CE as a function of the coupled pump power are presented in Fig.3.11. In addition, numerical simulations are also shown in Fig. 3.11, supporting the measured efficiencies. Simulations of CE are obtained by integrating

the mid-IR part of the simulated output spectra extracted using the GNLSE. For the simulations, the CE is defined as the ratio between the integral of the entire mid-IR DW bandwidth over the integral of the input spectrum. The on-chip power is then calculated by multiplying the simulated CE by the value of the input pump power used to simulate the spectrum.
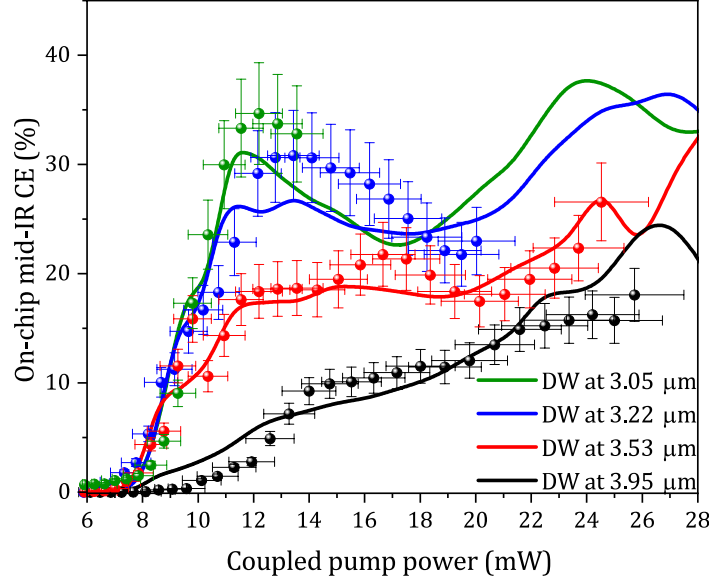
Figure 3.11 Mid-IR dispersive wave generation on-chip conversion efficiency (CE) as a function of the coupled pump power. Scattered points represent experimental data, while constant lines are simulations. Error bars of ±0.5 dBm and ±0.25 dBm represent the standard deviation of repeated measurements of the mid-IR DW and coupled pump powers.

From the CE curves presented in Fig.3.11, the overall CE exhibits three different zones. The first zone is where the DW is not generated yet, meaning that the main soliton has not yet reached the maximal compression due to the low pump power. After this initial stage, a power threshold is observed, which is different for each investigated waveguide. Beyond that threshold, the power coupled in the waveguide is high enough to compress the soliton before the end of the 5 mm long waveguide, leading to the DWG in the soliton compression point at $l_c \propto (1/|\beta_2|P)^{-1/2}$. Given this relation, it is well understood that the soliton undergoes multiple compression points before the end of the chip for the narrow waveguides with a smaller $|\beta_2|$ value, reinforcing the DWG process. Additionally, the spectral broadening at the compression point must be sufficient to overlap with the phase-matched DW wavelengths.

The efficiency of this process increases rapidly while increasing the pump power, reaching record values of 30 - 35 % for the narrow waveguides 1.00 μm and 1.05 μm. On the other hand, the efficiency does not increase as quickly for the wider waveguides and is limited by the large spectral separation between the pump and the DW positions.

Moreover, the wider waveguides have a larger value of $|\beta_2|$ at the pump wavelength of 2.09 μm: 0.31 and 0.4 fs²/μm for 1.10 and 1.17 μm widths, respectively, compared to 0.13 and 0.22 fs²/μm for the 1.00 and 1.05 wide waveguides. As a result, for a specific pulse

peak power and pulse duration, the soliton number is smaller for a waveguide with a larger β_2, given the fact that soliton number is inversely proportional to $|\beta_2|$, $N \propto (P/|\beta_2|)^{-1/2}$. This can limit the compression factor l_c and the number of compression points before the end of the waveguide, leading to less power coupled to the DW. Nevertheless, CE close to 20 % is still experimentally measured. Interestingly, the CE for the 1.00 and 1.05 µm wide waveguides starts decreasing beyond a coupled power of about 12 mW, a behavior confirmed by the simulations.

Thus, a third power level can be identified, which corresponds to the soliton that doesn't have enough power to enable recompression. After this saturation power, the CE has a slight slope and can be considered almost constant. In this region, the soliton can not be further broadened to reach the phase-matching area. It should be noted that the 1.00 µm wide waveguide suffered from higher input coupling loss, which limited the range of coupled pump power, as seen in Fig. 3.11 (green curve). In the waveguide width of 1.05 µm, up to 20 mW could be coupled, while for the wider and less lossy waveguides, 26 mW of average power could be coupled on-chip.

The maximum achievable CE is obtained when the generation of the mid-IR DW happens closer to the pump wavelength, thus for the narrower waveguide, and decreases for a larger waveguide width. This is theoretically predicted as, looking at Fig. 3.9, the mid-IR dispersion barrier increases for larger waveguides.

Finally, the visible DW CE is estimated by replacing the output chalcogenide lens with a silica objective in the output. A short pass filter with a cut-off wavelength at 700 nm substitutes the long pass one right after the chip. The transmitted light is then measured directly on a Si detector. This configuration suffers from higher output losses than the previous one, leading to a larger uncertainty on the measurement. Higher losses can be attributed to strong scattering at shorter wavelengths, which can be noticed by the inset of Fig. 3.7, where the visible DW is scattered out at the top of the chip, giving the characteristic green light. The results for the on-chip CE in the 1.05 µm waveguide are shown in Fig. 3.12 together with the numerical prediction. A very low visible DW generation CE, less than 1.5%, is observed experimentally and in an overall good agreement with theory. The visible DW CE remained well below 4% for all the waveguides under test, confirming the suitable design of the source that suppresses the visible part and significantly favors the mid-IR DW.
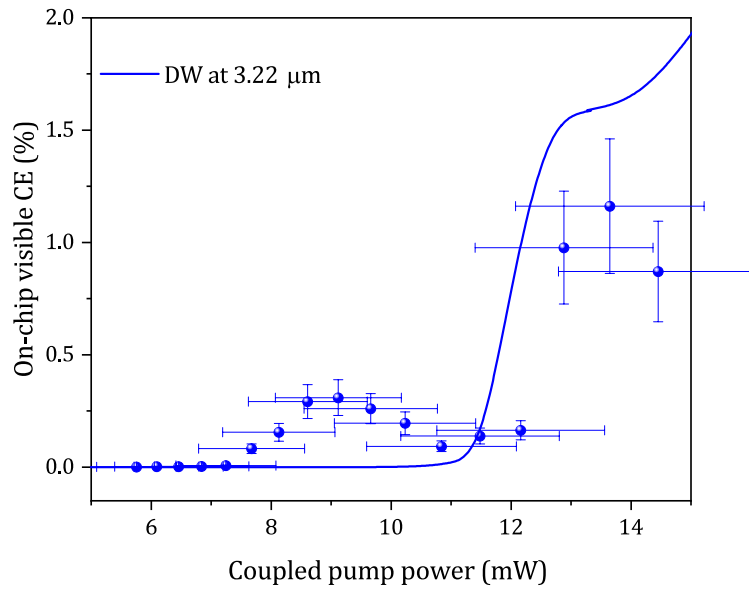
Figure 3.12 Visible dispersive wave CE as a function of the coupled pump power for a waveguide with a cross-section of 2.12 x 1.05 μm². Scattered points represent the experimental data, while the line is the simulated CE. Error bars on the y axis consider ±1 dBm uncertainty on the visible DW power measurement, while error bars on the x-axis represent ±0.5 dBm uncertainty on the coupled power.

Looking at Fig. 3.13, numerical and experimental data of the on-chip mid-IR DW power as a function of the coupled pump power are presented for all the waveguides. It is evident from the graph that all waveguides can generate mid-IR DW with a minimum on-chip power of 4.5 mW, while the maximum reported on-chip power reaches 6.5 mW for a DW generated at 3.53 μm. Specifically, 4.5 mW of on-chip DW power is reached at 3.05 μm with 13 mW pump power, at 3.22 μm with 16 mW of pump power, at 3.53 μm with 22 mW of pump power, and 3.95 μm with 26 mW of pump power. Due to the lower in-coupling losses at the two wider waveguides, more power can be coupled, and stronger mid-IR light is generated at the red-shifted DWs. However, to reach the reported mid-IR powers, higher coupled pump power is required. Thus, there is a clear trade-off between the necessary coupled pump power and the generated DW power, directly linked to the CE.

Increasing the pump power in the 1.05 μm wide waveguide (blue curve) from 12 mW to the 20 mW maximum does not significantly increase DW power. This could be explained by the low values of $|\beta_2|$ in the narrower waveguides, leading to a more extended compression point than in the two larger waveguides. This can also be seen in simulations of the propagating soliton presented in section 3.5.
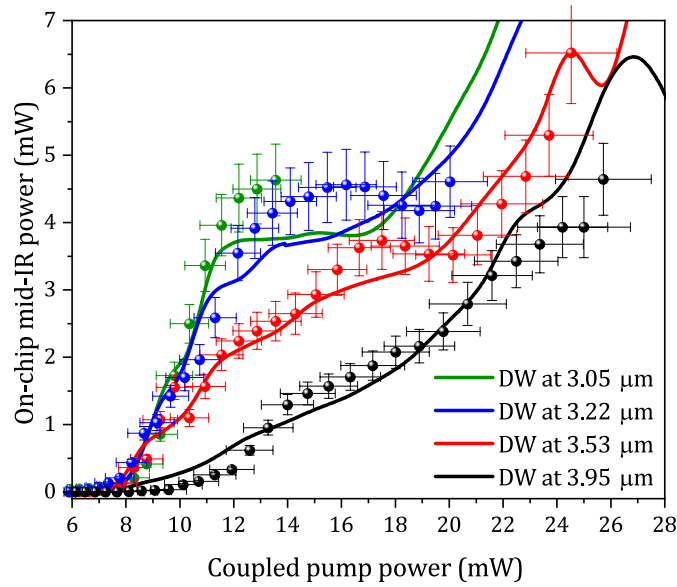
Figure 3.13 On-chip mid-IR DW power estimated from measured spectra. 4.5 mW of on-chip DW power is reached at 3.05 μm with 13 mW pump power, at 3.22 μm with 16 mW of pump power, at 3.53 μm with 22 mW of pump power, and 3.95 μm with 26 mW of pump power.

The highest on-chip mid-IR efficiencies based on DWG on Si_3N_4 waveguides have been measured in the thesis. The record values of more than 35 % at 3.05 μm, 31 % at 3.22 μm, 27 % at 3.53 μm, and 18 % at 3.95 μm, correspond to measured average powers at the chip output of about 1 mW, 1.15 mW, 2.10 mW, and 1 mW, respectively. These values represent a significant improvement compared to previous results [110].

A summary of the most important experimental findings of the DWG and CE study for the four waveguides is presented in Table 3.1. The on-chip mid-IR power corresponds to the maximum average coupled power achieved, while the maximum CE has been reached for lower powers for the DWs closer to the pump, as we have already discussed.

Si_3N_4 waveguide width (μm)	mid-IR DW central λ (μm)	maximum mid-IR CE %	maximum coupled power (mW)	mid-IR on-chip power (mW)	mid-IR output power (mW)
1.00	3.05	35	13.6	4.6	1
1.05	3.22	31	20	4.6	1.15
1.10	3.53	26.6	24.5	6.5	2.10
1.17	3.95	18	25.7	4.65	1

Table 3.1 Summary of the experimental results presented in Fig. 3.10, 3.11, and 3.13. Four different dispersive waves covering the entire 3 - 4 μm spectral region are generated while pumping the investigated waveguides at 2.09 μm. The maximum reported CE for each of them is stated in the third column, while the maximum coupled power and the corresponding mid-IR on-chip power give information for the DWG-based source.

Mid-IR power in the output of each waveguide is estimated by considering out-coupling losses. Overall, more than 1 mW can be reached at the waveguide's output, covering the entire 3–4 μm spectral region. Therefore, by improving the total coupling losses, all the

studied waveguides could reach higher mid-IR efficiencies. As a result, more mid-IR power would be delivered in the chip's output.

Since the SC dynamics are similar for all the studied waveguides, the measured spectral evolution for different input coupled pump powers are presented for the 1.10 μm wide waveguide in Fig. 3.14 below.
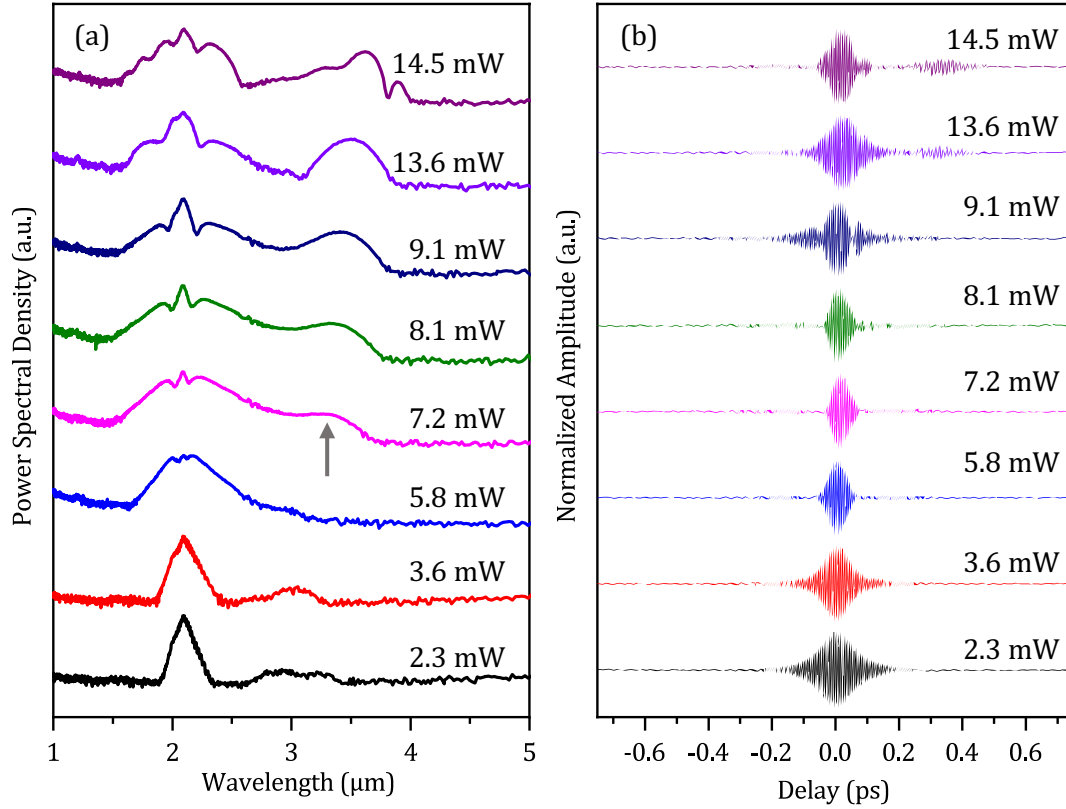
Figure 3.14 Dispersive wave evolution as a function of the coupled pump power. (a) Power spectral density spectra and (b) corresponding autocorrelation traces recorded in the output of the FT-OSA for varying average coupled pump powers.

The initiation of DW generation is detected starting from an average coupled pump power of approximately 7.2 mW and is indicated by the arrow in Fig. 3.14 (a). The DW then grows with increasing coupled pump power while no substantial change in the central soliton spectral region nor the mid-IR DW wavelength is detected. For more coupled pump power, the recorded spectrum does not change significantly, and thus the waterfall plot stops at a power where DW has reached its maximum broadening.

The dispersive wave emission can also be seen from the field autocorrelations presented in Fig. 3.14 (b). As the DW propagates with a different group velocity with respect to the main pulse, two additional interference patterns at a different time delay are observed. The "satellite" pulses indicate the pulse breaking of the fundamental solitons into multiple, and they constitute the signature of DWG in the temporal domain.

3.5 Numerical simulations of the SCG dynamics

Pumping in the anomalous dispersion regime enables soliton fission-driven SCG dynamics, as we have already seen in chapter 2. To better understand the complicated DWG process in the investigated Si$_3$N$_4$ waveguides, numerical simulations are performed. The pulse propagation is simulated based on the generalized nonlinear Schrödinger equation (GNLSE). For the simulations, an input sech^2 pulse with a frequency chirp of -1000 fs^2/2π is considered, leading to a pulse duration of about 110 fs before the entrance of the chip. The laser temporal pulse broadening mainly comes from the dispersion in the wave-plates and the input chalcogenide objective. The spectral dependence of the nonlinear coefficient is included in the model. High-order dispersion (HOD) terms are included up to the 30th order. The dispersion profiles correspond to those shown in Fig. 2.4, calculated using COMSOL Multiphysics. Including more HOD terms does not change the simulation result but increases the computation time significantly. The Raman fraction is set to zero. This can be explained by the negligible Raman response in Si$_3$N$_4$ compared to Raman in SiO$_2$ - experimentally measured in [126] - which results in the absence of Raman-induced soliton fission as well as negligible Raman self-frequency shift in SC generation. Linear propagation losses are also neglected in the model since they are calculated low in simulations (Fig. 3.2). A nonlinear contribution in the experimental in-coupling losses proportional to the coupled pump power to the third power is included to better compare with the experimental results. This particular correction is attributed to the increased multi-photon absorption processes and the consequent free carrier absorption, mainly coming from the rise of visible DW and the generated third harmonic with the pump power.

In Fig. 3.15, the experimental spectra recorded at the output of the four investigated waveguides, presented separately at Fig. 3.10, are compared with numerical simulations. For comparison reasons, the same average coupled pump power of approximately 12.5 mW is used. The choice of the power used in simulations is based on a fair comparison between the experimentally obtained and the simulated spectra. A low soliton number between 4 and 6 is estimated for all waveguides with such coupled power, as pure soliton dynamics are expected to drive the SCG. It has indeed been shown that a soliton number $N > 10$ leads to noise-seeded spectral broadening [117].

Overall, the simulated spectra of Fig. 3.15 reproduce very well the experimental ones. The theoretically predicted mid-IR DW positions match with the measured locations of the experimental ones for all the waveguides. The slight discrepancies in the mid-IR DW positions can be attributed to the variation of the actual waveguide size with respect to the one used in simulations. Fabrication tolerances on lithography can be approximately around 25 nm, and this variation in the waveguide's dimension can tune the phase-matching location, as seen in Fig. 3.9.
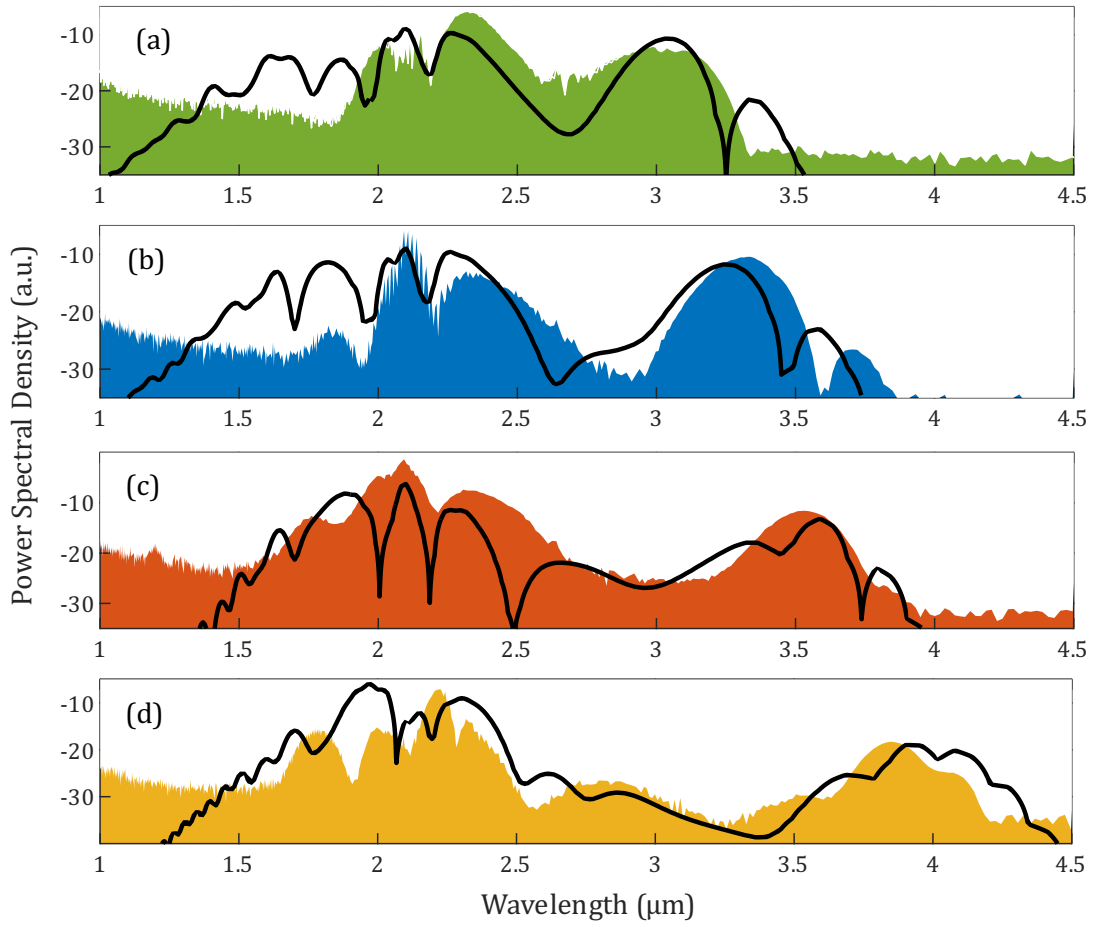
Figure 3.15 Experimental SC spectra measured at the output of the waveguides for maximum pump power (filled colored areas) in comparison with numerically simulated spectra (black lines) for DWs centered at (a) 3.00 µm, (b) 3.22 µm, (c) 3.53 µm, and (d) 3.95 µm, respectively.

Numerical simulations of the pulse evolution within the waveguide are also presented in Fig. 3.16 for the four waveguides under test by considering the same coupled power of 12.5 mW. The parameters used to perform the numerical simulations of the supercontinuum generation are the nonlinear coefficient $n_2 = 2.4 \times 10^{-19} \, m^2 \, W^{-1}$ and the nonlinearity γ, which is estimated for an effective mode area A_{eff} at the pump wavelength. The values of γ and A_{eff} at 2.09 µm for the four different investigated waveguides are obtained by COMSOL simulations and they are presented in Table 3.2. Propagation losses are negligible, and they are not included in the model, so the term which contains the linear loss α in the GNLSE (equation 2.11) is set to zero.

Si₃N₄ waveguide width (µm)	A_{eff} (µm²)	γ (m⁻¹W⁻¹)
1.00	1.41	0.51
1.05	1.86	0.39
1.10	1.92	0.37
1.17	2.00	0.36

Table 3.2 Summary of the values of effective mode area A_{eff} and nonlinear parameter γ used in simulations.
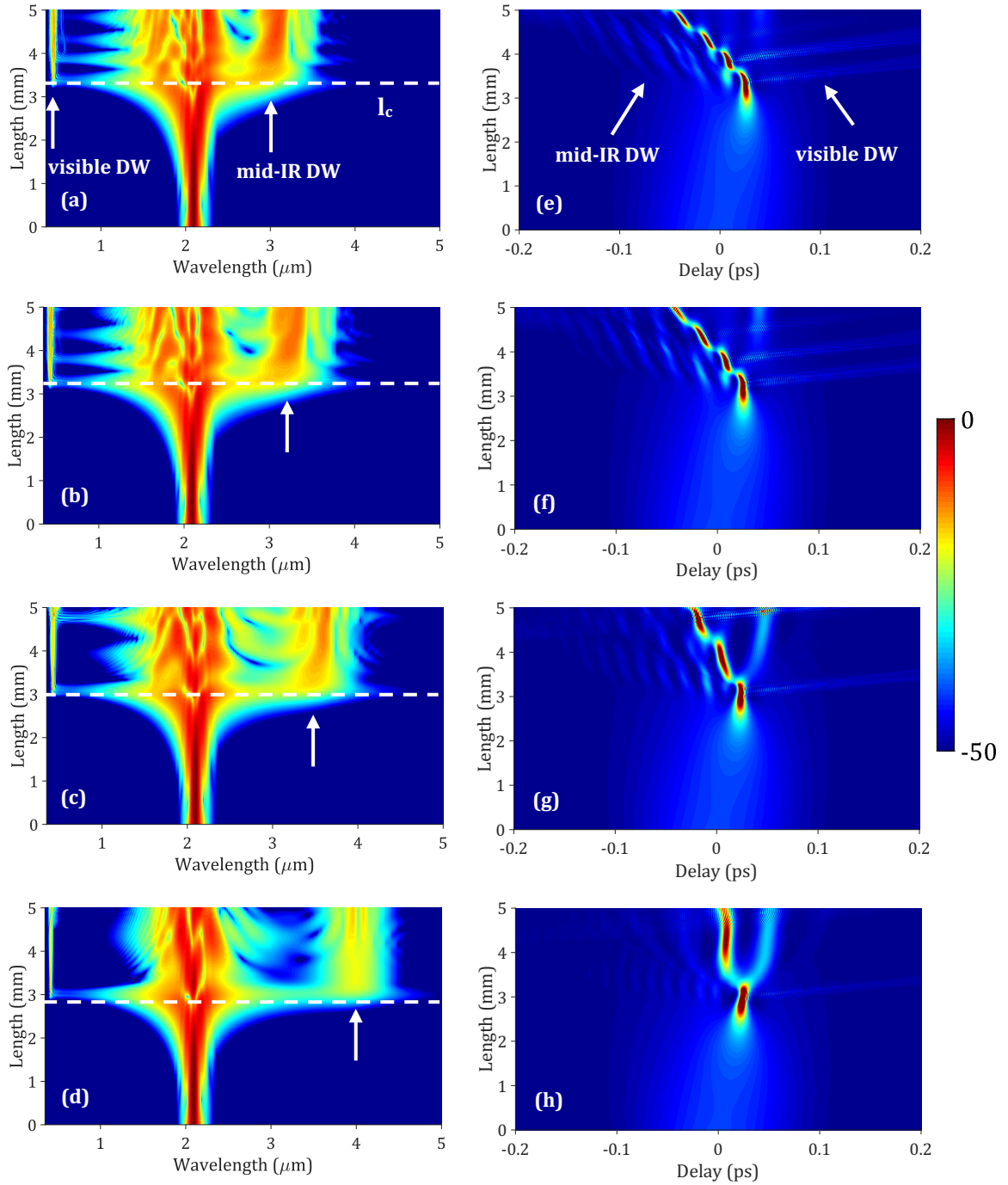
Figure 3.16 Simulated spectral evolution (a) - (d) along the waveguide as a function of wavelength is presented for the four different waveguides under test with DWs at 3.00 μm, 3.22 μm, 3.53 μm, and 3.95 μm from top to bottom. The corresponding temporal evolution is presented on (e) - (h). White arrows indicate the visible and mid-IR positions generated DWs while the dashed white line corresponds to the soliton fission (compression) point.

From the simulated pulse evolution spectra across the propagation length of 5 mm, Fig. 3.16 (a) - (d), we see both the visible and mid-IR dispersive waves generated at the same soliton compression point. Thus, the soliton fission point occurs approximately at l_c = 3 - 3.4 mm for all the investigated waveguides, as indicated by the dashed white line. The l_c point can be visually confirmed by the appearance of strong green light scattered out of

55

the chip at the expected compression point position at the inset of Fig. 3.7. Moreover, Fig. 3.16 (a) - (d) shows that the visible DW at 500 nm is much weaker than the mid-IR DWs in the four waveguides, justifying the measured CE for both visible and mid-IR spectral regions.

Additionally, Fig. 3.16 (a) - (d) shows how, after the first compression point l_c, additional spectral broadening points can occur before the end of the waveguide. The soliton recompression process can be repeated within the length of the waveguide, leading to multiple soliton compression points and thus multiple generations of DWs. This can happen as long as the new soliton pulse has enough energy to broaden spectrally and overlap with the phase-matching locations. The multiple recompression points are separated from each other by a much shorter distance so that this process occurs periodically after the l_c along the 5 mm waveguide.

This process can be noticed in Fig. 3.16 (a) - (d) and is different for each waveguide. For instance, in Fig. 3.16 (a), where the spectral evolution in the 1.00 µm waveguide is presented, the first soliton compression point l_c is found at a slightly longer distance before the end of the waveguide. Moreover, more multiple compression points are exhibited compared to the waveguides with a width of 1.05 µm (b), 1.10 µm (c), and 1.17 µm (d). As a result, the higher is the number of compression points, the more power is seeded to the DWs. This behavior can be understood reminding the smaller value of |β₂| when the waveguide width decreases. Both the soliton fission distance l_c and the soliton number N are inversely proportional to |β₂|, $l_c \propto (1/|\beta_2|P)^{-1/2}$ and $N \propto (P/|\beta_2|)^{-1/2}$.

This link between the β_2, the waveguide dimensions and the underlying SCG dynamics is in absolute agreement with the experimental results presented in Fig. 3.11 and Fig. 3.13. The mid-IR DWG efficiency is already around 30 % for just 12 mW of coupled pump power in the 1.00 µm and 1.05 µm width waveguides. A further increase in the coupled pump power will lead to a higher soliton number and noise-seeded dynamics for DW generation in smaller waveguide cross-sections. On the other hand, the same increase in the injected power results in multiple compression points in larger waveguides, which can eventually reinforce longer DWs.

Table 3.3 summarizes the values of β_2 at the pump wavelength of 2.09 µm, soliton number N, the dispersion length, L_D , and the nonlinear length, L_{NL} , corresponding to this soliton number as well as the soliton compression point l_c obtained by simulations presented in Fig. 3.16 for the four waveguides, showing the link between each other.

Si$_3$N$_4$ waveguide width (μm)	GVD (at 2.09μm) $|\beta_2|$ (fs^2/μm)	Soliton number N	L_D (cm)	L_{NL} (cm)	Soliton-fission point l_c (mm)
1.00	0.13	7.3	2.47	0.046	3.35
1.05	0.22	5.6	1.46	0.047	3.15
1.10	0.31	4.6	1.04	0.049	3.00
1.17	0.40	4.0	0.80	0.050	2.80

Table 3.3 Summary of the simulated values for β_2, soliton number N, corresponding dispersion length L_D, nonlinear length L_{NL} and soliton compression point l_c for the four investigated waveguides. Simulation values for N, L_D, L_{NL} and l_c are all estimated for a peak pump power of 5.5 kW which corresponds to the 12.5 mW of average coupled power.

This behavior of the multiple soliton-compression points can also be understood by looking at the temporal evolution presented in Fig. 3.16 (e) - (h). In fact, for the 1.00 μm and the 1.05 μm width waveguides, the number of recompression points, 4, coincides with the number of pulses in the temporal domain. While for the 1.10 μm and 1.15 μm wide waveguides, the 3 and 2 pulses, respectively, confirm the very few compression points within the propagation length of 5 mm.

Another effect that is more pronounced in the temporal domain is the soliton recoil effect which is slightly observed as a wavelength blue-shift of the fundamental soliton in the spectral domain. Basically, after a first slowdown of the soliton due to the increase of its group index, it accelerates while reducing its delay after the first soliton compression point. This is a characteristic signature of the soliton recoil: as a spectral blue-shift accelerates, a pulse moves towards the mid-IR region. This "bend" of the pulse trajectory is enhanced in smaller waveguides, consistently with the discussion above.

Finally, a power study presented experimentally in Fig. 3.14 is also numerically simulated for the waveguide of 1.10 μm width. The generated mid-IR DW is located at 3.5 μm. In Fig. 3.17 (a) - (d) the spectral evolution is presented for coupled powers of 14.5 mW, 12.5 mW, 10 mW and 7.2 mW, respectively. For this waveguide, the soliton number is estimated to be between 3 and 5 for a coupled pump power of 7.2 mW and 14.5 mW, respectively.

The threshold for a mid-IR DW generation at 3.5 μm is 7.2 mW coupled pump power, supporting the experimentally observed DW threshold at Fig. 3.14. Furthermore, the compression point l_c is shifted to the end of the waveguide for low pump powers, and once the pump power is high enough and the number of compression points increases, it moves towards the middle of the waveguide length. In the temporal domain of Fig. 3.17 (e) - (h), again, the visible and the mid-IR generated DWs appear at the trailing and the leading edges of the time window, respectively, since they propagate with a reduced and increased group delay compared to the pump. As a result, the different propagation speeds of the two simultaneously generated DWs, lead to negative times in the temporal window for the mid-IR DW, while the visible DW is located in positive times since it propagates with an increased group delay compared to the pump.

This behavior is observed after the threshold for the first compression point and is more pronounced after many compression points.
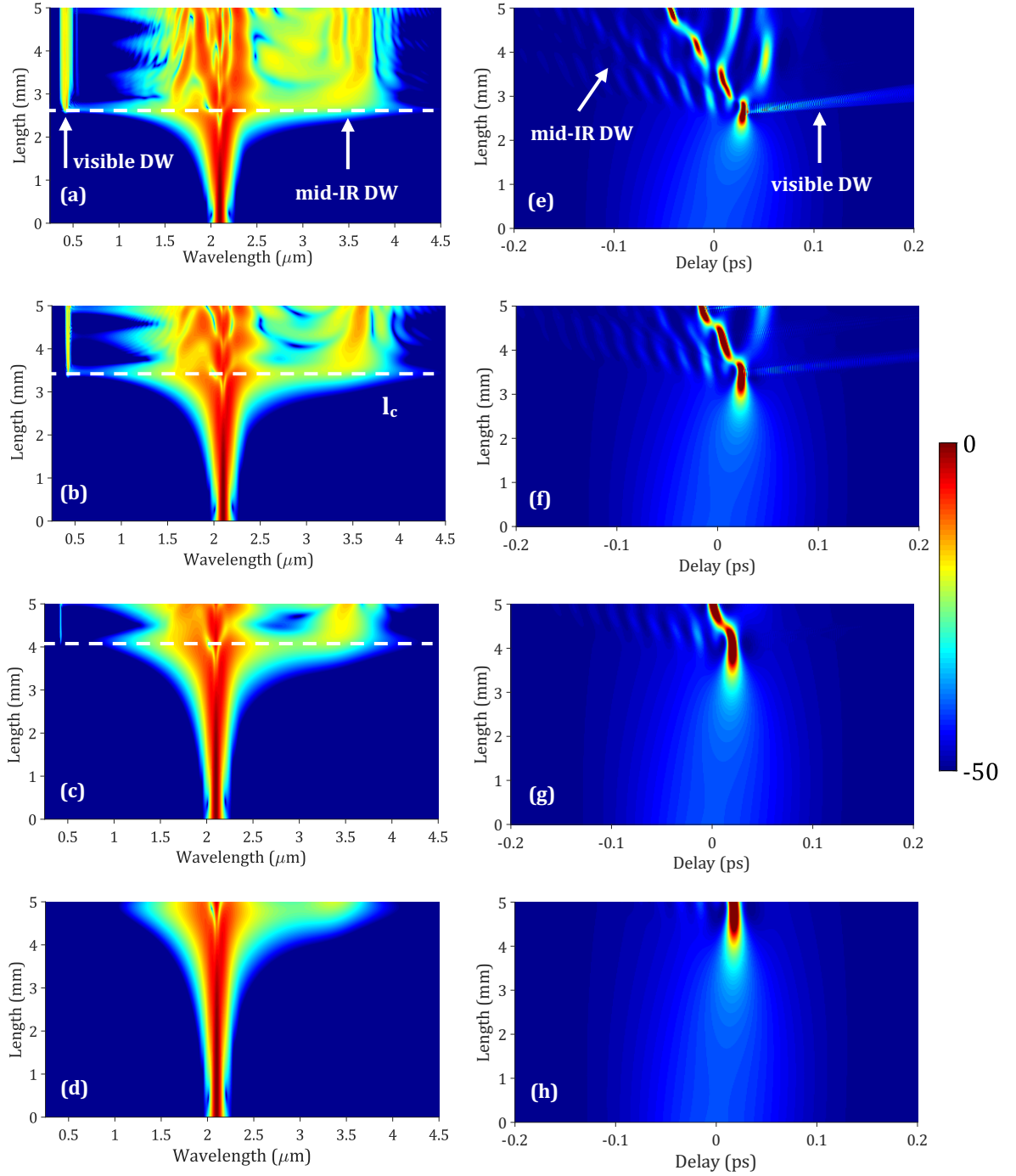
Figure 3.17 Numerically simulated spectral (a) - (d) and temporal (e) - (h) evolution for four different average coupled pump powers in a Si₃N₄ waveguide of 1.10 µm width. The dotted white line corresponds to the compression point l_c.

3.6 Conclusions

The development of a tunable mid-IR source based on DWG through an engineered SC process has been explored in detail. We showed that DWs located in the mid-IR could reach high levels of conversion efficiency. By merging dispersion-engineered large cross-section Si$_3$N$_4$ waveguides and a commercial turn-key femtosecond SWIR fiber laser, mid-IR CE can be boosted up to 35 %. State-of-the-art Si$_3$N$_4$ waveguides fabrication techniques allow for a careful waveguide design. Combining this design with a proper choice of pump parameters, the generation of mid-IR DW can be significantly favored. In contrast, the generation towards the visible part can be suppressed, reporting the highest efficiency measured to date for on-chip mid-IR DW generation.

The central wavelength of the dispersive waves can be set with lithographical precision inside the first mid-IR transparency window by simply changing the Si$_3$N$_4$ waveguide width. Precisely, the entire 3 – 4 µm wavelength region can be covered with milliwatt-level output powers. Numerical simulations of the different studied waveguide widths support the experimental findings, providing a deeper understanding of the DWG and soliton-fission process that arises under pumping in anomalous dispersion regime.

Thus, the presented approach can lead to a compact and easy-to-use device based on a chip-scale nonlinear platform compatible with planar fabrication techniques and a silica fiber-based pump source. Furthermore, the milliwatt-level power range achieved at the waveguide's output in the mid-IR spectral region is already suitable for spectroscopy applications, as we'll explore in the following thesis chapter.

Chapter 4

Gas spectroscopy using mid-IR supercontinuum from Si$_3$N$_4$ waveguides

Gas spectroscopy using mid-IR supercontinuum from Si₃N₄ waveguides

This chapter is based on the following journal publication and conference proceedings:

- D. Grassani, **E. Tagkoudi,** et al. "Mid-infrared gas spectroscopy using efficient fiber laser driven photonic chip-based supercontinuum," **Nature Communications**, vol. 10, no.1553, (2019) [145]
- **E. Tagkoudi** et al., "Gas Spectroscopy Using Low Threshold Mid-Infrared Radiation Generated in Si₃N₄ Waveguides," *Conference on Lasers and Electro-Optics (CLEO)*, San Jose, CA, U.S.A., paper STh1F.4. (2019) [151].
- **E. Tagkoudi** et al., "Multi-gas spectroscopy using tailored mid-IR dispersive wave generated in Si₃N₄ waveguide," *High-brightness Sources and Light-driven Interactions Congress*, paper MF1C.3. (2020) [152].
- **E. Tagkoudi**, et al. "Parallel gas spectroscopy using mid-infrared supercontinuum from a single Si₃N₄ waveguide," **Optics Letters**, vol. 45, issue 8, pp. 2195-2198, (2020) [153].

4.1 Introduction

Laser spectroscopy is a well-established and powerful technique for resolving molecular linewidths, as seen in the first chapter [31]. Particularly, middle-infrared (mid-IR) gas spectroscopy has attracted significant interest throughout the past decades due to the presence of extremely strong and unique absorption bands of trace gases in this part of the EM spectrum [33]. Gas monitoring in the mid-IR spectral region plays a critical role in many different fields, including molecular and biological sensing, food inspection, leak detection in industrial areas, environmental monitoring, and identification of hazardous gases for maintaining high air quality [4,154].

Focusing on the environmental monitoring of gas-phase species, the most vital application is detecting greenhouse gases, such as methane (CH_4) and carbon dioxide (CO_2). Controlling greenhouse gas concentrations emitted from vehicles and industrial sites can counteract the constant climate change [155]. Specifically, the C-H fundamental vibrational transition bands that lie in the spectral range between 3 - 4 μm need to be accurately resolved since they are present in many molecules closely related to environmental monitoring. For example, C-H roto-vibrational bands are essential for detecting methane, ethane, acetylene, and many hydrocarbons.

Methane (CH_4) and ethane (C_2H_6) are trace gases that significantly influence climate, and their quantification is very crucial for environmental monitoring [156].

On the other hand, acetylene (C_2H_2) is a well-known flammable gas that can be very hazardous to industrial production safety [157]. Moreover, all three gases contribute to the greenhouse effect. Therefore, it is essential to develop compact and simple-operation devices for simultaneous detection of CH_4, C_2H_6, and C_2H_2, whose absorption lines lie into the mid-IR.

Detecting mid-IR molecular signatures requires a significant field intensity which can be achieved through numerous different approaches. Quantum cascade lasers (QCLs) [67] and interband cascade lasers (ICLs) [69] have been currently the workhorse of laser sources for precise mid-IR molecular spectroscopy. An efficient alternative to these tools, which can provide extra tunability, as will be shown, is the generation of mid-IR light through nonlinear conversion. The direct generation of mid-IR light in the form of soliton-induced dispersive waves in Si_3N_4 waveguides pumped with an erbium-doped fiber laser at 1.55 μm has established a significant step towards compact mid-IR frequency comb sources [110]. However, limitations in conversion efficiency (CE) beyond 3 μm imply input average power levels of hundreds of milliwatts to reach the mW-level mid-IR power range required for spectroscopic application. In chapter 3 we showed that CE could be significantly enhanced by red-shifting the pump wavelength to the thulium band while maintaining the desired phase-matching conditions, reaching up to 35 % CE.

In this chapter, the tunable mid-IR DW-based source designed and developed in chapter 3 is tested in two separate absorption spectroscopy experiments. A first proof-of-principle absorption spectroscopy experiment confirms the value of this mid-IR source for the detection of acetylene (C_2H_2) using a DW at 3.00 μm. However, only a single gas can be detected from a given DW because of the limited DW spectral bandwidth. While the detection of several gas species could be achieved theoretically from different DWs, this would require switching between waveguides with varying dimensions or multiplexing the outputs of different waveguides. Nevertheless, by further system engineering, multiple trace-gas linear absorption spectroscopy can be achieved from light generated in a single Si_3N_4 waveguide. As a result, the large bandwidth of the generated DW with a center at 3.50 μm enables the parallel gas detection of acetylene (C_2H_2), methane (CH_4), and ethane (C_2H_6) simultaneously. Experimental results are compared with theoretical values extracted from the HITRAN database. Moreover, a study of the signal-to-noise ratio (SNR) as a function of different integration times proves a clear trade-off between the power of the on-chip generated mid-IR source and the required SNR and the number of averages.

Overall, this chapter shows that the toolkit for simultaneous trace-gas absorption spectroscopy has been extended beyond the commercially available and well-established mid-IR schemes. By leveraging on-chip mid-IR light generated in a single dispersion-engineered Si_3N_4 waveguide, a simple yet efficient device has been developed for parallel, or single, gas detection in the 3 – 4 μm spectral region.

4.2 Experimental Implementation

To demonstrate the application of the on-chip mid-IR source, we performed linear absorption spectroscopy experiments. The first one is a proof-of-principle spectroscopic experiment of gas acetylene (C_2H_2), using the DW centered at 3.00 μm generated from a 1.00 μm wide waveguide. The second experiment demonstrates parallel-gas detection of acetylene (C_2H_2), methane (CH_4), and ethane (C_2H_6) in a very short gas cell, using a DW at 3.50 μm from a 1.15 wide waveguide.

The experimental setup used for the spectroscopy experiments is shown in Fig. 4.1. The generation part is identical to the setup presented in chapter 3 (Fig. 3.7). The mid-IR DW, which serves as the light source for gas detection, is obtained from a dispersion engineered Si_3N_4 waveguide pumped with an off-the-shelf femtosecond fiber laser (Brevity λ+, NOVAE) which outputs 110 fs pulses at a 19 MHz repetition rate. At the output of the waveguide, light is directly coupled into a gas cell, which has a length of either 1 m or 5 cm for single-gas and multi-gas spectroscopy experiments, respectively.

After the interrogation of the gas sample using the DW-based source, the mid-IR light is collimated by adjusting the focal distance of the chalcogenide lens at the chip output. Afterward, the collimated light is focused using a parabolic mirror collimator into a single-mode indium fluoride (SMF InF_3) fiber to avoid Fabry-Perot effects. Finally, the spectra are recorded with an optical spectrum analyzer (OSA Yokogawa AQ6376) with a maximum wavelength reach of 3.4 μm. The total losses from the chip output to the OSA are estimated to be around 20 dB in this configuration. For all spectroscopic measurements presented in the chapter, the OSA is set to the maximum possible resolution –corresponding to 0.1 nm– and the high sensitivity setting using the internal chopper mode.
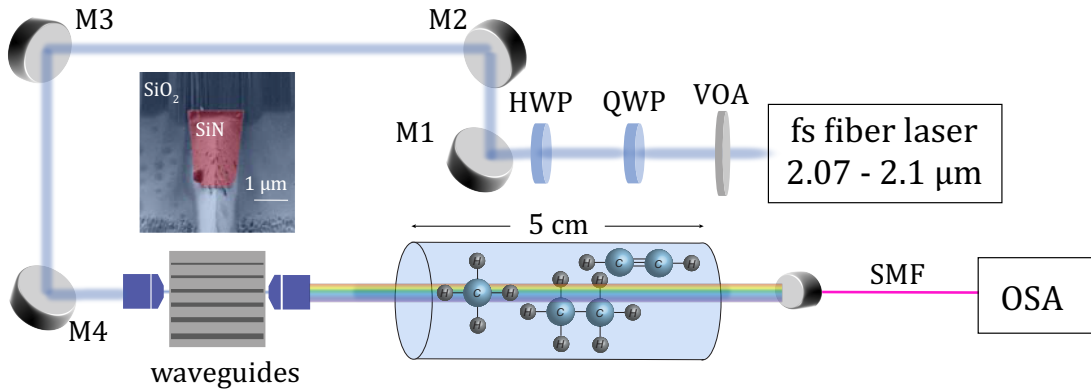
Figure 4.1 Experimental setup for gas absorption spectroscopy. M1-M4: mirrors that direct the laser beam into the chip, HWP: half-wave plate, QWP: quarter-wave plate, VOA: variable optical attenuator, SMF: single-mode fiber, OSA: optical spectrum analyzer. The scanning electron microscopic (SEM) picture of the large cross-section waveguide is also shown as an inset.

The overall tunability of the on-chip generated mid-IR source is once again presented in Fig. 4.2. The four different DWs are generated inside 5 mm long straight Si₃N₄ waveguides buried in a SiO₂ cladding with different cross-sections, as has been already discussed. Obviously, depending on the waveguide's cross-section, the DW can be generated between 3 and 4 µm. The spectra shown in Fig. 4.2 are obtained for approximately 13.6 mW average coupled power for all waveguides and are normalized to illustrate better the tuning capability and the overall possible coverage based on the multiplexing of the four DWs. This kind of mid-IR source offers flexibility in terms of spectral coverage since the DW position can be tuned by simply coupling into the adjacent waveguide on the same chip, depending on the targeting spectral region.

The input pump laser also offers some wavelength tunability: its central emitting wavelength can be adjusted between 2.07 and 2.10 µm. It is experimentally proved that a red-shift of the pump wavelength causes a blue-shift on the generated DW. As a result, the central wavelength of a given DW can be further fine-tuned by slight adjustments of the wavelength (λ_p) of the turn-key pump laser. This fine-tunability of the on-chip generated source through adjustment of the pump wavelength is also depicted in Fig. 4.2 for the 2.15 x 1.1 µm² waveguide (red curves).

Specifically, one edge of the DW can be favored by 5 to 10 dB with respect to the other. This is particularly important for the multi-gas absorption spectroscopy experiment presented in section 4.4. This is because the mid-IR DW has to spectrally overlap with the molecular absorption lines of many molecules simultaneously.
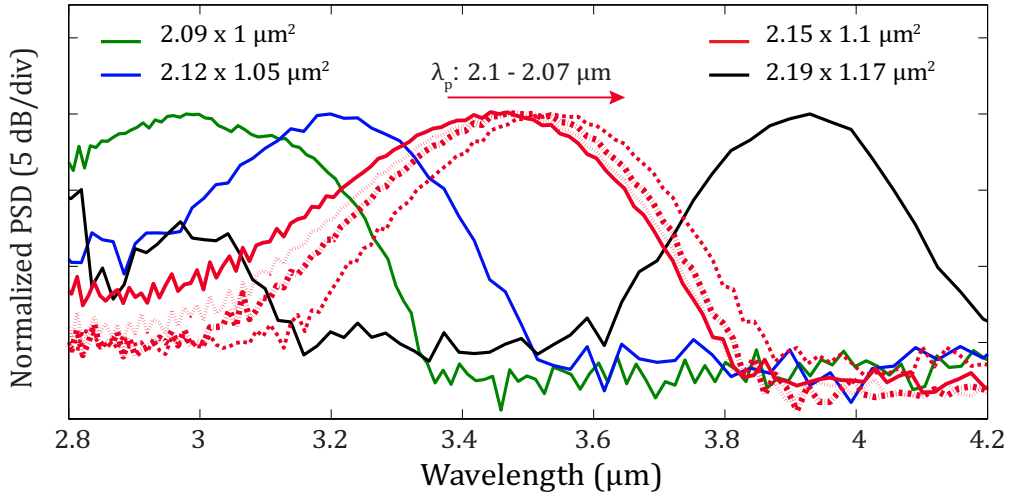
Fig. 4.2 Tunability of DWG based on waveguides with different cross-sections. Output spectra are recorded for a 13.6 mW average coupled power, and they are normalized for clarity. Fine tunability of the 3.50 µm DW is obtained through pump wavelength (λ_p) tuning, between 2.07 and 2.1 µm.

For the proof-of-concept single-gas spectroscopic experiment presented in section 4.3, the DW centered at 3.00 µm (green curve of Fig. 4.2) is utilized. In contrast, for the multi-gas spectroscopic experiment, the DW centered at 3.45 µm is used (solid red curve of Fig. 4.2).

4.3 Proof-of-principle spectroscopy measurement of C₂H₂

A simple proof-of-concept experiment is performed to demonstrate that the on-chip generated mid-IR DW can drive direct absorption spectroscopy. The targeted gas of this experiment is C_2H_2 because its molecular absorption lines reside precisely at the center of the 3.00 µm DW. The mid-IR light perfectly centered at 3.00 µm is generated from the 2.09 x 1.00 µm² Si₃N₄ waveguide and is directly coupled into a 108.5 cm long gas cell. The cell consists of wedged sapphire windows to avoid etalon effects and is filled with the gas sample under investigation. The light exiting the gas cell is guided to the Yokogawa OSA AQ6376. The transmitted spectra measured with the OSA with and without the gas sample are presented in Fig. 4.3. The sample spectrum is obtained by filling the long gas cell with 396 ppm C_2H_2 buffered in pure nitrogen (N_2). The total pressure in the cell is 1 atm at a temperature of $T = 296$ K. The reference measurement (without C_2H_2) is obtained by purging the cell with pure N_2. Absorption dips originating from C_2H_2 in the gas cell and atmospheric gas (H_2O) outside the cell are seen in Fig. 4.3. The resolution in the OSA is set to 0.1 nm with a sampling interval of 0.1 nm to obtain an optimum measurement. The high sensitivity setting is activated using the internal chopper mode.
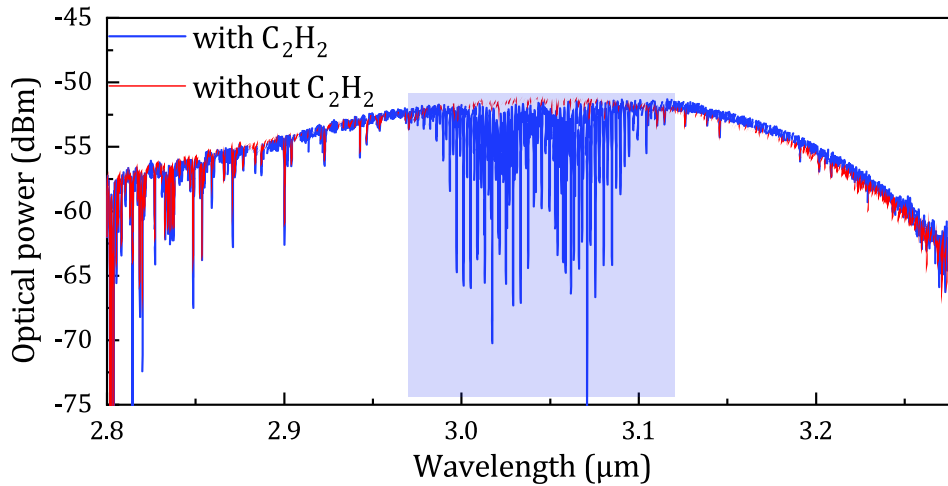
Fig. 4.3 Transmitted spectrum of the empty (red) or filled with C_2H_2 (blue) gas cell. The DW is centered at 3.05 µm, perfectly overlapping with the absorption lines of acetylene (highlighted with blue).

The spectrum through the gas cell containing the sample is first measured to extract the absorption spectrum presented in Fig. 4.4 (a). Afterward, the cell is purged and filled back to the original pressure with pure N_2. The reference measurement is the one containing the buffer gas. Therefore, the normalized spectral absorbance of C_2H_2 presented in Fig. 4.4 (a) is calculated by $-ln(I/Io)$, where I is the transmitted spectrum containing the gas, and Io is the reference spectrum. For these measurements, a sampling interval of 0.02 nm is used in the OSA, and a wavelength resolution of 0.1 nm using the high sensitivity setting of the internal chopper of the OSA, as previously. The measurement time for a wavelength range between 2.80 and 3.30 µm is approximately ~2 min.

After removing a remaining slowly varying background with a 9th order polynomial, the experimentally measured absorption spectra are fitted to a model based on the HITRAN database [3].
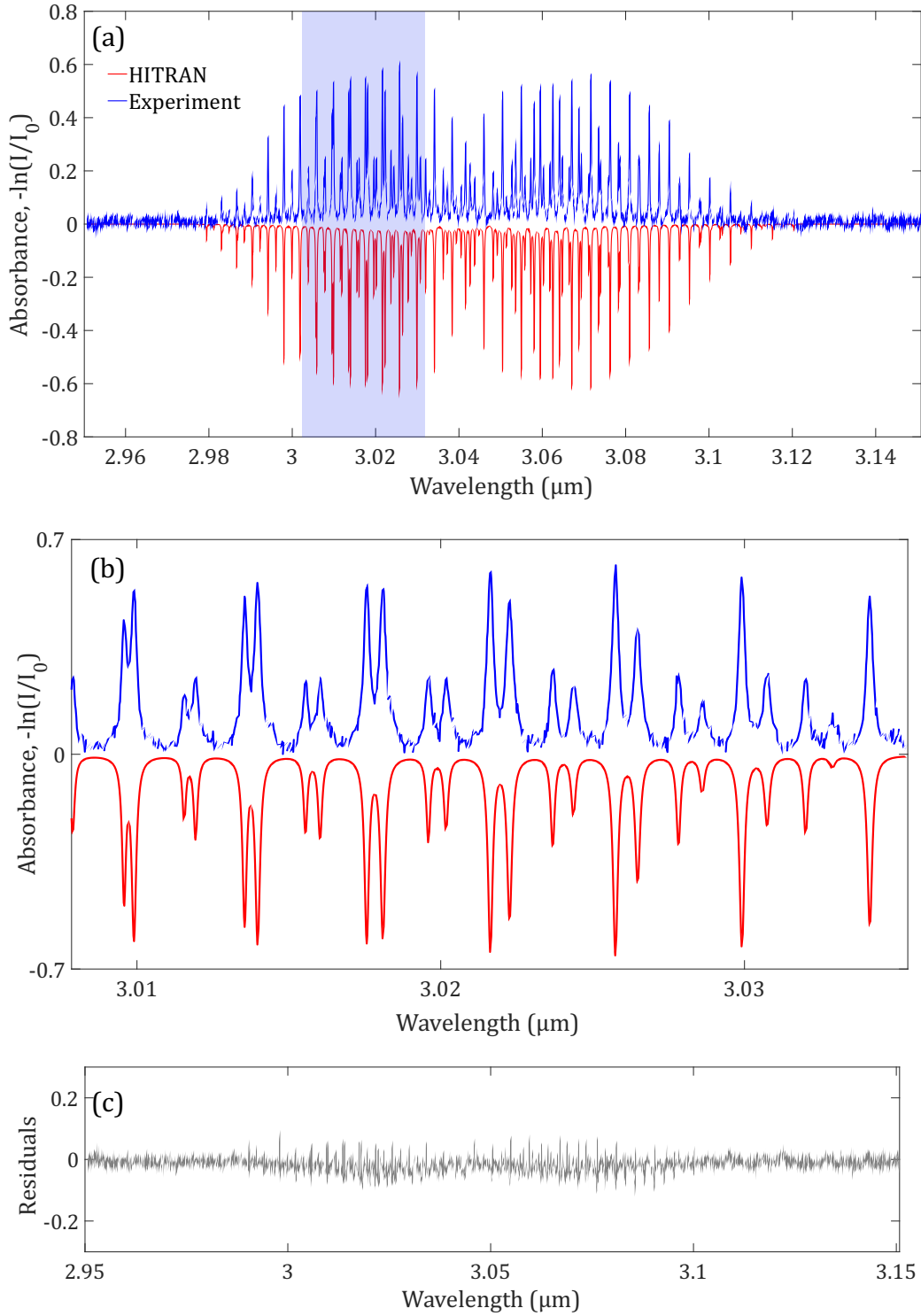
Fig. 4.4 (a) Absorption spectrum with the gas cell filled with C_2H_2 in N_2 buffer gas by normalizing the sample spectrum to that of the pure N_2 reference gas in the gas cell. The spectrum simulated using HITRAN is also shown in red (inverted for clarity). (b) Zoom-in graph, showing absorption lines between 3000 and 3035 nm (c) The residuals - the differences between simulations and experimental data - of the multiple-line fit.

67

The data provided by HITRAN include the spectral line intensity, central line frequency, air-broadening, and self-broadening coefficients, pressure shift coefficient, and the isotope peak line strength presented in chapter 2. Both Doppler and pressure line broadenings contribute in this case. As a result, a Voigt function is applied to simulate the line shapes of gas acetylene. The length of the cell, the temperature, as well as the gas partial and the total pressure, are taken into consideration for the simulations.

The difference between the normalized measurements and the HITRAN fitted data is plotted as the residual curve for C_2H_2, in which a least-square fitting is applied [158].

The normalized absorbance is compared to the HITRAN simulated one (red curve, inverted for clarity). The maximum normalized absorbance for χ=396 ppm of C_2H_2 is measured as 0.6. A zoom-in graph is shown in Fig. 4.4 (b) for easier comparison between measured and simulated absorption lines. The standard deviation (σ) of residual absorbance for this global fit is presented in Fig. 4.4 (c) and is measured to be $\sigma \sim$0.02.

Excellent agreement between the experimentally measured absorption lines and the corresponding simulated HITRAN lines confirms the reliability of the on-chip generated mid-IR DW source. The signal-to-noise ratio (SNR) is defined as the peak molecular normalized absorbance divided by the standard deviation (σ) of the noise in the baseline, which is given by the residuals (Fig. 4.4 (c)) [64,158]. SNR can be therefore calculated by the relationship SNR = a_{peak}/σ, where a_{peak} is the peak molecular absorbance presented in Fig. 4.4 (a). As a result, the SNR for the measurement is calculated to be ~30, and the noise equivalent concentration is ~13 ppm, given by 396 ppm/SNR$_{max}$. This value corresponds to the minimum detectable gas concentration using this device.

4.4 Parallel gas spectroscopy measurement of C_2H_2, CH_4, and C_2H_6 mixture

This section of the chapter discusses the results of parallel gas detection using a single Si₃N₄ waveguide. For the multi-gas spectroscopy experiment, we selected the waveguide with a cross-section of 2.15 x 1.10 µm². Using this waveguide, the generated DW perfectly centered at 3.45 µm offers the best overlap with CH_4 and C_2H_6 absorption lines. Additionally, the DW can be finely tuned, as seen in Fig. 4.2, by varying the pump wavelength in a specific waveguide to provide the optimized performance given the targeted gas (or gases). The pump is adjusted at 2.1 µm, to cover the absorption lines of C_2H_2 in parallel with the lines of CH_4 and C_2H_6. Nevertheless, as seen in Fig. 4.2, this DW does not efficiently cover the spectral region of C_2H_2 that we were able to detect with the DW at 3.00 µm from the smaller waveguide. In order to push the operation of the source, we further investigated the behavior of the SCG with increasing coupled pump power, enabled by a more optimized design.

The evolution of the spectra at the output of the chip for four different average coupled powers is presented in Fig. 4.5. For coupled pump powers of 16 mW and 17.7 mW, we observe a clear DW spectrum. The soliton number for these two powers is estimated as $N = 4$. When the power is further increased, at 21.2 mW, the broader spectrum is not as smooth as before and at the highest coupled power of 24.7 mW, the DW -reaching its maximum broadening- has a characteristic perturbed shape. The soliton number corresponding to the maximum coupled power is approximately $N = 5.2$.

It is observed that the total power in the mid-IR DW bandwidth, and CE, increase while increasing the pump power. Subsequently, the DW obtained with maximum coupled pump power (blue spectrum of Fig. 4.5) covers the entire spectral range from 2.86 μm to 3.86 μm. It has to be noted that the focal length of the output chalcogenide lens (Fig. 4.1) is adjusted to obtain an optimized maximum spectrum at 3.45 μm.

The broad bandwidth of the DW at 24.7 mW of coupled pump power provides sufficient coverage of the three targeted gases without switching to a waveguide with smaller dimensions, such as 2.09 x 1 μm^2 or 2.12 x 1.05 μm^2 (see Fig. 4.2). The region where the absorption lines of the gases reside are highlighted in grey. Absorption lines of C_2H_2 are located between 2.95 and 3.10 μm, while the spectral ranges 3.20 – 3.32 μm and 3.32 – 3.36 μm correspond to main absorption lines of CH_4 and C_2H_6, respectively.
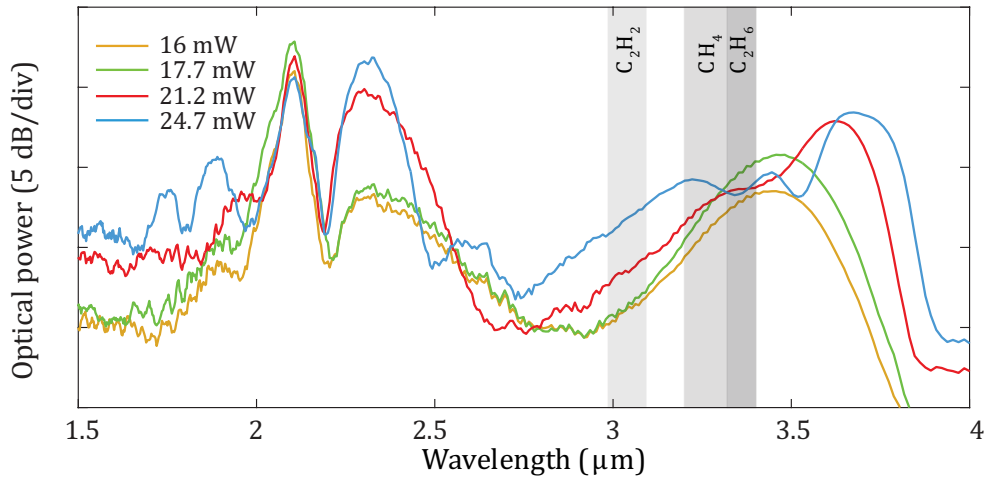
Fig. 4.5 Experimentally observed supercontinuum generation in a 2.15 × 1.10 μm^2 waveguide pumped at 2.1 μm with average coupled powers varying from 16 to 24.7 mW. The spectral region for spectroscopy is shown in grey: the C_2H_2 absorption lines are in the 2.95 – 3.1 μm range, the CH_4 main absorption lines lie in the 3.2 –3.32 μm range, and the C_2H_6 lines lie in the 3.32 – 3.36 μm range. Resolution: 0.1 nm (FT-OSA).

Numerical simulations based on the GNLSE are performed to explain the different shapes of the mid-IR DW for the maximum and the minimum coupled pump powers presented above. Fig. 4.6 presents the simulated spectral evolution for (a) a coupled pump power of 24.7 mW and (b) 16 mW for the waveguide of 2.15 x 1.1 μm^2 cross-section at the pump wavelength of 2.1 μm. We can notice that for lower pump power, the DW generated at 3.5 μm has a clear shape, like in the yellow curve of Fig. 4.5. However, for the maximum coupled power, the indication of multiple compression points before the end of the waveguide reinforces the emission of another DW. This reinforcement results not only in the broadening of the mid-IR DW but leads to interference between the generated DWs,

which is spectrally seen as a double-lobe shape of the mid-IR part of the spectrum (blue curve of Fig. 4.5).
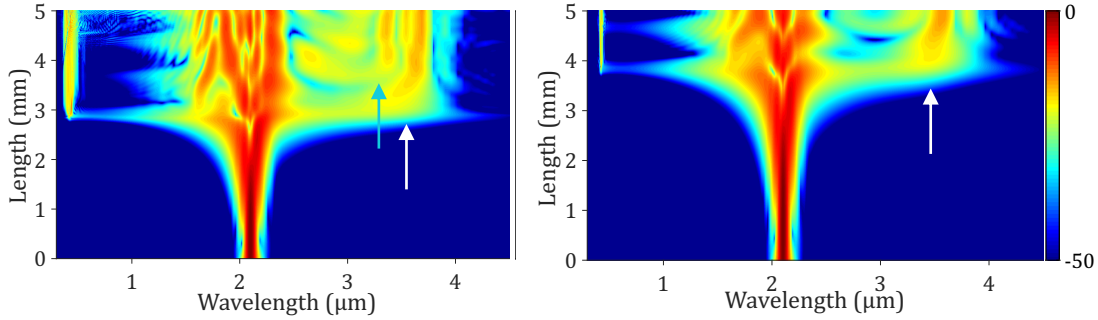
Fig. 4.6 Simulated pulse propagation evolution for the 2.15 x 1.1 µm^2 cross-section waveguide Si$_3$N$_4$ waveguide pumped at 2.1 µm for a propagation distance of 5 mm. The white arrows indicate the positions of the main generated mid-IR dispersive wave while the blue arrow indicates the secondary mid-IR peak, giving the characteristic shape to the DW. Numerical simulations are performed by solving the GNLSE for (a) 24.7 mW and (b) 16 mW coupled pump power.

The experimental values of the mid-IR on-chip generated source used for the multi-gas spectroscopy experiment are summarized in table 4.1 for all four coupled pump powers shown in Fig. 4.5. In addition, the calculations of the on-chip DW, output DW and corresponding CE values presented in Table 4.1 have been extensively discussed in chapter 3.

The maximum on-chip mid-IR power of the DW used in multi-gas spectroscopy is calculated as 8.4 mW, meaning 2.4 mW available at the chip's output. These values are slightly higher compared to values of Table 3.1 for the same waveguide geometry (2.15 x 1.10 µm^2). However, this can be justified by the red-shifting of the pump at 2.1 µm. The tunable SWIR laser used to pump the waveguides is a source based on Raman soliton-self-frequency shift. As a result, the power is increased when the source is shifted from the blue side towards longer wavelengths [159]. Thus, with more power to the source and while keeping the same coupling losses, the coupled pump power and the mid-IR DW power increase. Therefore, the maximum mid-IR power used to interrogate the multi-gas cell is estimated to be 2.4 mW, a value that is sufficient for spectroscopic measurements. The mid-IR DW bandwidth is also presented in Table 4.1, reaching 1000 nm for the maximum coupled power.

Coupled Pump power (mW)	On-chip DW power (mW)	Output DW power (mW)	On-chip CE (%)	DW bandwidth (nm) (at −10 dB)
16	3.8	1.07	23.75	750
17.7	4	1.13	22.6	750
21.2	6	1.7	28.4	820
24.7	8.4	2.4	34	1000

Table 4.1 Experimental values calculated for the 2.15 × 1.1 µm^2 waveguide. These values correspond to the four spectra presented in Fig. 4.5 for the 3.45 µm-centered DW used in the parallel-gas spectroscopy experiment.

Fig. 4.7 shows the experimental supercontinuum spectrum for the waveguide selected for the multi-gas spectroscopy compared with simulations for 24.7 mW of average coupled power.
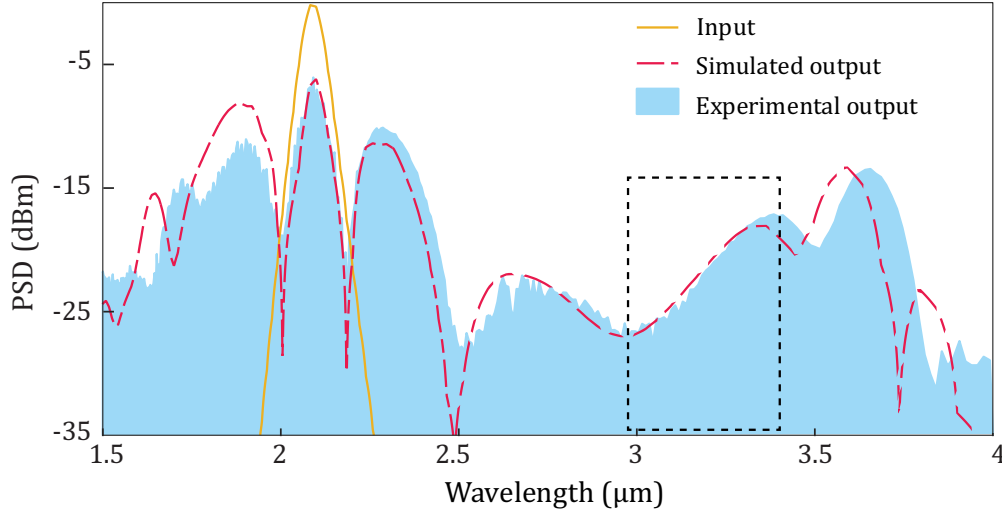
Fig. 4.7 Experimentally observed (blue) and simulated (red trace) supercontinuum generation in 2.19 x 1.1 μm^2 Si_3N_4 waveguide pumped at 2.10 μm (yellow trace) with 24.7 mW average coupled power. The spectral region used for spectroscopy showed in the black dashed box.

Experiments and simulations are found to be in excellent agreement. The dashed box illustrates the part of the mid-IR DW used for spectroscopy. Using a long-pass filter with a cut-on wavelength at 2.5 μm, the SWIR part of the SC is blocked.

The filtered mid-IR DW is then directly coupled into a short gas cell filled with the three targeted gases (C_2H_2, CH_4, and C_2H_6). The concentrations of the gas-phase mixture inside the gas cell are the following : 2.5 % of C_2H_2, 0.8 % of CH_4, and 1 % of C_2H_6 balanced with N_2 to a total pressure of 1 atm. The gas cell has a total path length of 5 cm with MgF_2 optics in the windows. The particular short gas cell is sealed, and there is no possibility to control or adjust the partial pressures of the three gases in the mixture. After interrogating the gas sample with the DW source, the collimated mid-IR light is focused using a parabolic mirror collimator into an SMF. Finally, the spectra are recorded with the same optical spectrum analyzer (OSA Yokogawa AQ6376).

Figure 4.8 shows the overall transmission spectrum collected after the gas cell. Simultaneous detection of C_2H_2, CH_4, and C_2H_6 is achieved in a single measurement within a spectral coverage of 2.95 - 3.4 μm. The noise level (grey curve) is also presented in the graph since the noise floor of the OSA rises significantly beyond 3.25 μm. Consequently, the maximum dynamic range of the gas absorption measurement is 15 dB and decreases close to the OSA's detection edge due to an increase in the noise floor.
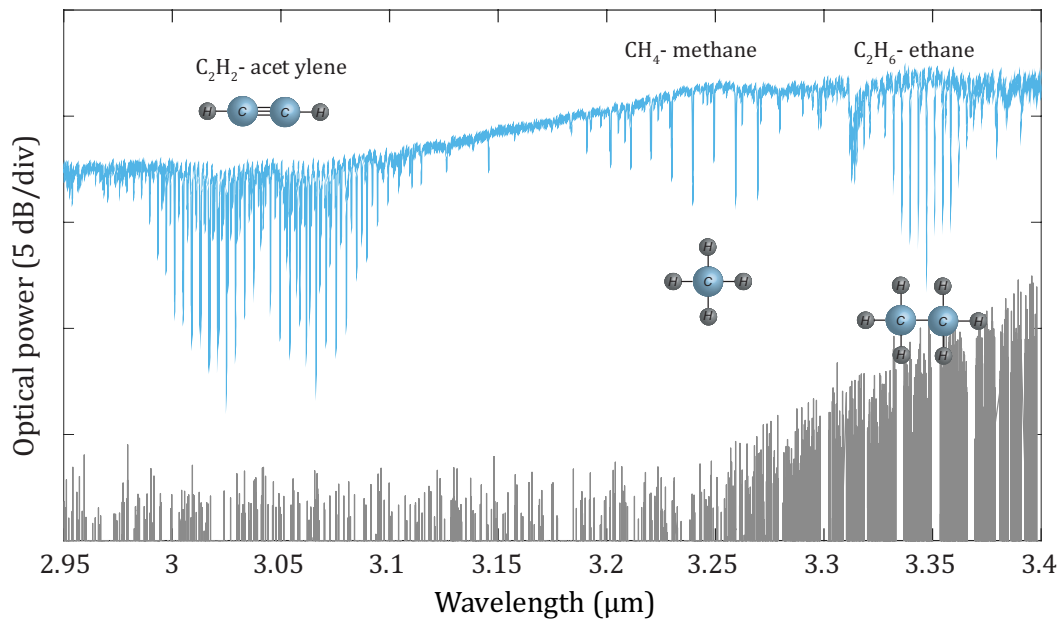
Fig. 4.8 Transmission spectrum at the output of the gas cell (cyan) observed on the OSA. The noise level is shown in grey. The resolution of the mid-IR OSA is set at the maximum of 0.1 nm.

The experimental results obtained for the multi-gas spectroscopy using the mid-IR DW source are presented, compared with HITRAN database simulations. To retrieve the normalized spectra, every measurement is obtained with the multi-gas cell, and afterward, the reference measurement without the gas cell is subtracted from the initial measurement.

The spectral absorbance is calculated by $-ln(I/Io)$, where I is the transmitted spectrum containing the gases, and Io is the reference spectrum. All spectra are recorded with a wavelength resolution of 0.1 nm using the high sensitivity setting of the internal chopper of the Yokogawa OSA AQ6376 and a sampling step of 0.02 nm. Data acquisition over the 2.95 – 3.4 µm spectral band was performed for 1, 2, 4, and 8 numbers of averages set on the OSA.

The analysis is already described in section 4.3 for single-gas detection. After removing a remaining slowly varying background with a 9th order polynomial, the experimentally measured absorption spectra are fitted to a model based on the HITRAN database [3]. A Voigt function is applied to simulate the line shapes of the three gases separately. The length of the cell, the temperature, as well as the partial and the total pressure of each gas inside the mixture, are taken into consideration for the simulations. The difference between the normalized measurements and the HITRAN fitted data is plotted as the residual curve for each gas, where a least-square fitting is applied [158].

In Fig. 4.9 (a), the experimental spectrum of absorbance and the comparison with the HITRAN simulations (inverted for clarity) are presented for C_2H_2. The spectra in the following figures (Fig. 4.9 – 4.11) are obtained with eight times of averaging in the OSA.

The wavelength range between 2.98 and 3.09 µm has been converted to a wavenumber range of 3230 – 3360 cm^{-1}. The correspondence between the experimental data and the HITRAN database is more evident in the zoom-in graph shown in Fig. 4.9 (b) with the equivalent residual plotted in black below (c). The standard deviation of the residual for acetylene C$_2$H$_2$ using the spectral range shown in Fig. 4.9 (b) is calculated to be σ = 0.045.
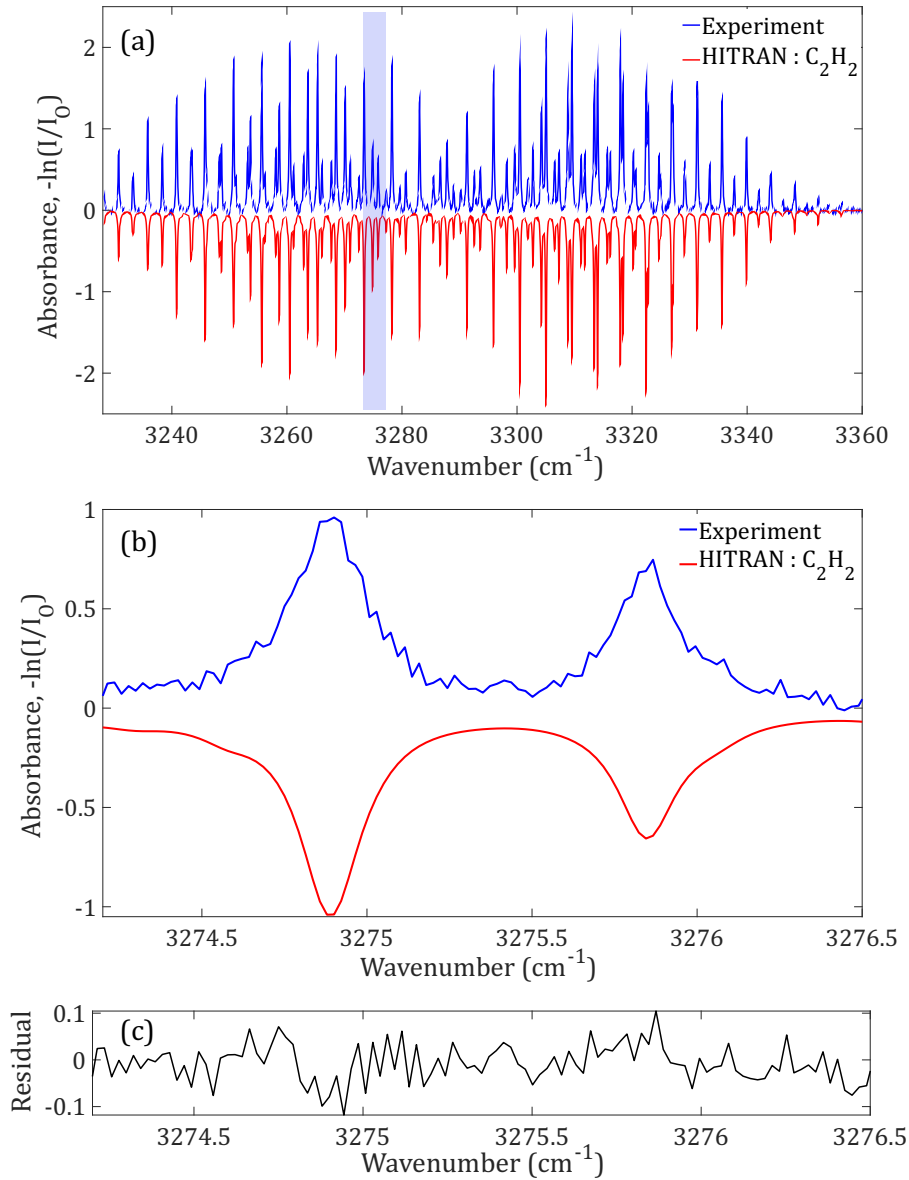
Fig. 4.9 (a) Experimental gas absorbance (blue curve) and the HITRAN database (red curve, inverted) for gas acetylene C$_2$H$_2$. The light blue shaded area represents the selected zoom-in graphs shown in (b) together with the (c) residual (black line).

In Fig. 4.10 (a), the experimental spectrum of absorbance and the comparison with the HITRAN simulations (inverted for clarity) are presented for CH$_4$.

The wavelength range between 3.18 and 3.32 μm corresponds to a wavenumber range of 3011 – 3179 cm^{-1}. The correspondence between the experimental data and the HITRAN database is pronounced in the zoom-in graph shown in Fig. 4.10 (b) with the equivalent residual plotted in black below (c). The standard deviation of the residual for methane CH_4 using the spectral range shown in Fig. 4.9 (b) is calculated to be σ = 0.038.
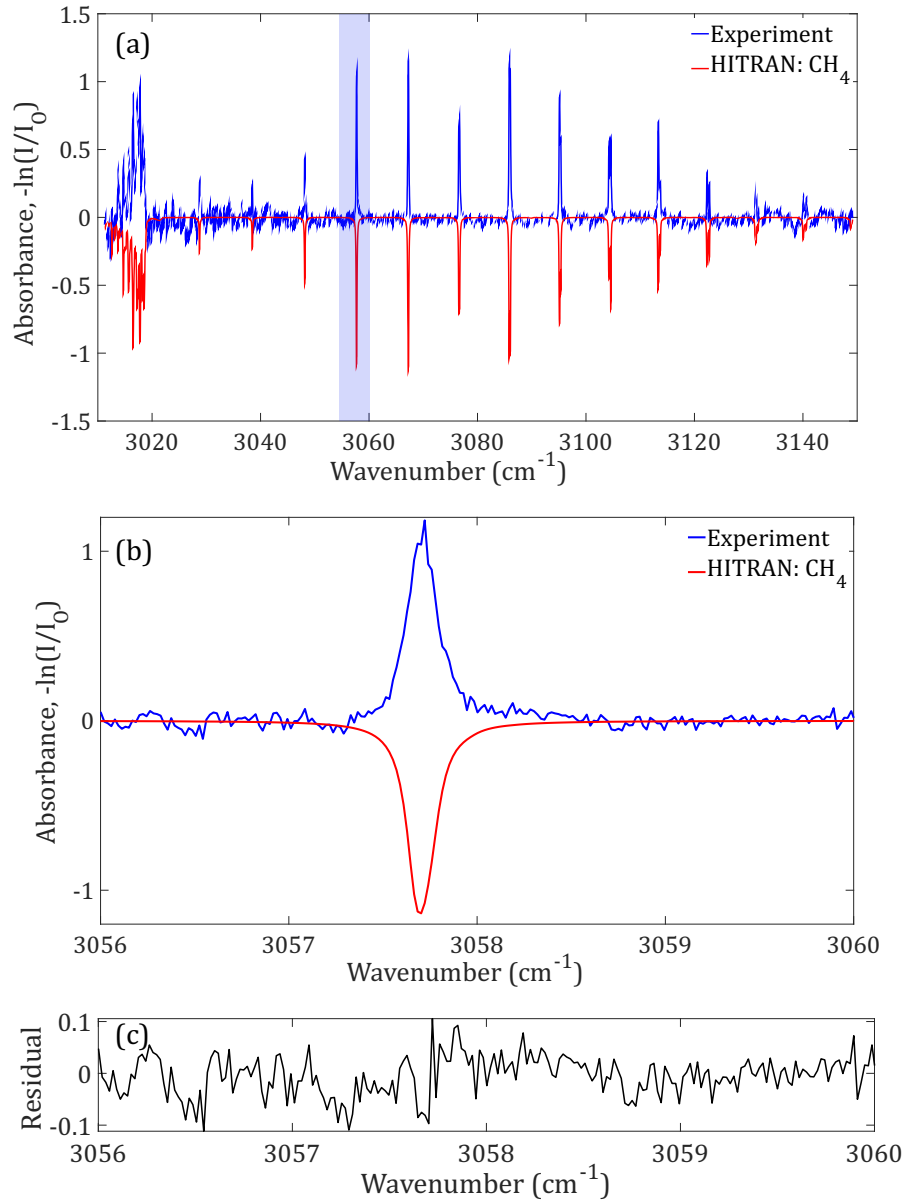
Fig. 4.10 (a) Experimental gas absorbance (blue curve) and the HITRAN database (red curve, inverted) for gas methane CH_4. The light blue shaded area represents the selected zoom-in graphs shown in (b) together with the (c) residual (black line).

Finally, in Fig. 4.11 (a), the experimental spectrum and the comparison with the HITRAN simulations (inverted for clarity) are presented for C_2H_6. The wavelength range between 3.33 and 3.36 μm can be expressed as a wavenumber range of 2972 – 3001 cm^{-1}. The correspondence between the experimental data and the HITRAN database is shown clearly in the zoom-in graph of Fig. 4.11 (b), with the equivalent residual plotted in black

below (c). The standard deviation of the residual for ethane C_2H_6 using the spectral range shown in Fig. 4.10 (b) is calculated to be $\sigma = 0.11$.

As indicated by the yellow arrows, absorption lines from CH_4 can be seen in Fig. 4.10 (a), despite being much weaker than the C_2H_6 lines. The presence of methane's lines shows that the two gases can be detected within the same spectral span. However, they can be distinguished by each other.
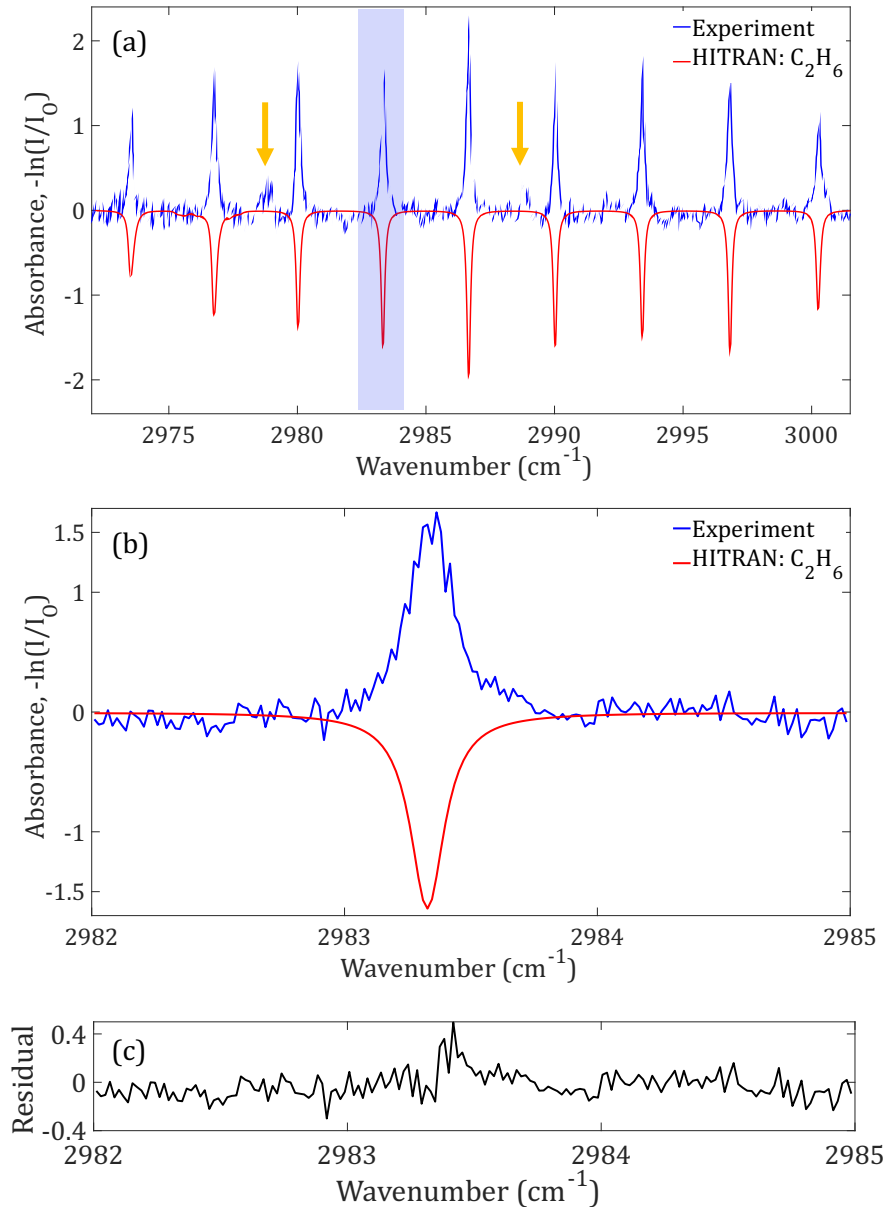
Fig. 4.11 (a) Experimental gas absorbance (blue curve) and the HITRAN database (red curve, inverted) for gas ethane C_2H_6. The light blue shaded area represents the selected zoom-in graphs shown in (b) together with the (c) residual (black line). In (a), the black arrows indicate two of the CH_4 absorption lines, also confirmed by HITRAN simulations.

Comparing the estimated standard deviation values for the three gases, the smallest σ value is obtained for CH_4. This can be explained by the higher power spectral density of the mid-IR DW in the vicinity of the CH_4 absorption lines combined with a relatively low

noise floor from the OSA. On the other hand, the largest standard deviation for C_2H_6 mainly comes from the increased noise level of the OSA at this wavelength range.

Overall, the above analysis shows an excellent agreement between the HITRAN model and the experimental results for all three detected gases.

4.5 Signal-to-noise ratio (SNR) study

A strong point of the mid-IR source as a spectroscopic tool arises from the combination of the dispersion-engineered Si_3N_4 waveguide and the tuning of the pumping wavelength in such a way that the mid-IR DW will be efficiently generated and optimized. In the following set of experiments we investigate and discuss the impact of the efficiency of the generated source on the detection performance.

The signal-to-noise ratio (SNR) can be directly extracted from the standard deviation (σ) of the baseline noise (residuals) [158]. SNR is calculated by the relationship:

$$SNR = \frac{a_{peak}}{\sigma}$$

where a_{peak} is the peak molecular absorbance presented in Fig. 4.9 (a) – 4.11 (a) for each gas, respectively [160]. This form of SNR calculation comes from the fact that the source used in the measurement presents a large spectral bandwidth [161].

The SNR for all three gases for the four different mid-IR DW powers is measured by adjusting the coupled pump power as specified in Table 4.1 and different numbers of averages. The calculated SNRs as a function of the number of averages are presented in Fig. 4.12 (a) - (c). According to the multi-absorption line analysis presented in [161], five absorption peaks from different areas of the spectrum are selected for each of the three gases to extract the SNR. The points of Fig. 4.12 represent the mean value of the calculated SNRs, and error bars have been added based on the extracted standard deviation.

The SNR follows a square-root dependence on the number of averages since the system noise is dominated by white noise. A mismatch between the square-root fittings and the measured SNRs is attributed to drifts in the DW power in each spectral region during the averaging time. As expected, the SNR increases with the number of averages, and the best SNRs for all three gases are obtained for the highest mid-IR DW power.

The graphs also illustrate the importance of having an efficient and, at the same time, broad mid-IR generation. For example, in Fig. 4.12 (c), which is the SNR for C_2H_6 within the spectral region at the limit of our OSA wavelength range, the gas detection is impossible unless a minimum of 1.2 mW of DW is generated. This is due to the much higher noise level of the OSA, which masks the C_2H_6 absorption lines at lower powers.

For the case of CH_4 presented in Fig. 4.12 (b), with absorption lines perfectly centered with the DW peak, increasing the total mid-IR DW power up to 1.7 mW significantly improves the performance. As a result, this enables much faster measurements.
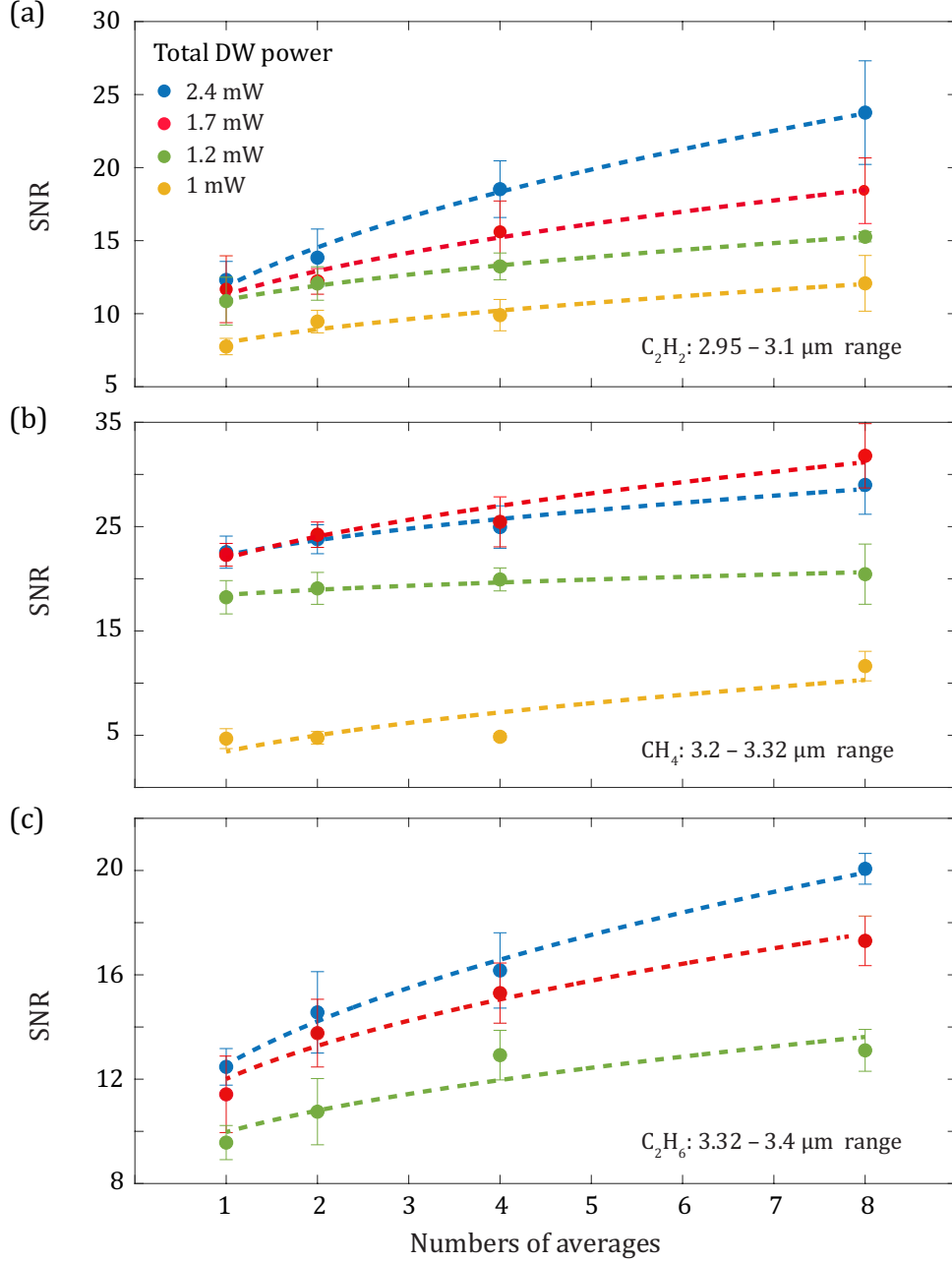
Fig. 4.12 SNR retrieved from the residuals for four mid-IR DW powers (2.4, 1.7, 1.2, and 1 mW) as a function of the number of averages for (a) C_2H_2, (b) CH_4, and (c) C_2H_6. A square root fitting is applied, showing SNR dependence on the number of averages.

A further increase of power does not seem to provide an additional advantage within this wavelength range. This is explained by the fact that when the coupled pump power is increased towards the maximum value of 24.7 mW, the main consequence is the spectral broadening of the DW, as seen in Fig. 4.5 and quantified in Table 4.1.

While the total DW increases, the actual power within the CH_4 spectral band does not change significantly. However, more and more light is generated on the blue and red side of the DW, allowing for the detection of multiple gases in an extended wavelength range.

Finally, in Fig. 4.12 (a), an excellent fit in the case of C_2H_2 is observed, following the trade-off between DW overlap and equipment noise.

The mole fractions of C_2H_2, CH_4, and C_2H_6 can also be extracted from the absorbance spectra fittings. The fittings estimate the partial pressure in the cell for each gas separately. The mole fraction can be calculated by dividing the partial pressure for each gas with the total pressure in the gas mixture. As a result, χ_{C2H2} =19760 ppm is calculated for C_2H_2, χ_{CH4} = 5513 ppm for CH_4, and χ_{C2H6} = 9149 ppm for C_2H_6. The maximum estimated SNR for all the gases is equal to 24 for C_2H_2, 34.5 for CH_4, and 21 for C_2H_6. The noise-equivalent detection limits for the three gases, defined as χ/SNR_{max}, are estimated as 824 ppm for C_2H_2, 160 ppm for CH_4, and 436 ppm C_2H_6.

Consequently, the sensitivity limit for a particular spectroscopic measurement is set by the maximum obtained SNR. The gas cell used for this spectroscopy experiment is extremely short, and, as a result, these are the best detection limits we could achieve in such a length. On the other hand, a higher performance of the device -a lower detection limit for the three gases- can be achieved using longer cells.

Table 4.2 summarizes the essential values obtained using the 3.45 μm DW for the simultaneous detection of C_2H_2, CH_4, and C_2H_6.

Gas	Spectral range (μm)	Standard deviation (σ)	SNR	detection limit (ppm)
C_2H_2	2.95 – 3.1	0.045	24	825
CH_4	3.2 – 3.32	0.038	34.5	160
C_2H_6	3.32 – 3.4	0.11	21	436

Table 4.2 Summary of the extracted standard deviation (σ), the maximum obtained SNR, and the detection limit in ppm for the three investigated gases: C_2H_2, CH_4, and C_2H_6.

4.6 Conclusions

In summary, in this chapter the application of the mid-IR DW-based source for gas spectroscopy has been demonstrated. To confirm that DWs generated on single Si_3N_4 waveguides have the potential to serve as sources for direct absorption spectroscopy, experiments of single-gas and parallel-gas detection have been performed.

In a first demonstration, a mid-IR DW centered at 3.00 μm can detect gas acetylene (C_2H_2) with a 13 parts-per-million (ppm) noise-equivalent detection limit in a very long gas cell of 1 m with adjustable pressure. This DW is generated in a Si_3N_4 waveguide with a cross-section of 2.09 x 1.00 $μm^2$ pumped at a wavelength of 2.09 μm.

For further optimization, the tunability of the pump wavelength is used to fine-tune the mid-IR DW position. Apart from that, fine-tuning results in an enhanced CE and a broader bandwidth of the DW. Thus, the DW can be centered at a specific wavelength to overlap with the targeted molecular absorption lines. With a pump located at 2.1 μm and a waveguide of 2.15 x 1.10 $μm^2$ dimensions, a broad DW centered at 3.45 μm is generated. The simultaneous detection of multiple gas-phase species within the 2900 – 3380 cm^{-1} functional group region using this broadband mid-IR DW is demonstrated. Quantitative detection of acetylene (C_2H_2), methane (CH_4), and ethane (C_2H_6) has been achieved with several hundreds of ppm noise-equivalent detection limit in a 5 cm long gas cell with fixed pressures. Precisely, the detection limits are calculated as 824 ppm for C_2H_2, 160 ppm for CH_4, and 436 ppm for C_2H_6. Experimental results are compared with theoretical values of the HITRAN database, and a detailed study of the signal-to-noise (SNR) ratio performed for different integration times showing the clear trade-off between the power of the source and the required number of averages in the OSA, thus the SNR.

Overall, a compact, single-pass, multiple gas-phase species absorption spectroscopy device has been experimentally demonstrated. The mid-IR DW is generated through the SC process in dispersion-engineered large cross-section Si_3N_4 waveguides, which are seeded with wavelength-tuned fiber laser pulses, enabling extra tunability of the source. The reliability of the developed device is confirmed by an excellent agreement between measured absorption lines and HITRAN simulations.

Chapter 5

Polarization-dependent supercontinuum in uncladded Si_3N_4 waveguide

Polarization-dependent supercontinuum in uncladded Si₃N₄ waveguide

The content of this chapter is based on the following publications:

- **E. Tagkoudi** et al., "Extreme polarization-dependent infrared supercontinuum generation in uncladded silicon nitride waveguide," CLEO-Europe, (2021)
- **E.Tagkoudi** et al., "Extreme polarization-dependent supercontinuum generation in an uncladded silicon nitride waveguide," **Optics Express**, vol. 29, issue 14, pp. 21348-21357, (2021) [162]

5.1 Introduction

The nonlinear dynamics of a supercontinuum (SC) source depend dramatically on the dispersion profile of the hosting material, as already seen in previous chapters of this thesis. The majority of studies on on-chip supercontinuum generation (SCG) focus on the anomalous dispersion pumping regime using ultrashort pulses [105,108,109]. The spectral broadening arises from soliton dynamics in this regime, including fission of the seed pulse into multiple solitons. As a result, the energy of the solitonic pulse can be transferred to the phase-matched dispersive waves (DW), as extensively studied in chapter 3. While these underlying dynamics are known to yield SC with an extensive spectral bandwidth, they lead to spectra with multiple fine spectral structures that are susceptible to noise [87].

The noise sensitivity and fine spectral features can be significantly minimized in platforms exhibiting an all-normal dispersion (ANDi) profile. ANDi SCG typically displays reduced bandwidth compared to the anomalous pumping schemes and requires higher pump powers. However, ANDi SCG dynamics are dominated by self-phase modulation (SPM) and optical wave breaking (OWB), processes considerably less prone to noise amplification. As a result, the obtained SC from an ANDi profile has an improved phase-stability and coherence, leading to a smooth profile [163,164]. These characteristics of ANDi SCG make it an ideal SC source for pulse compression applications, as reported in [165,166].

While ANDi SCG has attracted significant attention during the years in fiber-based platforms [166,167], there have been very few demonstrations of on-chip ANDi SC. Until today, active research on ANDi in integrated platforms is mainly based on silicon-germanium waveguides (SiGe/Si), exploiting its strong material dispersion [103,104].

Recently, ANDi SCG in a silicon-rich silicon nitride platform has been reported, exhibiting a low normal GVD for the TE mode [168]. While the bandwidth of the ANDi SC using telecom wavelength pumping spans nearly one octave, the generated SC source exhibits pronounced spectral features with intensity variations up to 30 dB across the entire SC spectrum [168]. The reasons for such strong spectral features, uncommon to ANDi SC, are unclear but could be attributed to the input pulse profile and the low dispersion value at the pump wavelength.

In an effort to exploit ANDi SC in a nonlinear platform such as stoichiometric silicon nitride, Si_3N_4, a different waveguide design is experimentally and numerically studied in this chapter of the thesis. Using a fully uncladded Si_3N_4 waveguide, an extremely polarization-sensitive SWIR supercontinuum (SC) source is generated due to the very different dispersion profiles depending on the propagation mode.

The air-clad design of this waveguide is engineered to present simultaneously anomalous dispersion regime for transverse electric (TE) mode excitation and all-normal-dispersion (ANDi) for the transverse magnetic (TM) mode at a near-infrared pumping wavelength range between 1.73 - 2.13 µm. This dispersion-engineering of the polarization modes enables switching via simple adjustment of the input polarization state, from an octave-spanning soliton fission-driven supercontinuum with a fine spectral structure to a flat and smooth ANDi SC at a pumping wavelength of 2.10 µm. Such polarization-sensitive SC source could be utilized in versatile applications from broadband on-chip sensing to pulse compression and few-cycle pulse. Moreover, the experimental results are in excellent agreement with numerical simulations.

5.2 Waveguide design and experimental implementation

The waveguide is fabricated using the photonic Damascene process based on LPCVD of Si_3N_4 on top of SiO_2 [150]. This technique efficiently releases the tensile stress and prevents cracking of the Si_3N_4 thin film, allowing for the fabrication of large cross-section waveguides, like those detailed studied in chapter 3. However, the standard design for buried Si_3N_4 waveguides is slightly modified for the uncladded structure. The Si_3N_4 core layer is left uncovered, providing a full air-cladded scheme that is envisioned to be used in on-chip sensing applications.

A scanning electron microscope (SEM) picture of the fabricated structure and corresponding dimensions are shown in the inset of Fig.5.1. The waveguide is 5.5 cm long, folded in 11 meanders on a 5mm x 5mm chip, and has a cross-section of 2.00 µm x 0.75 µm. The bends have a radius of approximately 100 µm, designed to minimize mode mixing. The group velocity dispersion (GVD) profile is numerically simulated for both TM and TE modes using the FEM mode solver COMSOL Multiphysics and is presented in Fig.5.1. The dispersion is essentially low and anomalous for the TE polarization mode between the 1.00 - 2.13 µm region with two zero-dispersion wavelengths (ZDWs) at 1 and 2.13 µm. The dispersion of the TM mode is also anomalous in the near-infrared with ZDWs at 840 nm and 1.73 µm. However, it becomes normal beyond 1.73 µm.

Two possible pumping wavelengths based on the available fs fiber lasers are indicated in Fig. 5.1: 1.56 μm and near 2 μm. With a standard NIR wavelength of 1.56 μm, we expect to see the generation of an anomalous SC regardless of the pump polarization. However, pumping at 2 μm allows for ANDi SC from the TM polarization mode while for TE mode remains anomalous.
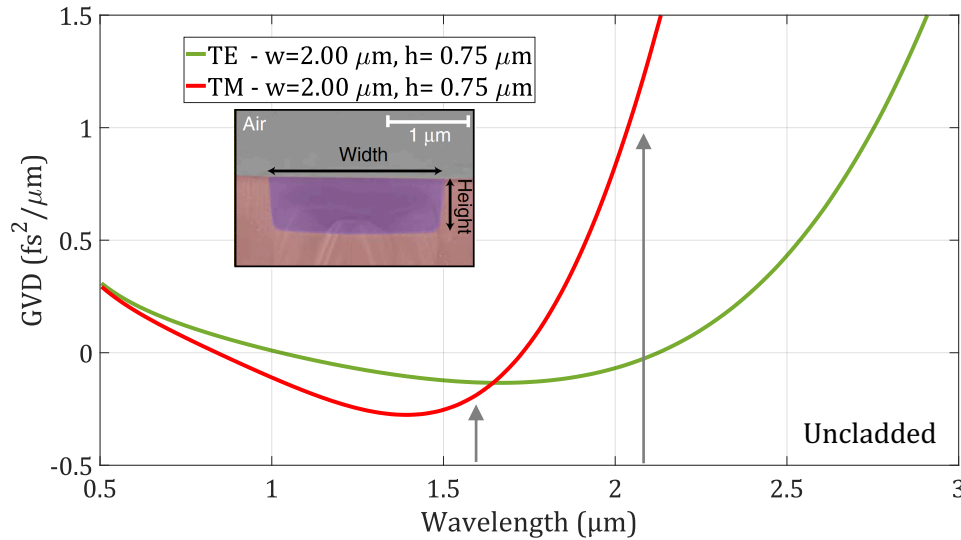
Fig. 5.1 Simulated group velocity dispersion (GVD) curve for the fundamental TM (red curve) and fundamental TE mode (green curve). The arrows indicate the position of the pumps. Inset: SEM image of the uncladded Si₃N₄ waveguide of 2.00 μm x 0.75 μm cross-section.

Numerical simulations of the GVD curves are also performed for both TM and TE modes, considering the SiO₂-cladded version of the same waveguide geometry.
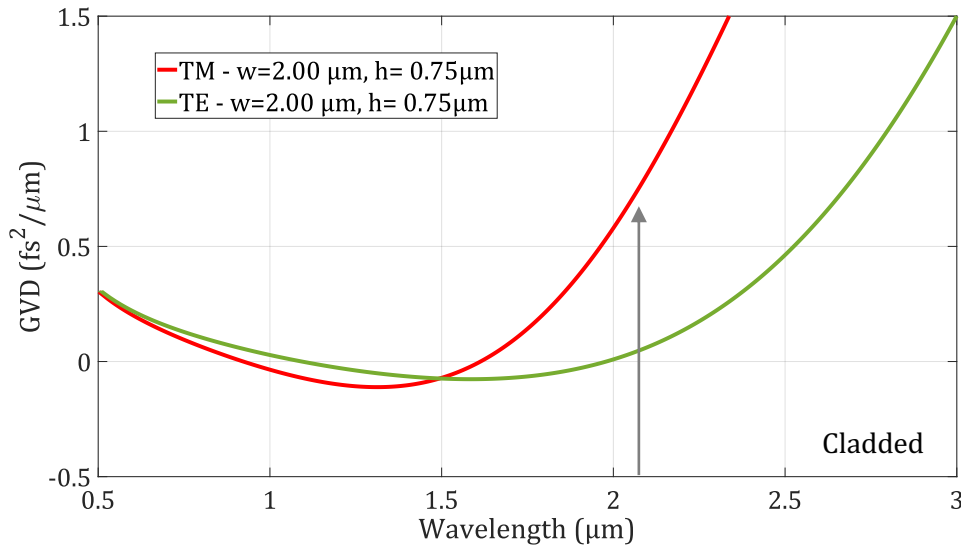
Fig. 5.2 Simulated group velocity dispersion (GVD) curve for the fundamental TM (red curve) and fundamental TE mode (green curve) for a SiO₂-cladded Si₃N₄ waveguide of 2.00 μm x 0.75 μm cross-section. The arrows indicate the position of the pump.

However, as we can see in Fig. 5.2, pumping the cladded design at 2.10 μm does not offer the advantage of switching between different dispersion regimes since it is normal for both TE and TM modes at a pumping wavelength of 2.10 μm, while it remains anomalous

for a pump centered at 1.56 μm. As a result, the cladded version does not provide as much differentiation between TE and TM, showing the clear advantage of the uncladded design used in the experiments.

Fig. 5.3 presents the integrated dispersion β_{int} curves as a function of wavelength for the air-cladded waveguide cross-section. The β_{int} for the two possible pumping wavelengths, 1.55 μm (purple curve) and 2.10 μm (green) for the TE mode are plotted.

From Fig. 5.3, we see that for a pump positioned at 1.55 μm, energy is symmetrically transferred to the phase-matching locations, one in the visible and the second one located in the mid-IR, before 3.5 μm. However, similar to what we have seen in the previous fully cladded waveguides, we can expect a relatively low conversion efficiency towards the mid-IR since the distant location of the DW from the telecom-wavelength pump constitutes a significant barrier for the pump powers that we can couple to the waveguide.
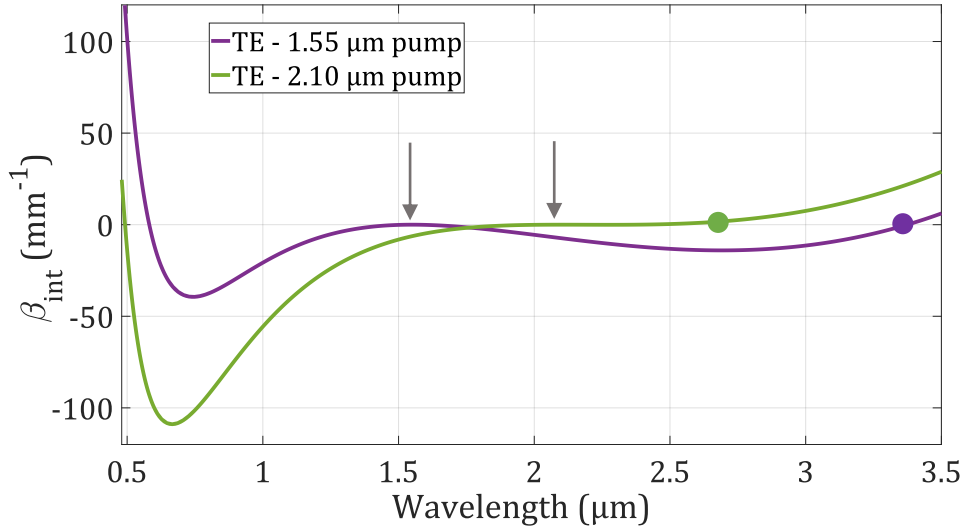
Fig. 5.3 Simulated integrated dispersion as a function of wavelength for the uncladded waveguide scheme of 2.00 x 0.87 μm², cross-section, pumped at 1.55 μm (purple), and at 2.10 μm (green). Both curves are simulated for the TE polarization mode. The arrows indicate the positions of the pump.

On the other hand, by red-shifting the pump at 2.10 μm, we observe the same symmetry breaking of the integrated dispersion once again predicting a favored and more efficient energy transfer to the mid-IR, but with a shorter wavelength reach compared to 1.55 μm pumping. Thus, the pump selection for this study is based on the dual TE/TM SC behavior that a pump located at 2.10 μm offers for the uncladded waveguide design while at the same time trying to reach as efficiently as possible mid-IR wavelengths beyond 2.5 μm.

The experimental setup for the generation and characterization of SCG in the uncladded waveguide is the same as presented in Fig. 3.7 of chapter 3. The polarization of the pump pulses is controlled by a HWP, allowing for exciting the TE or the TM mode selectively. The collimated light is focused with a parabolic mirror at the waveguide output with a fluoride MMF connected to an OSA. Depending on the wavelength range, the spectra are recorded using different OSAs for the visible/near-infrared range from 350 nm to 1750 nm (Yokogawa AQ6374) and the mid-infrared range 1500-3400 nm (Yokogawa AQ6376).

The total transmission losses including in/out-coupling, propagation losses, and Fresnel reflection from the waveguide facets, are measured at the pump wavelength with low power in the absence of spectral broadening. They are estimated to be around 13 and 22 dB for TE and TM polarization, respectively. The difference in coupling might be possibly attributed to the in/output tapers operating differently in TE and TM polarization modes. Optical propagation losses for both TM and TE modes are also evaluated using the propagation loss coefficient α as shown in Fig. 5.4. They are calculated by including the imaginary part of the refractive index of SiO_2 in the numerical simulations. Fig. 5.4 shows that the mode is very well confined in the core of the waveguide for wavelengths below 3.5 µm, and the losses are around 0.5 dB/mm and 0.2 dB/mm for TM and TE mode at this wavelength, respectively. At the pump wavelength of 2.10 µm propagation losses are estimated as 0.05 dB/mm for both TM and TE modes. Simulations of losses are performed considering a straight waveguide geometry in the COMSOL model. As a result, propagation losses arising from the multiple bends of the meanders waveguide are not considered in the study. We expect that additional loss arising from the several bends of the waveguides, particularly at wavelengths longer than 2 µm. Preliminary and ongoing studies performed in our laboratory did not see a significant impact from bends between 1.50 and 2 µm light, while the impact at 3 µm –using an optical parametric oscillator (OPO)– is currently underway.
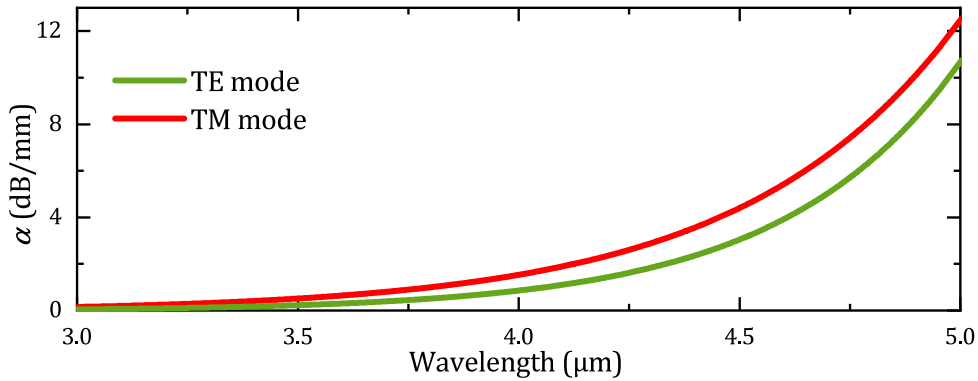
Fig. 5.4 Attenuation coefficient α as a function of wavelength for TM (red) and TE (green) polarization.

Figure 5.5 (a) shows the experimentally recorded spectra at the output of the waveguide for an average incident power of 100 mW and 112 mW for TE and TM input polarization, respectively. These values correspond to peak powers of 48 and 54 kW incident on the coupling optics. Estimating the actual fraction of peak power injected into the waveguide is not straightforward in long meanders waveguides. This is because it is difficult to distinguish the coupling losses from the propagation losses for a multi-curve waveguide geometry, as the one used here. In contrast with the straight waveguides of a total length of 5 mm studied in chapters 3 and 4, where the coupling losses are assumed to be equally distributed between input and output, in 5.5 cm long meanders waveguides, this assumption is not any more accurate. In all experiments reported in the chapter, the incident peak power ($Pp_{incident}$) is therefore reported, which is a parameter that can be reliably measured.

By looking at Fig. 5.5 (a), one can see the striking difference between the SC spectra generated in the two modes, caused by the different generating mechanisms. Specifically, in the TE mode, the anomalous waveguide GVD at the pump wavelength of 2.10 µm enables soliton-fission driven SCG. As a result, the input pulse breaks up into multiple fundamental solitons, and energy is simultaneously transferred to the phase-matched DWs located in the normal dispersion region.
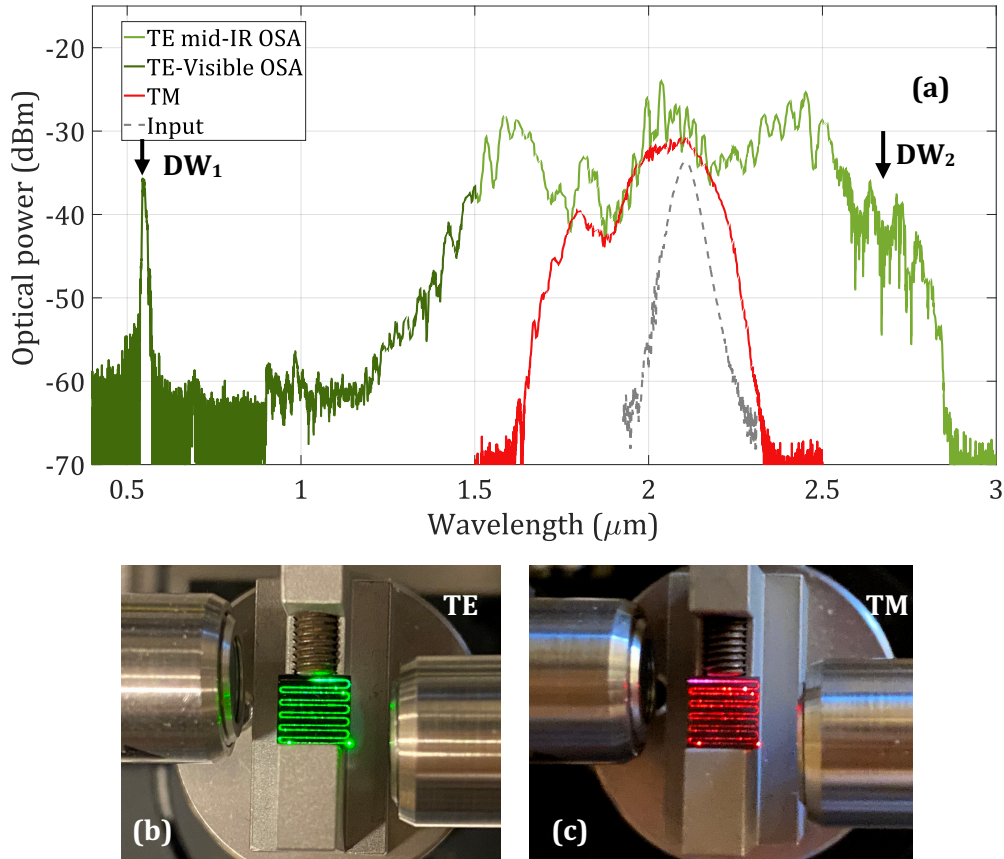
Fig. 5.5 (a) Experimental spectra measured at the output of the 5.5 cm long waveguide for TE (green) and TM (red) mode coupling. The incident peak power is estimated to be 48 kW and 54 kW for the TE and TM modes, respectively. The spectrum of the attenuated pump pulse is also shown in grey. Black arrows indicate the visible and mid-IR DW positions. Photographs of the waveguide captured from the top showing (b) green scattered light for TE excitation and (c) red scattered light for TM excitation. The waveguide is folded in meanders on a 5 mm x 5 mm chip. The light is coupled from the left-hand side at the top of the chip and collected at the bottom right.

The DW wavelengths in the visible at 547 nm (DW$_1$) and the mid-IR at a wavelength of 2.70 µm (DW$_2$) are in excellent agreement with theoretical predictions presented in Fig. 5.3. The result for the TE pumping is an octave-spanning SC spectrum extending from the visible to the mid-IR. The fact that the pump wavelength is located much closer to the second ZDW leads to the generation of an infrared DW close to the pump wavelength and a DW in the visible isolated from the SC spectrum. Changing the input polarization for TM pumping leads to a smooth and flat SC spectrum but with more limited bandwidth, typical of the ANDi regime and essentially dominated by SPM.

Photographs of the chip captured with a standard camera are shown in Fig. 5.5 (b) for TE and 5.5 (c) for TM pumping, supporting further the two different regimes observed depending on the input polarization.

In TM pumping, one can see the generation and scattering of red light near 700 nm from the input of the waveguide arising from third-harmonic generation (THG) of the 2.10 µm pump. THG is not observed in TE pumping, possibly because of the large phase mismatch for this process at this particular polarization. Instead, the generation of green light corresponding to the visible DW generated near 547 nm is seen. In contrast with the THG, the visible DW is not generated instantly at the waveguide's input, but after a distance of a few mm corresponding to the point of maximum higher-order soliton temporal compression and fission, l_c.

The dual TE/TM behavior of the generated SC source presented in Fig. 5.5 will be further investigated by carrying out a more detailed experimental and numerical study in the following sections of the chapter.

5.3 ANDi supercontinuum

In this section of the chapter, experimental results and numerical simulations will be presented for the TM polarization mode, which corresponds to the ANDi regime pumping.

The experimental evolution of the spectrum as a function of the incident peak pump power, $Pp_{incident}$, for TM mode, excitation is shown in Fig. 5.6. The experimental study is performed for five different incident peak powers starting from 1.9 kW up to the maximum power delivered by the pump laser, 54 kW. At lower pump powers, symmetrical spectral broadening due to the SPM-based SCG mechanism is observed. However, as the power increases, the spectrum starts exhibiting an asymmetry with enhanced broadening towards the shorter wavelengths. This can be explained by combining the very strong GVD slope and reduced dispersion below 2 µm wavelength range presented in Fig. 5.1.

Overall, the ANDi SC spectra present a remarkable flatness and smoothness, without any fine spectral features related to noise-driven dynamics.
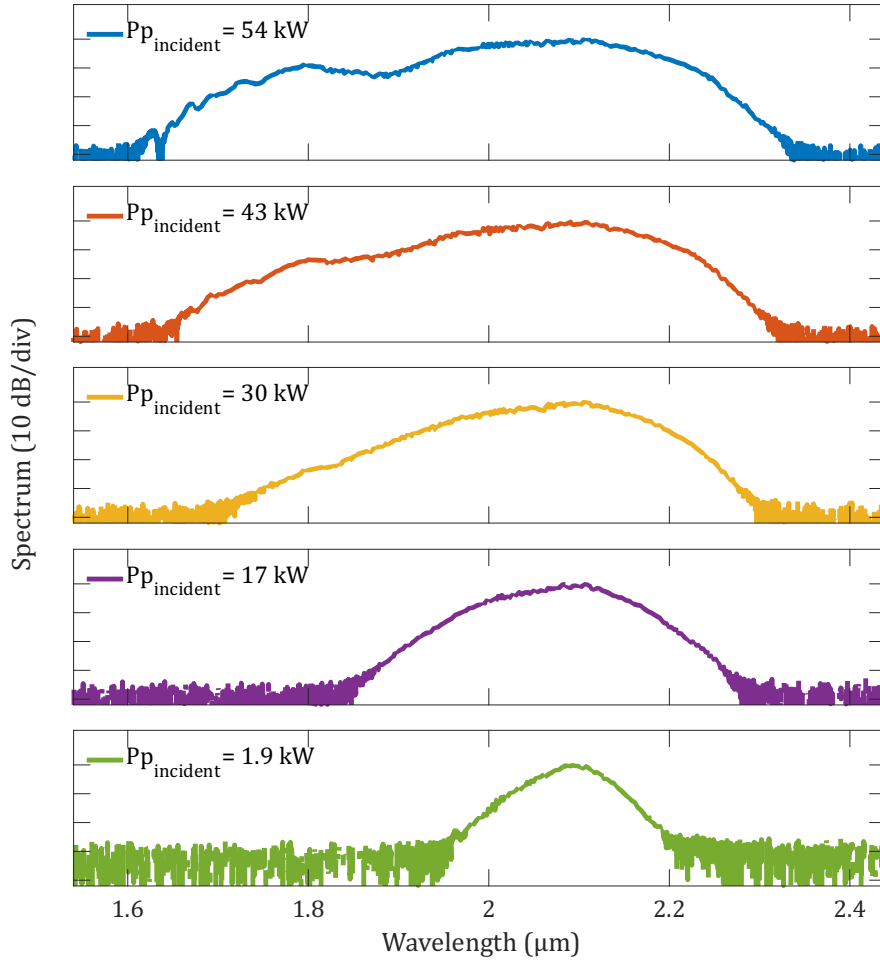
Fig. 5.6 Experimental SCG for TM-ANDi excitation for an increasing incident peak power from 1.9 kW to 54 kW.

Numerical simulations of the pulse propagation dynamics using the generalized nonlinear Schrödinger equation (GNLSE) are performed to understand the physical mechanisms behind spectral broadening better. The GNLSE is solved with a second-order Runge–Kutta algorithm in the frame of reference, moving at the group velocity of the input pulse and including high-order dispersion terms up to the 10th order. The dispersion profiles used in propagation simulations correspond to those presented earlier in Fig. 5.1. The parameters used to perform the numerical simulations of the supercontinuum generation are the nonlinear coefficient $n_2 = 2.4\ x\ 10^{-19}\ m^2\ W^{-1}$ and the nonlinearity γ, which is estimated as $\gamma = 0.47\ m^{-1}W^{-1}$ for an effective mode area $A_{eff} = 1.53\ \mu m^2$ at the pump wavelength of 2.10 μm for the uncladded waveguide under investigation. The temporal intensity of the pump pulses is assumed to be hyperbolic secant (sech²). Pulses are slightly chirped due to the coupling optical components, resulting in an injected pulse duration of 110 fs (FWHM) at the chip entrance. Input chirp is included in the simulations for more accurate results.

As previously mentioned, the estimation of the coupled power in the case of meanders uncladded waveguides is difficult. As a result, the injected peak power indicated in

simulation graphs is scaled proportionally from the experimentally measured incident peak powers by a fixed coupling coefficient. This coefficient is given by the ratio of incident average power divided by the measured average output power, $c = P_{incident}/P_{output}$, which is used as a free-running parameter in the simulations. Utilizing this approach, the fraction of incident peak power coupled into the TM mode that matches best with the experimental measurements presented in Fig. 5.6 is estimated to be 15 %.

In Fig. 5.7, simulated output spectra for the five experimentally measured spectra shown in Fig. 5.6 are presented. The graphs show a near-perfect agreement with the experiments, confirming the flat and smooth ANDi spectra generated for TM polarization mode. The maximum obtained bandwidth for the ANDi SC spans from 1.60 µm to 2.30 µm.

Fig. 5.7 Numerically simulated SCG for TM-ANDi excitation, for injected peak power values starting from 270 W up to 7.6 kW.

The simulated spectral and temporal pulse propagation evolution along the length of the waveguide (5.5 cm) in the TM mode are plotted in Fig. 5.8 (a) and (b) for a maximum coupled pump power estimated as 7.6 kW. Both graphs show typical ANDi SCG dynamics. One can see that SCG occurs mainly in the first few mm of the waveguide. The SPM-

dominated spectral broadening is initially symmetrical, and as the spectrum expands, the asymmetry becomes more pronounced due to higher-order dispersion (HOD).

In the time domain, the input pulse gradually stretches due to the large normal dispersion value, which prevents additional nonlinear spectral broadening beyond the first 5 mm of propagation. It is worth mentioning that in contrast to soliton-fission driven dynamics seen in chapter 3, the associated temporal envelope for the ANDi SC source, Fig. 5.8 (b), preserves its single pulse configuration with limited fine structure.

Fig. 5.8 Simulated (a) spectral and (b) temporal normalized pulse propagation along the 5.5 cm waveguide when pulses with 7.6 kW peak power are injected in the TM polarization mode.

Due to the strong normal dispersion regime in TM polarization excitation, one may expect the SC pulses to exhibit quasi-linear chirp. To confirm this, in Fig. 5.9 the simulated spectrogram of the ANDi supercontinuum at the waveguide's output is presented for the maximum injected peak power of 7.6 kW.

The spectrogram shows a single pulse that has been stretched to approximately 6 ps at the output of the waveguide. The smooth and near-parabolic phase variation across the entire spectrum corresponds to a quasi-linear chirp. As a result, the single output pulse could be efficiently re-compressed using a grating or a prism pair [169].
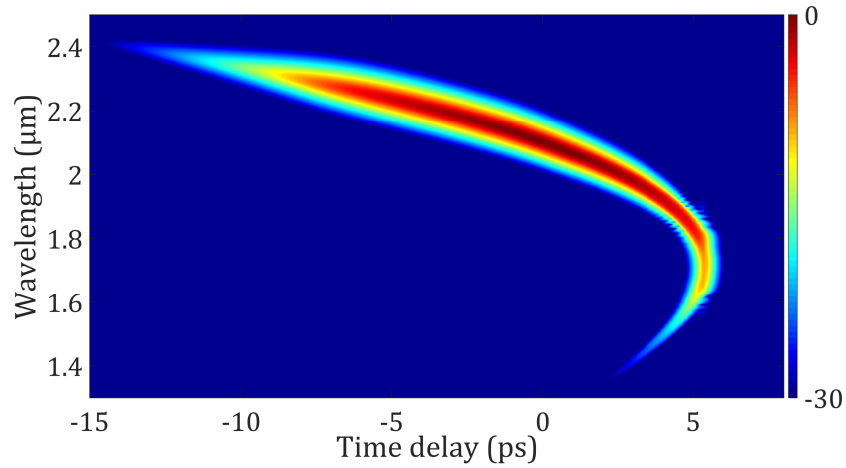
Fig. 5.9 Simulated spectrogram of ANDi supercontinuum in TM mode at a maximum coupled peak power of 7.6 kW.

5.4 Soliton fission-driven supercontinuum

Finally, we look at the soliton fission-driven supercontinuum. The study begins by illustrating the experimental evolution of spectra while pumping in the TE – anomalous dispersion regime for increasing incident peak power. Fig. 5.10 shows the experimentally obtained spectra for six different incident peak powers varying from 630 W up to 48 kW. At a threshold of 1.3 kW, the generation of a mid-IR DW at a wavelength of 2.7 µm is observed. Further increase of the pump power to 12 kW results in a significant spectral broadening and the generation of a visible DW at approximately 547 µm. We can indeed expect the mid-IR DW to be generated closer to the input of the waveguide since less broadening of the pump pulse is required for mid-IR generation, compared with the visible DW, which is spectrally located further away. Continuously increasing the power up to the maximum of 48 kW leads to an additional spectral expansion. In particular, the spectrum grows towards the short-wavelength spectral range. An increase in both visible and mid-IR DW's powers is observed as more power is coupled to the waveguide. Thus, the maximum spectral bandwidth of the soliton fission-driven SC reaches more than an optical octave, spanning from 547 nm to 2.67 µm at a bandwidth of -30 dB.
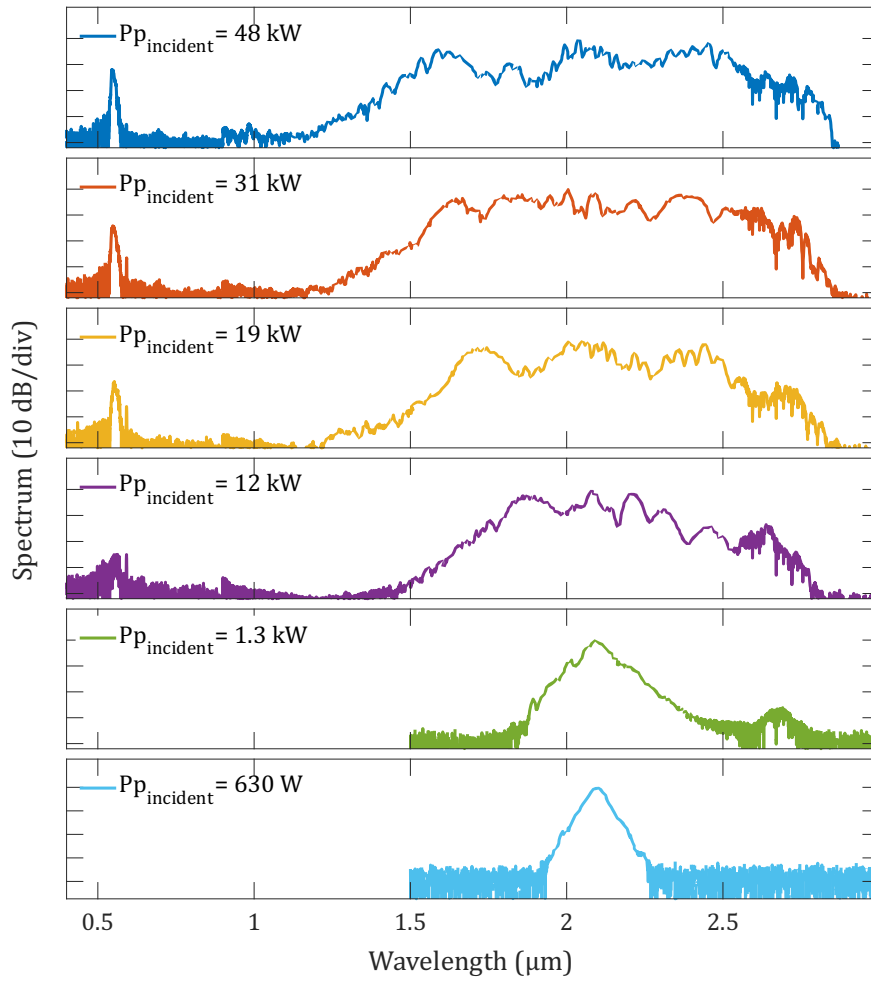
Fig. 5.10 Experimental SCG for TE-soliton fission-driven excitation for an increasing incident peak power varying from 630 W to 48 kW.

Once again, numerical simulations based on GNLSE are performed to get insights into the SC dynamics. The injected peak power is scaled proportionally from the experimentally measured incident peak powers by a fixed coupling coefficient *c* defined before, which is used as a free-running parameter in the simulations. Utilizing this approach, the fraction of incident peak power coupled into the TE mode that matches best with the experimental measurements presented in Fig. 5.10 is estimated to be 8 %. The simulated SC spectra for TE input polarization are presented in Fig. 5.11 as a function of injected peak power. In particular, the spectral shape, bandwidth, and location of both visible and mid-IR DWs are well predicted by the simulations.
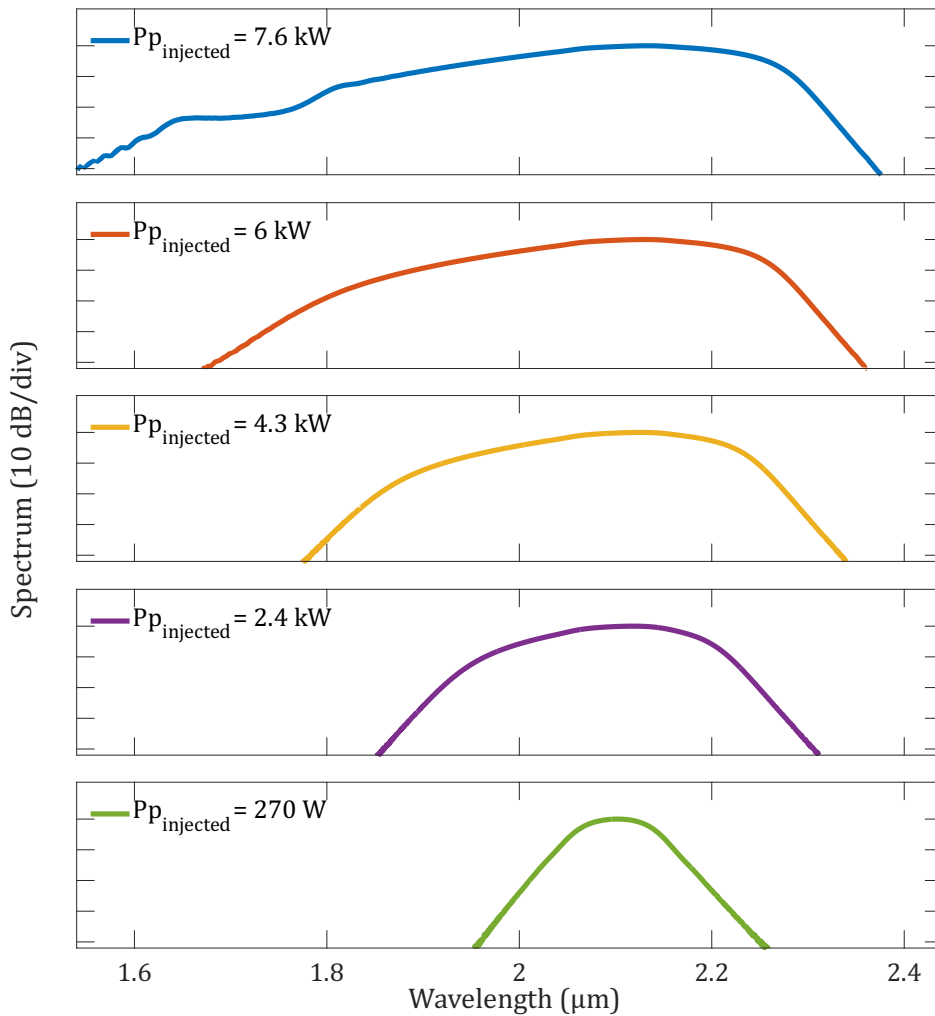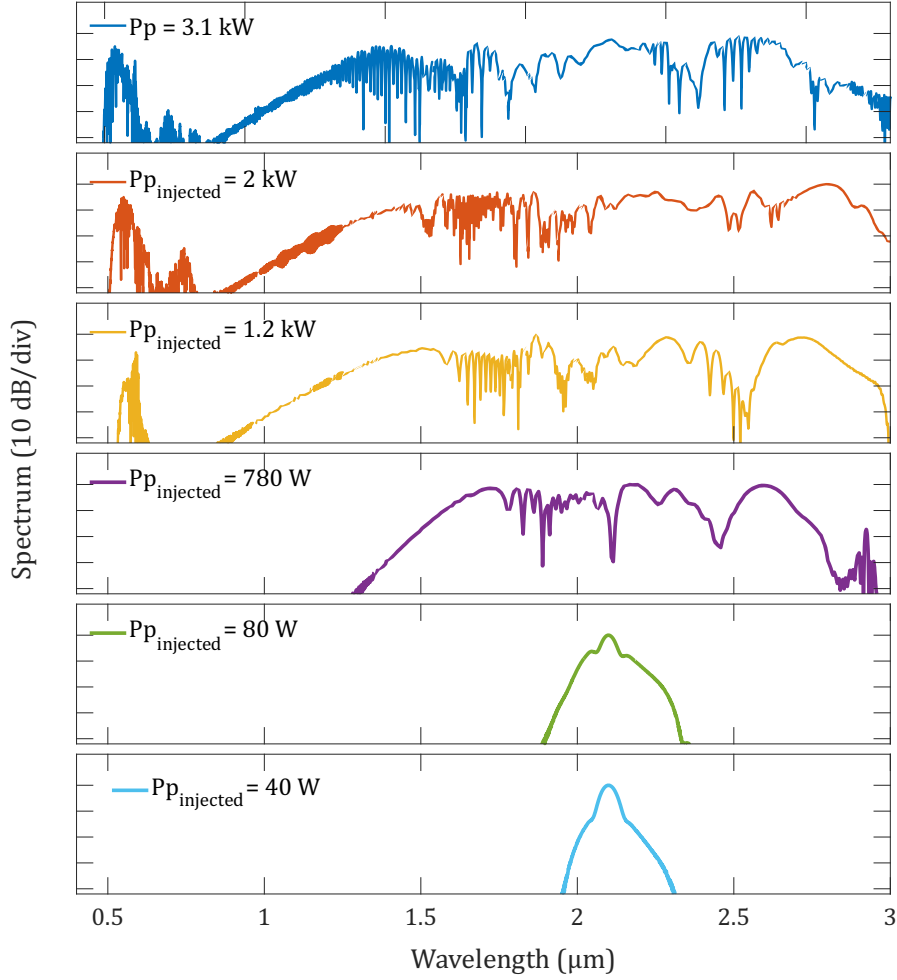
Fig. 5.11 Numerically simulated SCG for TE excitation, for injected peak power values starting from 40 W up to 3.1 kW.

A discrepancy is observed in the longer wavelength spectral range for the highest power values, where the simulated SC spectra extend further towards the mid-IR compared to experimental measurements. This can be attributed to the uncertainty on the dispersion profile shown in Fig. 5.1, simulated with Comsol Multiphysics assuming a perfect 2D structure. Moreover, increased losses in the long-wavelength side arising from the waveguide bends and fabrication imperfections can be another reason for the mismatch between simulated and measured spectra.

To confirm the nature of the soliton dynamics that leads to the SC generation in the TE mode, Fig. 5.12 illustrates the simulated SC spectral and temporal evolution corresponding to the highest incident peak power used in experiments. The spectral evolution in Fig. 5.12 (a) shows an initial near-symmetric broadening with maximum spectral expansion observed after approximately 3 mm of pulse propagation. After this soliton compression point l_c at 4 mm, the pump pulse is transformed into a higher-order soliton that rapidly breaks up into multiple fundamental solitons. Then, finally, the energy is transferred to the phase-matched DWs in the normal dispersion regime. The generation

of the visible and the mid-IR DWs is observed in Fig. 5.12 (a) but can also be visually confirmed by the scattered green light on top of the waveguide, shown in Fig. 5.5 (b).
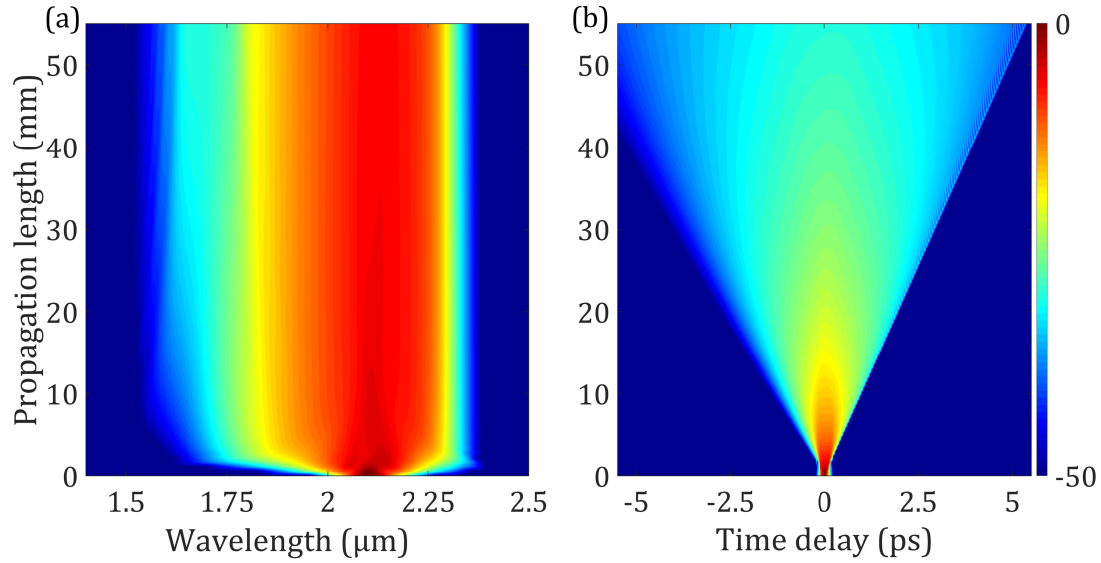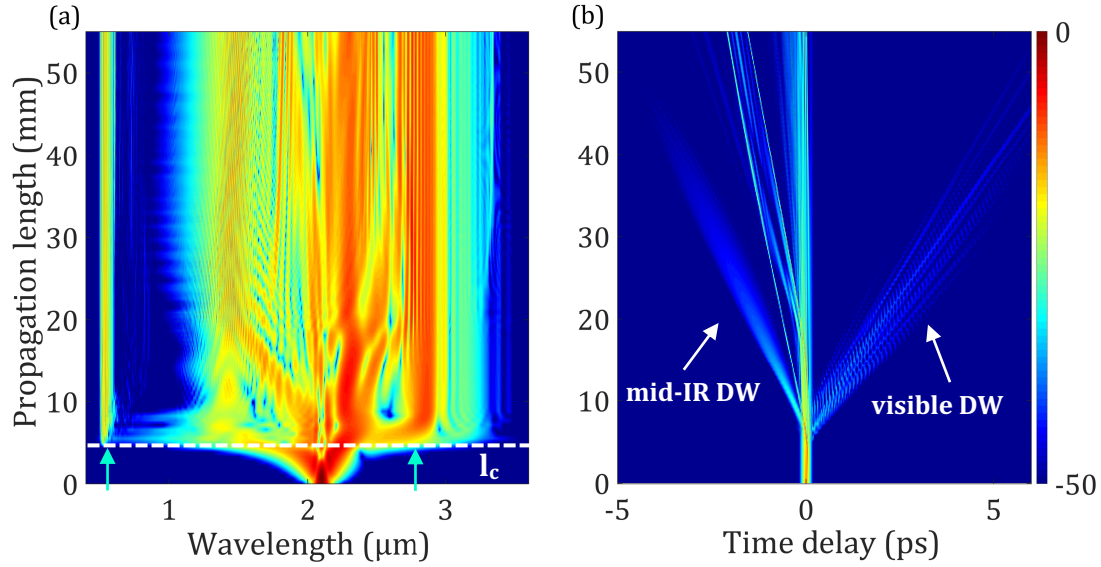

Fig. 5.12 Numerically simulated (a) spectral and (b) temporal normalized pulse propagation along the 5.5 cm waveguide length, when pulses with 3.1 kW peak power are injected in the TE mode. Soliton compression point is indicated with a white dashed line in a propagation length of 4 mm. Arrows indicate the positions of the generated DWs.

In the time domain, Fig. 5.12 (b), the pulse corresponds to a higher-order soliton experiencing soliton-fission dynamics with maximum temporal compression reached after 4 mm. This distance is slightly larger than what was seen in the experiments above (approximately 3 mm). This difference can be attributed to a deviation from the ideal dispersion profile used in the numerical simulations. At this point in the propagation, the spectrum expands significantly into the normal dispersion regimes, and HOD terms lead to the fission of the compressed pulse into two fundamental solitons. The generation of two distinct DWs further accompanies the fission in the normal dispersion regions at 547 nm and 2.70 μm, respectively, which rapidly walk off from the pump temporal residue. The DWs in the visible and the IR experience increased and reduced group delay compared to the pump. As a result, they appear at the trailing and the leading edge of the temporal window of Fig. 5.12 (b), respectively.

The ejected solitons during the soliton-fission process experience a strong spectral recoil towards the short wavelengths from the DW component at 2.7 μm, inducing a downshift of their central wavelength. This consequently obliges the locations of the solitons to be found in negative times within the temporal window. Moreover, the fundamental solitons exhibit a quasi-linear trajectory in the space-time plane. Propagation beyond the fission distance leads to some interactions between the individual solitons and DWs, yielding a slight increase in the SC spectral bandwidth. Still, the spectral broadening process is limited after the first 1 cm of propagation.

The dynamics at the temporal domain are also confirmed by the simulated spectrogram shown in Fig. 5.13. Solitons ejected after the soliton-fission process are identified, and DWs are generated in the visible and the mid-IR by the soliton with the largest amplitude.
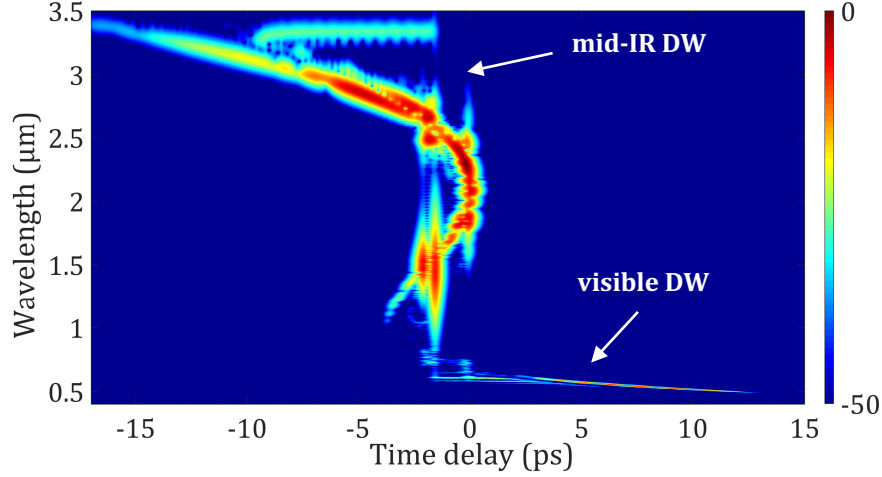
Fig. 5.13 Simulated spectrogram of supercontinuum in TE mode at a maximum coupled peak power of 3.1 kW.

Moreover, we investigate the noise sensitivity of the on-chip generated SC source in both pumping regimes. To that end, the first-order degree of coherence $g_{12}^{(1)}$ is simulated, using the one-photon-per-mode approximation to model the noise background of the input pulse [117].

The calculated complex degree of first-order coherence $g_{12}^{(1)}$ is given by the equation:

$$g_{12}^{(1)}(\lambda) = \frac{\langle E_1^*(\lambda)E_2(\lambda)\rangle}{\sqrt{\langle|E_1(\lambda)|^2\rangle\langle|E_2(\lambda)|^2\rangle}} \quad (5.1)$$

where E_1^* and E_2 are conjugate pairs of individual supercontinuum complex spectral envelopes.

Fig. 5.14 shows the coherence of the entire SC band for (a) TE soliton fission-driven SC and (b) TM-ANDi SC calculated for 100 independent realizations with different seed noise as equation (5.1) dictates. Both plots correspond to the highest injected peak powers, 3.1 kW and 7.6 kW for TE and TM modes, respectively.

One can see that the spectrum essentially maintains an excellent degree of coherence over the entire SC bandwidth in both pumping regimes. However, some small fluctuations can be observed around the wavelength of the solitons and visible DW in Fig. 5.14, attributed to the soliton-fission nature of the SC process. Although the soliton fission dynamics can degrade the phase coherence of the generated SC significantly, preserving a low number of solitons like in this case ($N \cong 5$) can guarantee a high coherence.

On the other hand, ANDi SC preserves, as expected, a very high degree of coherence on its entire bandwidth. Generally, due to the perfect coherence of ANDi SC schemes, even a single run of simulations is sufficient to obtain the spectra presented in Fig. 5.14 (b). However, the same number of runs is used in both cases.
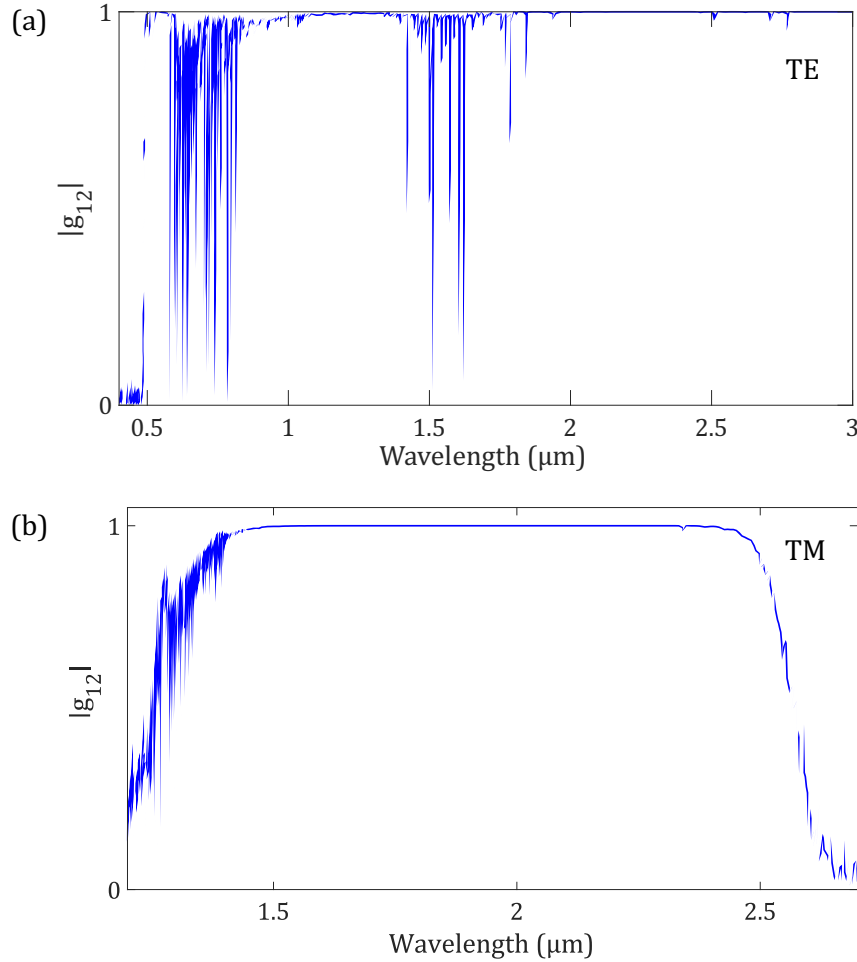
Fig. 5.14 Simulated first-order degree of coherence at the uncladded waveguide output for (a) an injected peak power of 3.1 kW at TE polarization mode (soliton fission driven SC) and (b) peak power of 7.6 kW at TM polarization mode (ANDi SC).

Finally, to further support the importance of the dual-dispersion regime for SC generation in the uncladded waveguide at the 2.10 µm pumping wavelength, the same experiment is performed while pumping the waveguide at 1.56 µm. According to the GVD simulations presented in Fig. 5.1, both TE and TM polarization modes in the waveguide experience anomalous dispersion pumping at 1.56 µm. As a result, only TE polarization mode is presented since the two modes do not experience a different profile and the underlying dynamics are the same.

The experimental setup is the same as for the 2.10 µm pumping, replacing the 2-micron optical components with standard telecom-wavelengths ones. A compact turn-key femtosecond MLL (FemtoFErb 1560, Toptica) with a repetition rate of 100 MHz and a

pulse duration of approximately 80 fs (FWHM) is utilized to pump the uncladded waveguide. The fiber laser output is collimated and directed in a free space configuration to the input lens. Total transmission losses are measured as 11 dB for TE polarization mode at the pump wavelength for a low pump power to avoid spectral broadening. Experimental measurements for the TE pumping are presented in Fig. 5.15 for the same incident peak powers used in the 2.10 µm pumping study for a fair comparison.

The total transmission losses including in/out-coupling, propagation losses, and Fresnel reflection from the waveguide facets, are measured at the pump wavelength with low power in the absence of spectral broadening for TE polarization

Looking at Fig. 5.15, only the visible DW is generated at a wavelength of 532 nm. Even measuring the spectra beyond 2.4 µm does not show the appearance of the mid-IR DW predicted by simulations of integrated dispersion in Fig. 5.2. The predicted mid-IR DW position is too far from the pump, approximately around 3.35 µm, and according to the β_{int} curve, the energy transfer towards the mid-IR is less efficient compared to the 2 µm pumping. As a result, the uncladded waveguides of 2.00 µm x 0.75 µm cross-section exhibit interesting SC properties only at a SWIR pumping wavelength beyond 2 µm.
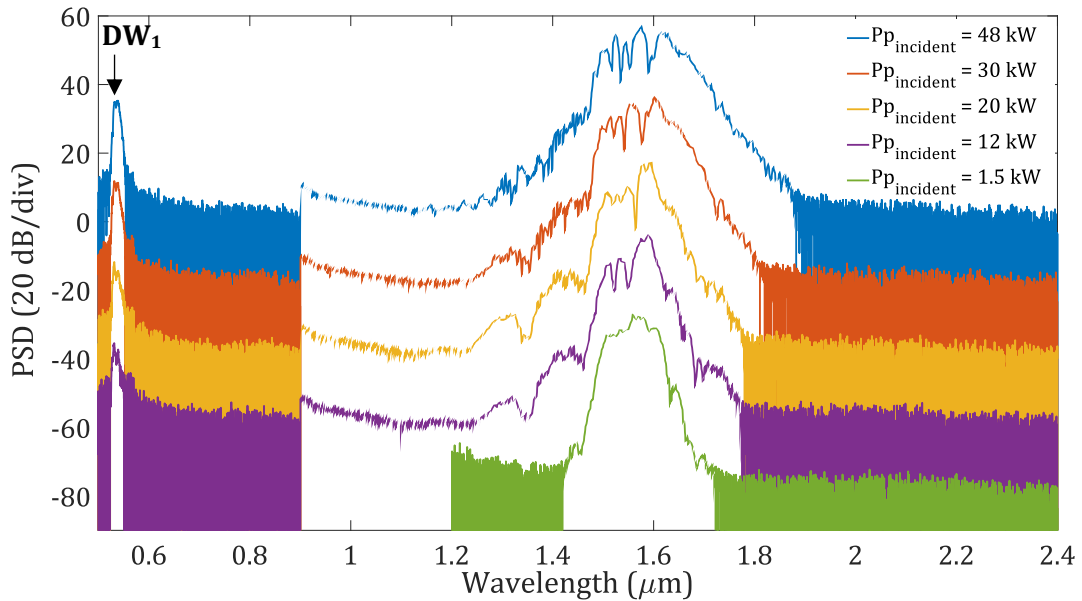
Fig. 5.15 Experimental SCG for TE-soliton fission-driven excitation for an increasing incident peak power varying from 1.5 W to 48 kW for a pumping wavelength of 1.56 µm.

Numerical simulations of the spectral evolution of the TE soliton fission-driven SC pumped at 1.56 µm are presented in Fig. 5.16 to confirm its limitations in terms of an efficient mid-IR reach. The simulated pulse propagation corresponds to a maximum injected power of 3.1 kW. After the soliton fission point at approximately 2.2 mm, two dispersive waves are generated, one in the visible and the second one in the mid-IR as β_{int} dictates. However, the large distance separating the pump from the mid-IR DW significantly limits the energy transfer. Thus, we are not able to experimentally observe the 3.3 µm.
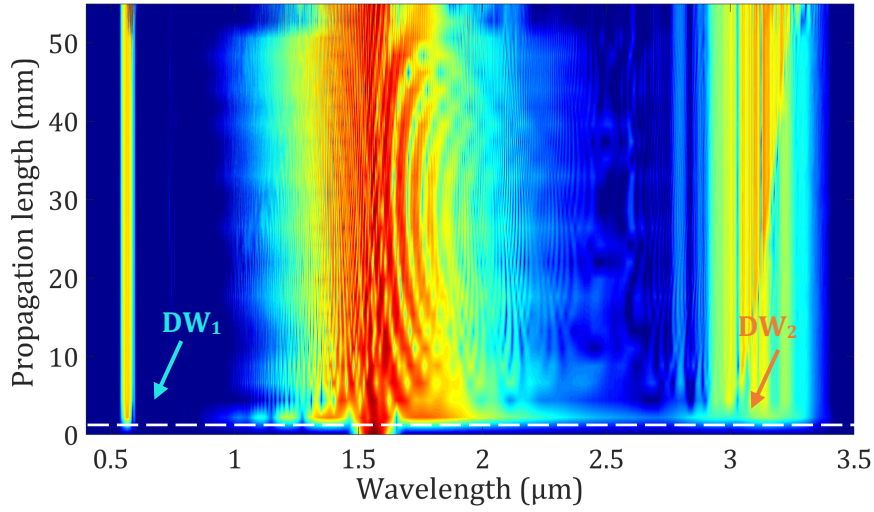
Fig. 5.16 Numerically simulated spectral evolution along the 5.5 cm waveguide length, when pulses with 3.1 kW peak power are injected in the TE mode. Soliton compression point is indicated with a white dashed line in a propagation length of 2 mm. Arrows indicate the positions of the generated DWs.

Moreover, the selection of 1.56 µm as the pump wavelength does not offer the advantage of ANDi SC generation in TM mode. For both TE and TM polarization modes, we obtain a soliton fission-driven SC.

5.5 Conclusions

This chapter demonstrates a SWIR supercontinuum source with extreme polarization sensitivity in an uncladded Si$_3$N$_4$ waveguide platform. Leveraging TM or TE dispersion-engineering of the air-cladded scheme, one can obtain SC spectra at the waveguide output with very different characteristics by simply adjusting the input polarization of the pump. Specifically, under TM mode excitation, an ultra-flat, SPM-dominated ANDi SC spanning from 1.60 µm to 2.30 µm is generated, exhibiting high power density and a high degree of coherence. On the other hand, TE polarization excitation yields an octave-spanning SC with spectral coverage from the visible up to 3 µm. Soliton-fission dynamics drive this broadband SC as the 2.10 µm pump lies in the anomalous dispersion regime of the uncladded waveguide. Numerical simulations are in excellent agreement with experimental measurements, confirming the dual-regime performance of the developed SC source. Having both anomalous and ANDi SC from a single chip and a single Si$_3$N$_4$ waveguide offers significant flexibility in a simple design.

By a simple adjustment of polarization, one can favor at will either smooth and coherent ANDi or broadband soliton-fission driven SC, depending on the application. For instance, a broad spectral bandwidth obtained at TE mode can be used in on-chip spectroscopy and direct sensing. In contrast, the ultra-flat spectrum at TM mode offers the possibility of pulse compression and few-cycle pulse generation.

Chapter 6

Conclusions and future perspectives

Conclusions and future perspectives

Significant progress in the development of novel mid-IR light sources has been accomplished during the last decade, and new spectrometric techniques have come into play, profiting from these sources. Supercontinuum generation (SCG) is one of the most attractive and common ways to access the mid-IR spectral range, where strong absorption lines of many essential molecules reside. Owing to its large spectral broadening that can reach multi-octave levels, SC successfully drives spectroscopy. An interesting alternative to optical fiber-based SCG is to pump integrated waveguides with femtosecond lasers. Integrated platforms offer the advantage of a reduced footprint and the lithographic control of the dispersion.

In this thesis, we focus on Si_3N_4 waveguides, exploring new capabilities of SCG in this platform, not only by providing experimental and theoretical results on the significantly enhanced conversion efficiency towards the mid-IR, but we go one step beyond and bring new insights into the utilization of the mid-IR radiation generated on-chip as a tool for spectroscopy measurements.

Leveraging the dispersive wave generation (DWG) mechanism induced by soliton-fission driven SC, efficient mid-IR radiation from a tunable, turn-key femtosecond SWIR fiber laser is achieved. A combination of state-of-the-art Si_3N_4 waveguide fabrication with a particular design and fiber laser technology with a proper choice of pumping parameters enables significant favoring of the mid-IR DWG while reducing the energy transfer to the visible DW. As a result, we report the highest conversion efficiency (CE) up to date for on-chip mid-IR DWG, which reaches 35%. Furthermore, by switching between different waveguide widths, the entire spectral region between 3 – 4 µm is covered, with milliwatt level on-chip powers and milliwatt level output powers. Although the efficiency decreases for DWs generated deeper in the mid-IR, we can still obtain average output powers up to 2 mW in the mid-IR region. These values represent a significant improvement in conversion efficiency compared to previous mid-IR SCG [110]. In addition, the achieved mid-IR output power levels are sufficient for direct absorption spectroscopy applications. By pumping a single straight waveguide with a fiber laser, a mid-IR DW spanning from 2.95 to 3.4 µm is generated. This simple scheme is used for the simultaneous detection of three different gas-phase species -acetylene (C_2H_2), methane (CH_4), and ethane (C_2H_6)-, with several hundreds of parts-per-million (ppm) detection limit in a 5 cm long gas cell.

Overall, the development of a simple SC-based source with a bandwidth between 2 – 4 µm has been achieved, and its utilization in multi-species gas absorption spectroscopy has been successfully established at a ppm level in a very short gas cell.

However, limitations arising from these promising results still leave room for further improvement. For example, three main parameters could be improved in a future study: 1) the detection limit, 2) conversion efficiency, and 3) fully on-chip integration.

The easiest way to anticipate the ppm-detection limit obtained in this thesis would be to utilize much longer optical path lengths while interrogating the gas samples. For example, multi-pass gas cells like the cells presented in [170,171] could significantly improve the detection sensitivity of our device and the SNR. However, the few milliwatt-level mid-IR DW output power constitutes the alignment to such a type of cell impossible due to many reflections of the mid-IR beam in the mirrors.

This suggestion gives rise to discussion of another main constrain: how to increase the output mid-IR power. In fact, there are two ways towards the improvement of the mid-IR power. One solution could be to use a pump source with a higher repetition rate than the 19 MHz femtosecond mode-locked laser (MLL) seeding the SC in our Si_3N_4 waveguides. Frequency combs at 2 μm with similar pulse duration but much higher repetition rates are now available [70] to drive SC. As a consequence, with a higher average power in the waveguide's input, the power transferred to the mid-IR would be enhanced.

Moreover, the relatively large input and output coupling losses and fabrication defects observed as scattering points along the waveguides degrade the delivered output mid-IR power. To that end, new types of in/out coupling tapers [172] could dramatically decrease the in/out coupling losses, improving the coupled power into the waveguides and, as a result, the wavelength conversion efficiency and thus the output mid-IR DW power. Therefore, this could further enhance the performance of the on-chip generated SC as a spectroscopic device.

Working on a fully integrated platform has been envisioned for a long time, and efforts of the scientific community towards the integration of MLLs on a chip have now become a reality [173,174]. MLL structures presented in [174] use photonic integrated circuits (PICs) made of indium phosphide (InP) and SiN could be a very interesting approach towards the direction of a fully on-chip scheme. However, the current pulse is not transform-limited, and the achieved pulse durations cannot drive SCG as of now. Moreover, the so far achieved average output powers are still limited to allow for optimal nonlinear wavelength conversion [173]. On the other hand, by co-integrating such a MLL on the Si_3N_4 waveguides used in the thesis would enable a compact and portable solution for environmental gas spectroscopy, significantly reducing the footprint of the presented simple spectroscopy scheme.

In the last part of this thesis, an air-cladded waveguide design enables the generation of a SC source with extreme polarization sensitivity. A dramatic change of the dispersion profile between the TM and TE mode at a pumping wavelength of 2.1 μm results in a flat and highly coherent ANDi SC or a broadband soliton fission-driven SC generation up to 3 μm for TM and TE, respectively. Having both anomalous and ANDi SCG from a single chip offers significant flexibility, specifically ANDi, that has the advantage of nonlinear pulse compression [175].

Especially on-chip pulse compression is particularly interesting, connecting the short pulse generation and the compactness that only on-chip generated sources can offer [176,177]. On-chip pulse compression can be achieved either in the ANDi regime [176] or in the solitonic regime [177], with trade-offs between the obtained short pulse duration at FWHM -shorter on-chip compressed pulses achieved at soliton regime- and the pulse

quality. In general, ANDi schemes offer enhanced quality of the compressed pulse [176], paid by the price of a less short compressed pulse duration.

As an overall conclusion, thesis results open new perspectives for the generation of versatile broadband SC light sources in the 2 – 4 µm spectral range in Si_3N_4 waveguides, whose characteristics can be tailored to satisfy diverse applications. For example, we can either achieve simultaneous multi-gas detection in a cladded Si_3N_4 waveguide or benefit from the polarization-sensitive behavior of the air-cladded waveguide geometry. For the latter, the stable and flat nature of ANDi SC can be used in pulse compression applications and few-cycle pulse generation, while the broad soliton fission-driven SC in the same waveguide can be used in on-chip spectroscopy and sensing.

References

1. M. Vainio and L. Halonen, "Mid-infrared optical parametric oscillators and frequency combs for molecular spectroscopy," Physical Chemistry Chemical Physics **18**(6), 4266–4294 (2016).

2. P.Atkins, *Elements of Physical Chemistry* (2006).

3. I. E. Gordon, L. S. Rothman, C. Hill, R. V. Kochanov, Y. Tan, P. F. Bernath, M. Birk, V. Boudon, A. Campargue, K. V. Chance, B. J. Drouin, J. M. Flaud, R. R. Gamache, J. T. Hodges, D. Jacquemart, V. I. Perevalov, A. Perrin, K. P. Shine, M. A. H. Smith, J. Tennyson, G. C. Toon, H. Tran, V. G. Tyuterev, A. Barbe, A. G. Császár, V. M. Devi, T. Furtenbacher, J. J. Harrison, J. M. Hartmann, A. Jolly, T. J. Johnson, T. Karman, I. Kleiner, A. A. Kyuberis, J. Loos, O. M. Lyulin, S. T. Massie, S. N. Mikhailenko, N. Moazzen-Ahmadi, H. S. P. Müller, O. V. Naumenko, A. V. Nikitin, O. L. Polyansky, M. Rey, M. Rotger, S. W. Sharpe, K. Sung, E. Starikova, S. A. Tashkun, J. Vander Auwera, G. Wagner, J. Wilzewski, P. Wcisło, S. Yu, and E. J. Zak, "The HITRAN2016 molecular spectroscopic database," Journal of Quantitative Spectroscopy and Radiative Transfer (2017).

4. D. Popa and F. Udrea, "Towards integrated mid-infrared gas sensors," Sensors **19**(9), 1–15 (2019).

5. M. Meinshausen, S. J. Smith, K. Calvin, J. S. Daniel, M. L. T. Kainuma, J. Lamarque, K. Matsumoto, S. A. Montzka, S. C. B. Raper, K. Riahi, A. Thomson, G. J. M. Velders, and D. P. P. van Vuuren, "The RCP greenhouse gas concentrations and their extensions from 1765 to 2300," Climatic Change **109**(1), 213–241 (2011).

6. K. S. V. Santhanam and N. N. N. Ahamed, "Greenhouse gas sensors fabricated with new materials for climatic usage: A review," ChemEngineering **2**(3), 1–30 (2018).

7. W. B. Grant, R. H. Kagann, and W. A. McClenny, "Optical Remote Measurement of Toxic Gases," Journal of the Air and Waste Management Association **42**(1), 18–30 (1992).

8. K. J. Major, M. K. Poutous, K. F. Dunnill, K. J. Ewing, J. S. Sanghera, P. C. Deguzman, and I. D. Aggarwal, "Evaluation of a biomimetic optical-filter based chemical sensor for detection of hazardous chemical vapors in the infrared," Detection and Sensing of Mines, Explosive Objects, and Obscured Targets XXI **9823**(May 2016), 98230U (2016).

9. A. Bajtarevic, C. Ager, M. Pienz, M. Klieber, K. Schwarz, M. Ligor, T. Ligor, W. Filipiak, H. Denz, M. Fiegl, W. Hilbe, W. Weiss, P. Lukas, H. Jamnig, M. Hackl, A. Haidenberger, B. Buszewski, W. Miekisch, J. Schubert, and A. Amann, "Noninvasive detection of lung cancer by analysis of exhaled breath," BMC Cancer **9**, 348 (2009).

10. G. Song, T. Qin, H. Liu, G. B. Xu, Y. Y. Pan, F. X. Xiong, K. S. Gu, G. P. Sun, and Z. D. Chen, "Quantitative breath analysis of volatile organic compounds of lung cancer patients," Lung Cancer **67**(2), 227–231 (2010).

11. D. Etezadi, J. B. Warner, F. S. Ruggeri, G. Dietler, H. A. Lashuel, and H. Altug, "Nanoplasmonic mid-infrared biosensor for in vitro protein secondary structure detection," Light: Science and Applications **6**(8), e17029-10 (2017).

12. Y. Zhu, Z. Li, Z. Hao, C. DiMarco, P. Maturavongsadit, Y. Hao, M. Lu, A. Stein, Q. Wang, J. Hone, N. Yu, and Q. Lin, "Optical conductivity-based ultrasensitive mid-infrared biosensing on a hybrid metasurface," Light: Science and Applications **7**(1), 1–11 (2018).

13. R. Ghosh, J. W. Gardner, and P. K. Guha, "Air Pollution Monitoring Using Near Room Temperature Resistive Gas Sensors: A Review," IEEE Transactions on Electron Devices **66**(8), 3254–3264 (2019).

14. A. O. Perez, B. Bierer, L. Scholz, J. Wöllenstein, and S. Palzer, "A wireless gas sensor network to monitor indoor environmental quality in schools," Sensors **18**(12), 1–13 (2018).

15. U. Willer, M. Saraji, A. Khorsandi, P. Geiser, and W. Schade, "Near- and mid-infrared laser monitoring of industrial processes, environment and security applications," Optics and Lasers in Engineering **44**(7), 699–710 (2006).

16. R. I.-C. and Leonardo C. Pacheco-Londoño, John R. Castro-Suarez, Nataly J. Galán-Freyle, Amanda M. Figueroa-Navedo, José L. Ruiz-Caballero, "Mid-Infrared Laser Spectroscopy Applications I: Detection of Traces of High Explosives on Reflective and Matte Substrates," Intech 13 (2016).

17. F. K. Tittel, M. Lewicki Rafałand Jahjah, B. Foxworth, Y. Ma, L. Dong, R. Griffin, K. Krzempek, P. Stefanski, and J. Tarka, "Mid-infrared Laser Based Gas Sensor Technologies for Environmental Monitoring, Medical Diagnostics, Industrial and Security Applications," in *Terahertz and Mid Infrared Radiation: Detection of Explosives and CBRN (Using Terahertz)*, M. F. Pereira and O. Shulika, eds. (Springer Netherlands, 2014), pp. 153–165.

18. M. Hernández-Martínez, T. Gallardo-Velázquez, G. Osorio-Revilla, N. Almaraz-Abarca, and E. Castañeda-Pérez, "Application of MIR-FTIR spectroscopy and chemometrics to the rapid prediction of fish fillet quality," CYTA - Journal of Food **12**(4), 369–377 (2014).

19. Y. Ma, H. He, J. Wu, C. Wang, K. Chao, and Q. Huang, "Assessment of Polysaccharides from Mycelia of genus Ganoderma by Mid-Infrared and Near-Infrared Spectroscopy," Scientific Reports **8**(1), 1–10 (2018).

20. W. H. Su and D. W. Sun, "Mid-infrared (MIR) Spectroscopy for Quality Analysis of Liquid Foods," Food Engineering Reviews **11**(3), 142–158 (2019).

21. F. Hempel, V. Artyushenko, F. Weichbrodt, and J. Röpcke, "Application of quantum cascade lasers and infrared-fibres for the monitoring and control of industrial plasma processes," Journal of Physics: Conference Series **157**, (2009).

22. Z. D. Weller, S. P. Hamburg, and J. C. Von Fischer, "A National Estimate of Methane Leakage from Pipeline Mains in Natural Gas Local Distribution Systems," Environmental Science and Technology **54**(14), 8958–8967 (2020).

23. A. Coustenis, A. Salama, B. Schulz, S. Ott, E. Lellouch, T. Encrenaz, D. Gautier, and H. Feuchtgruber, "Titan's atmosphere from ISO mid-infrared spectroscopy," Icarus **161**(2), 383–403 (2003).

24. T. D. Robinson, K. Ennico, V. S. Meadows, W. Sparks, D. B. J. Bussey, E. W. Schwieterman, and J. Breiner, "Detection of ocean glint and ozone absorption using LCROSS earth observations," Astrophysical Journal **787**(2), (2014).

25. K. Wagner, A. Boehle, P. Pathak, M. Kasper, R. Arsenault, G. Jakob, U. Käufl, S. Leveratto, A.-L. Maire, E. Pantin, R. Siebenmorgen, G. Zins, O. Absil, N. Ageorges, D. Apai, A. Carlotti, É. Choquet, C. Delacroix, K. Dohlen, P. Duhoux, P. Forsberg, E. Fuenteseca, S. Gutruf, O. Guyon, E. Huby, D. Kampf, M. Karlsson, P. Kervella, J.-P. Kirchbauer, P. Klupar, J. Kolb, D. Mawet, M. N'Diaye, G. Orban de Xivry, S. P. Quanz, A. Reutlinger, G. Ruane, M. Riquelme, C. Soenke, M. Sterzik, A. Vigan, and T. de Zeeuw, "Imaging low-mass planets within the habitable zone of α Centauri," Nature Communications **12**(1), 1–7 (2021).

26. W.H.Cheng, "Technology development in breath microanalysis for clinical diagnosis," The Historical Journal **13**(2), 339–343 (1999).

27. M. Metsälä, "Optical techniques for breath analysis: from single to multi-species detection," Journal of Breath Research **12**(2), (2018).

28. T. A. Vincent and J. W. Gardner, "A low cost MEMS based NDIR system for the monitoring of carbon dioxide in breath analysis at ppm levels," Sensors and Actuators, B: Chemical **236**, 954–964 (2016).

29. A. P. M. Michel, S. Liakat, K. Bors, and C. F. Gmachl, "In vivo measurement of mid-infrared light scattering from human skin," Biomedical Optics Express **4**(4), 520 (2013).

30. B. Henderson, A. Khodabakhsh, M. Metsälä, I. Ventrillard, F. M. Schmidt, D. Romanini, G. A. D. Ritchie, S. te Lintel Hekkert, R. Briot, T. Risby, N. Marczin, F. J. M. Harren, and S. M. Cristescu, "Laser spectroscopy for breath analysis: towards clinical implementation," Applied Physics B: Lasers and Optics **124**(8), 1–21 (2018).

31. W. Demtröder, *Laser Spectroscopy 2: Experimental Techniques, Fifth Edition* (Springer-Verlag Berlin Heidelberg, 2015).

32. N. Picqué and T. W. Hänsch, "Frequency comb spectroscopy," Nature Photonics **13**(3), 146–157 (2019).

33. A. Schliesser, N. Picqué, and T. W. Hänsch, "Mid-infrared frequency combs," Nature Photonics **6**(7), 440–449 (2012).

34. S. Schiller, "Spectrometry with frequency combs," Optics Letters **27**(9), 766 (2002).

35. A. Schliesser, M. Brehm, F. Keilmann, and D. W. van der Weide, "Frequency-comb infrared spectrometer for rapid, remote chemical sensing," Optics Express **13**(22), 9029 (2005).

36. S. A. Diddams, K. Vahala, and T. Udem, "Optical frequency combs: Coherently uniting the electromagnetic spectrum," Science **369**(6501), (2020).

37. J. L. Hall, "Nobel lecture: Defining and measuring optical frequencies," Reviews of Modern Physics **78**(4), 1279–1295 (2006).

38. D. J. Jones, S. A. Diddams, J. K. Ranka, A. Stentz, R. S. Windeler, J. L. Hall, and S. T. Cundiff, "Carrier-envelope phase control of femtosecond mode-locked lasers and direct optical frequency synthesis," Science **288**(5466), 635–639 (2000).

39. R. Paschotta, A. Schlatter, S. C. Zeller, H. R. Telle, and U. Keller, "Optical phase noise and carrier-envelope offset noise of mode-locked lasers," Applied Physics B: Lasers and Optics **82**(2 SPEC. ISS.), 265–273 (2006).

40.   E. Benkler, H. R. Telle, A. Zach, and F. Tauser, "Circumvention of noise contributions in fiber laser based frequency combs," Optics Express **13**(15), 5662 (2005).

41.   D. E. Spence, P. N. Kean, and W. Sibbett, "60-fsec pulse generation from a self-mode-locked Ti : sapphire laser," Optics Letters **16**(1), 42–44 (1991).

42.   T. M. Fortier, A. Bartels, and S. A. Diddams, "Octave-spanning Ti:sapphire laser with a repetition rate >1 GHz for optical frequency measurements and comparisons," Optics Letters **31**(7), 1011 (2006).

43.   F. L. Hong, K. Minoshima, A. Onae, H. Inaba, H. Matsumoto, T. Sugiura, and M. Yoshida, "Broad-spectrum frequency comb generation and carrier-envelope offset frequency measurement using the second harmonic generation of a mode-locked fiber laser," OSA Trends in Optics and Photonics Series **88**(17), 926–927 (2003).

44.   S. A. Diddams, "The evolving optical frequency comb [Invited]," Journal of the Optical Society of America B **27**(11), B51 (2010).

45.   M. E. Fermann and I. Hartl, "Ultrafast fibre lasers," Nature Photonics **7**(11), 868–874 (2013).

46.   M. Kourogi, N. Ken'ichi, and M. Ohtsu, "Wide-Span Optical Frequency Comb Generator for Accurate Optical Frequency Difference Measurement," IEEE Journal of Quantum Electronics **29**(10), 2693–2701 (1993).

47.   I. Morohashi, T. Sakamoto, H. Sotobayashi, T. Kawanishi, I. Hosako, and M. Tsuchiya, "Widely repetition-tunable 200 fs pulse source using a Mach–Zehnder-modulator-based flat comb generator and dispersion-flattened dispersion-decreasing fiber," Optics Letters **33**(11), 1192 (2008).

48.   K. Beha, D. Cole, P. Del'Haye, A. Coillet, S. Diddams, and S. Papp, "Electronic synthesis of light," Optica **4**(4), 406 (2017).

49.   A. G. Griffith, R. K. W. Lau, J. Cardenas, Y. Okawachi, A. Mohanty, C. B. Poitras, A. L. Gaeta, and M. Lipson, "Silicon-chip mid-infrared frequency comb generation," Nature Communications **6**(6299), 1–5 (2014).

50.   B. Kuyken, T. Ideguchi, S. Holzner, M. Yan, T. W. Hänsch, J. Van Campenhout, P. Verheyen, S. Coen, F. Leo, R. Baets, G. Roelkens, and N. Picqué, "An octave-spanning mid-infrared frequency comb generated in a silicon nanophotonic wire waveguide," Nature Communications **6**, 1–6 (2015).

51.   L. C. Sinclair, J. D. Deschênes, L. Sonderhouse, W. C. Swann, I. H. Khader, E. Baumann, N. R. Newbury, and I. Coddington, "Invited Article: A compact optically coherent fiber frequency comb," Review of Scientific Instruments **86**(8), (2015).

52.   A. Klenner, A. S. Mayer, A. R. Johnson, K. Luke, M. R. E. Lamont, Y. Okawachi, M. Lipson, A. L. Gaeta, and U. Keller, "Gigahertz frequency comb offset stabilization based on supercontinuum generation in silicon nitride waveguides," Optics Express **24**(10), 11043 (2016).

53.   C. Langrock, M. M. Fejer, I. Hartl, and M. E. Fermann, "Generation of octave-spanning spectra inside reverse-proton-exchanged periodically poled lithium niobate waveguides," Optics Letters **32**(17), 2478 (2007).

54.   T. Fortier and E. Baumann, "20 Years of Developments in Optical Frequency Comb Technology and Applications," Communications Physics **2**(1), 1–16 (2019).

55. T. J. Kippenberg, R. Holzwarth, and S. A. Diddams, "Microresonator-based optical frequency combs," Science **332**(6029), 555–559 (2011).

56. V. Brasch, M. Geiselmann, T. Herr, G. Lihachev, M. H. P. Pfeiffer, M. L. Gorodetsky, and T. J. Kippenberg, "Photonic chip based optical frequency comb using soliton induced cherenkov radiation," Science (2014).

57. E. Obrzud, S. Lecomte, and T. Herr, "Temporal solitons in microresonators driven by optical pulses," Nature Photonics **11**(9), 600–607 (2017).

58. Z. Gong, A. Bruch, M. Shen, X. Guo, H. Jung, L. Fan, X. Liu, L. Zhang, J. Wang, J. Li, J. Yan, and H. X. Tang, "High-fidelity cavity soliton generation in crystalline AlN micro-ring resonators," Optics Letters **43**(18), 4366 (2018).

59. B. Shen, L. Chang, J. Liu, H. Wang, Q. F. Yang, C. Xiang, R. N. Wang, J. He, T. Liu, W. Xie, J. Guo, D. Kinghorn, L. Wu, Q. X. Ji, T. J. Kippenberg, K. Vahala, and J. E. Bowers, "Integrated turnkey soliton microcombs," Nature **582**(7812), 365–369 (2020).

60. B. Stern, X. Ji, Y. Okawachi, A. L. Gaeta, and M. Lipson, "Battery-operated integrated frequency comb generator," Nature **562**(7727), 401–405 (2018).

61. I. A. N. C. Coddington, N. A. N. Ewbury, and W. I. S. Wann, "Dual-comb spectroscopy," Optica **3**(4), (2016).

62. A. Dutt, C. Joshi, X. Ji, J. Cardenas, Y. Okawachi, K. Luke, A. L. Gaeta, and M. Lipson, "On-chip dual-comb source for spectroscopy," Science Advances **4**(3), 1–10 (2018).

63. T. Ideguchi, A. Poisson, G. Guelachvili, N. Picqué, and T. W. Hänsch, "Adaptive real-time dual-comb spectroscopy," Nature communications **5**, 3375 (2014).

64. M. Yu, Y. Okawachi, A. G. Griffith, N. Picqué, M. Lipson, and A. L. Gaeta, "Silicon-chip-based mid-infrared dual-comb spectroscopy," Nature Communications **9**(1), 6–11 (2018).

65. . H. Guo, W. Weng, J. Liu, F. Yang, W. Hänsel, C. S. Brès, L. Thévenaz, R.Holzwarth, T. J. Kippenberg, "Nanophotonic supercontinuum-based mid-infrared dual-comb spectroscopy," Optica **7**(9), 1181–1188 (2020).

66. M. Razeghi, N. Bandyopadhyay, Y. Bai, Q. Lu, and S. Slivken, "Recent advances in mid infrared (3-5μm) Quantum Cascade Lasers," Optical Materials Express **3**(11), 1872 (2013).

67. S. Borri, G. Insero, G. Santambrogio, D. Mazzotti, F. Cappelli, I. Galli, G. Galzerano, M. Marangoni, P. Laporta, V. Di Sarno, L. Santamaria, P. Maddaloni, and P. De Natale, "High-precision molecular spectroscopy in the mid-infrared using quantum cascade lasers," Applied Physics B: Lasers and Optics **125**(1), 1–9 (2019).

68. I. Vurgaftman, C. L. Canedy, C. S. Kim, M. Kim, W. W. Bewley, J. R. Lindle, J. Abell, and J. R. Meyer, "Mid-infrared interband cascade lasers operating at ambient temperatures," New Journal of Physics **11**, (2009).

69. L. A. Sterczewski, J. Westberg, M. Bagheri, C. Frez, I. Vurgaftman, C. L. Canedy, W. W. Bewley, C. D. Merritt, C. S. Kim, M. Kim, J. R. Meyer, and G. Wysocki, "Mid-infrared dual-comb spectroscopy with interband cascade lasers," Optics Letters **44**(8), 2113 (2019).

70. K. F. Lee, C. Mohr, J. Jiang, P. G. Schunemann, K. L. Vodopyanov, and M. E. Fermann,

"Midinfrared frequency comb from self-stable degenerate GaAs optical parametric oscillator," Optics Express **23**(20), 26596 (2015).

71. N. Leindecker, A. Marandi, R. L. Byer, and K. L. Vodopyanov, "Broadband degenerate OPO for mid-infrared frequency comb generation," Optics Express **19**(7), 6296 (2011).

72. J. Y. Degang Xu, Jiaxin Zhang, Yixin He, Yuye Wang, K. Z. Yangwu Guo, Chao Yan, Longhuang Tang, Jining Li, and A. J. Y. Yicheng Wu, "High-energy, tunable, long-wave mid-infrared optical parametric oscillator based on BaGa$_4$Se$_7$ crystal," Optics Letters **45**(18), 18–21 (2020).

73. A. Ruehl, A. Gambetta, I. Hartl, M. E. Fermann, K. S. E. Eikema, and M. Marangoni, "Widely-tunable mid-infrared frequency comb source based on difference frequency generation," Optics Letters **37**(12), 2232 (2012).

74. F. C. Cruz, D. L. Maser, T. Johnson, G. Ycas, A. Klose, L. C. Sinclair, I. Coddington, N. R. Newbury, and S. A. Diddams, "Mid-infrared optical frequency combs based on difference frequency generation for dual-comb spectroscopy," Optics Express **23**(20), 26814–26824 (2015).

75. C. W. Rudy, A. Marandi, K. L. Vodopyanov, and R. L. Byer, "Octave-spanning supercontinuum generation in in situ tapered As$_2$S$_3$ fiber pumped by a thulium-doped fiber laser," Optics Letters **38**(15), 2865 (2013).

76. Jean-Christophe Gauthier, "Mid-IR supercontinuum from 2.4 to 5.4 μm in a low loss fluoroindate fiber," Nature Photonics **6**(1), 165–168 (2018).

77. D. Jayasuriya, C. R. Petersen, D. Furniss, C. Markos, Z. Tang, M. S. Habib, O. Bang, T. M. Benson, and A. B. Seddon, "Mid-IR supercontinuum generation in birefringent, low loss, ultra-high numerical aperture Ge-As-Se-Te chalcogenide step-index fiber," Optical Materials Express **9**(6), 2617 (2019).

78. L. Yang, B. Zhang, K. Yin, T. Wu, Y. Zhao, and J. Hou, "High-power mid-infrared supercontinuum generation in a fluoroindate fiber with over 2 W power beyond 3.8 μm," Optics Express **6**(5), 417 (2018).

79. T. S. Saini, T. H. Tuan, T. Suzuki, and Y. Ohishi, "Coherent Mid-IR Supercontinuum Generation using Tapered Chalcogenide Step-Index Optical Fiber: Experiment and modelling," Scientific Reports **10**(1), 1–9 (2020).

80. N. Singh, D. D. Hudson, Y. Yu, C. Grillet, S. D. Jackson, A. Casas-Bedoya, A. Read, P. Atanackovic, S. G. Duvall, S. Palomba, B. Luther-Davies, S. Madden, D. J. Moss, and B. J. Eggleton, "Mid infrared supercontinuum generation from 2 to 6 μm in a silicon nanowire," Optica **2**(9), 797 (2015).

81. J. M. Chávez Boggio, A. Ortega Moñux, D. Modotto, T. Fremberg, D. Bodenmüller, D. Giannone, M. M. Roth, T. Hansson, S. Wabnitz, E. Silvestre, and L. Zimmermann, "Dispersion-optimized multicladding silicon nitride waveguides for nonlinear frequency generation from ultraviolet to mid-infrared," Journal of the Optical Society of America B **33**(11), 2402 (2016).

82. J. Wei, C. Ciret, M. Billet, F. Leo, B. Kuyken, and S. P. Gorza, "Supercontinuum Generation Assisted by Wave Trapping in Dispersion-Managed Integrated Silicon Waveguides," Physical Review Applied **14**(5), 1 (2020).

83. S. May, M. Clerici, and M. Sorel, "Supercontinuum generation in dispersion

engineered AlGaAs-on-insulator waveguides," Scientific Reports **11**(1), 1–7 (2021).

84. J. A. Black, D. R. C. Richelle Streater, Kieran F. Lamee, and and S. B. P. Su-Peng Yu, "Group-velocity-dispersion engineering of tantala integrated photonics," Optics Letters **46**(4), 817–820 (2021).

85. J. Dudley and T. Roy, *Supercontinum Generation in Optical Fibers* (Cambridge University Press, 2010).

86. R.R. Alfano and S.L. Shapiro, "Emission in the region 4000 to 7000Å via four-photon coupling in glass," Physical Review Letters **24**(11), 584–588 (1970).

87. J. M. Dudley, G. Genty, and S. Coen, "Supercontinuum generation in photonic crystal fiber," Reviews of Modern Physics **78**(4), 1135–1184 (2006).

88. A. Karabchevsky, A. Katiyi, A. S. Ang, and A. Hazan, "On-chip nanophotonics and future challenges," Nanophotonics **9**(12), 3733–3753 (2020).

89. C. R. Petersen, U. Møller, I. Kubat, B. Zhou, S. Dupont, J. Ramsay, T. Benson, S. Sujecki, N. Abdel-Moneim, Z. Tang, D. Furniss, A. Seddon, and O. Bang, "Mid-infrared supercontinuum covering the 1.4-13.3 µm molecular fingerprint region using ultra-high NA chalcogenide step-index fibre," Nature Photonics **8**(11), 830–834 (2014).

90. D. D. Hudson, S. Antipov, L. Li, I. Alamgir, T. Hu, M. El Amraoui, Y. Messaddeq, M. Rochette, S. D. Jackson, and A. Fuerbach, "Toward all-fiber supercontinuum spanning the mid-infrared," Optica **4**(10), 1163 (2017).

91. I. Savelii, O. Mouawad, J. Fatome, B. Kibler, F. Désévédavy, G. Gadret, J. C. Jules, P. Y. Bony, H. Kawashima, W. Gao, T. Kohoutek, T. Suzuki, Y. Ohishi, and F. Smektala, "Mid-infrared 2000nm bandwidth supercontinuum generation in suspended-core chalcogenide and tellurite optical fibers," Optics Express **20**(24), 2641–2645 (2013).

92. Z. Zhao, B. Wu, X. Wang, Z. Pan, Z. Liu, P. Zhang, X. Shen, Q. Nie, S. Dai, and R. Wang, "Mid-infrared supercontinuum covering 2.0–16 µm in a low-loss telluride single-mode fiber," Laser and Photonics Reviews **11**(2), 2–6 (2017).

93. S. A. Rezvani, Y. Nomura, K. Ogawa, and T. Fuji, "Generation and characterization of supercontinuum in polarization maintained ZBLAN fiber using femtosecond 2 µm pulses," Optics Express **27**(17), 24499–24511 (2019).

94. C. Yao, Z. Jia, Z. Li, S. Jia, Z. Zhao, L. Zhang, Y. Feng, G. Qin, Y. Ohishi, and W. Qin, "High-power mid-infrared supercontinuum laser source using fluorotellurite fiber," Optica **5**(10), 1264 (2018).

95. B. Dong, D. L. Kwong, C. Lee, P. G. Q. Lo, X. Luo, and K. W. Ang, "Aluminum Nitride on Insulator (AlNOI) Platform for Mid-Infrared photonics," Optics Letters **44**(1), 73–76 (2019).

96. J. Lu, L. Shao, Y. Okawachi, A. L. Gaeta, and M. Lončar, "Ultraviolet to mid-infrared supercontinuum generation in single-crystalline aluminum nitride waveguides," Optics Letters **45**(16), 4499–4502 (2020).

97. M. L. Mengjie Yo, Linbo Shao, Yoshitomo Okawachi, Alexander L. Gaeta, "Ultraviolet to Mid-Infrared Supercontinuum Generation in Lithium-Niobate Waveguides," in *Conference on Lasers and Electro-Optics (CLEO) (Optical Society of America, 2020),*

p. STu4H.1. (2020).

98. V. V. H. Saghaei, "Broadband mid-infrared supercontinuum generation in dispersion-engineered silicon-on-insulator waveguide," Journal of the Optical Society of America B **36**(2), 193–202 (2019).

99. R. K. W. Lau, M. R. E. Lamont, A. G. Griffith, Y. Okawachi, M. Lipson, and A. L. Gaeta, "Octave-spanning mid-infrared supercontinuum generation in silicon nanowaveguides," Optics Letters **39**(15), 4518 (2014).

100. R. Kou, T. Hatakeyama, J. Horng, J.-H. Kang, Y. Wang, X. Zhang, and F. Wang, "Mid-IR broadband supercontinuum generation from a suspended silicon waveguide," Optics Letters **43**(6), 1387 (2018).

101. X. Liu, B. Zhou, M. Bache, C. J. Kruckel, A. Fulop, and V. Torres-Company, "Octave-spanning supercontinuum generation in a silicon-rich nitride waveguide," Optics Letters **41**(12), 1–4 (2016).

102. M. Sinobad, C. Monat, B. Luther-davies, P. Ma, S. Madden, D. J. Moss, A. Mitchell, D. Allioux, R. Orobtchouk, S. Boutami, J.-M. Hartmann, J.-M. Fedeli, and C. Grillet, "Mid-infrared octave spanning supercontinuum generation to 85 μm in silicon-germanium waveguides," Optica **5**(4), 360 (2018).

103. M. Montesinos-Ballester, C. Lafforgue, J. Frigerio, A. Ballabio, V. Vakarin, Q. Liu, J. M. Ramirez, X. Le Roux, D. Bouville, A. Barzaghi, C. Alonso-Ramos, L. Vivien, G. Isella, and D. Marris-Morini, "On-Chip Mid-Infrared Supercontinuum Generation from 3 to 13 μm Wavelength," ACS Photonics **7**(12), 3423–3429 (2020).

104. A. Della Torre, M. Sinobad, R. Armand, B. Luther-Davies, P. Ma, S. Madden, A. Mitchell, D. J. Moss, J. M. Hartmann, V. Reboud, J. M. Fedeli, C. Monat, and C. Grillet, "Mid-infrared supercontinuum generation in a low-loss germanium-on-silicon waveguide," APL Photonics **6**(1), (2021).

105. R. Halir, Y. Okawachi, J. S. Levy, M. A. Foster, M. Lipson, and A. L. Gaeta, "Ultrabroadband supercontinuum generation in a CMOS-compatible platform," Optics Letters **37**(10), 1685 (2012).

106. A. L. G. A.R. Johnson, A.S. Mayer, A. Klenner, K. Luke, E.S. Lamb, M.R.E. Lamont, C. Joshi, Y. Okawachi, F.W.Wise, M. Lipson, U.Keller, "Octave-spanning coherent supercontinuum generation in a silicon nitride waveguide," Optics Letters **40**(21), 5117–5120 (2015).

107. . M.A.G. Porcel, F. Schepers, J.P.Epping, T.Hellwig, M.Hoekman, R.G.Heideman, P.J.M. Van der Slot, C.J.Lee, R.Schmidt, R.Bratschitsch, C.Fallnich, K.J. Boller, "Two-octave spanning supercontinuum generation in stoichiometric silicon nitride waveguides pumped at telecom wavelengths," Optics Express **25**(2), 1596–1603 (2017).

108. H. Zhao, B. Kuyken, F. Leo, S. Clemmen, E. Brainis, G. Roelkens, and R. Baets, "Visible-to-near-infrared octave spanning supercontinuum generation in a silicon nitride waveguide," Optics Letters **40**(10), 2177–2180 (2015).

109. J. P. Epping, T. Hellwig, M. Hoekman, R. Mateman, A. Leinse, R. G. Heideman, A. van Rees, P. J. M. van der Slot, C. J. Lee, C. Fallnich, and K.-J. Boller, "On-chip visible-to-infrared supercontinuum generation with more than 495 THz spectral bandwidth," Optics Express **23**(15), 19596 (2015).

110. H. Guo, C. Herkommer, A. Billat, D. Grassani, C. Zhang, M. H. P. Pfeiffer, W. Weng, C.

S. Brès, and T. J. Kippenberg, "Mid-infrared frequency comb via coherent dispersive wave generation in silicon nitride nanophotonic waveguides," Nature Photonics **12**(6), 330–335 (2018).

111. T. Wang, N. Venkatram, J. Gosciniak, Y. Cui, G. Qian, W. Ji, and D. T. H. Tan, "Multi-photon absorption and third-order nonlinearity in silicon at mid-infrared wavelengths," Optics Express **21**(26), 32192 (2013).

112. R. Soref, "Mid-infrared photonics in silicon and germanium," Nature Photonics **4**(8), 495–497 (2010).

113. D. T. H. Tan, K. J. A. Ooi, and D. K. T. Ng, "Nonlinear optics on silicon-rich nitride—a high nonlinear figure of merit CMOS platform [Invited]," Photonics Research **6**(5), B50 (2018).

114. C. J. Krückel, A. Fülöp, P. A. Andrekson, and V. Torres-Company, "Bandgap engineering in nonlinear silicon nitride waveguides," Optics Express **25**(13), 15370–15380 (2017).

115. K. Ikeda, R. E. Saperstein, N. Alic, and Y. Fainman, "Thermal and Kerr nonlinear properties of plasma-deposited silicon nitride/ silicon dioxide waveguides," Optics Express **16**(17), 12987 (2008).

116. M. H. P. Pfeiffer, A. Kordts, V. Brasch, M. Zervas, M. Geiselmann, J. D. Jost, and T. J. Kippenberg, "Photonic Damascene process for integrated high-Q microresonator based nonlinear photonics," Optica **3**(1), 20 (2016).

117. G. Agrawal, *Nonlinear Fiber Optics-Fifth Edition* (2013).

118. N. Akhmediev and M. Karlsson, "Cherenkov radiation emitted by solitons in optical fibers," Physical Review A **51**(3), 2602–2607 (1995).

119. K. C. Cossel, E. M. Waxman, I. A. Finneran, G. A. Blake, J. Ye, and N. R. Newbury, "Gas-phase broadband spectroscopy using active sources progress, status, and applications," Journal of optical society of America B **34**(1), 104 (2017).

120. K. Okamoto, *Fundamentals of Optical Waveguides, Second Edition (Optics and Photonics Series)* (2005).

121. D. Marcuse, *Theory of Dielectric Optical Waveguides* (Academic Press, 2013).

122. Jacques Bures, *Guided Optics:Optical Fibers and All Fiber Components* (Wiley, 2009).

123. W. H. Reeves, D. V. Skryabin, F. Biancalana, J. C. Knight, P. S. J. Russell, F. G. Omenetto, A. Efimov, and A. J. Taylor, "Transformation and control of ultra-short pulses in dispersion-engineered photonic crystal fibres," Nature **424**(6948), 511–515 (2003).

124. S. Kim, K. Han, C. Wang, J. A. Jaramillo-Villegas, X. Xue, C. Bao, Y. Xuan, D. E. Leaird, A. M. Weiner, and M. Qi, "Dispersion engineering and frequency comb generation in thin silicon nitride concentric microresonators," Nature Communications **8**(1), (2017).

125. J. M. Dudley, *Supercontinuum Generation in Optical Fibers* (Cambridge University Press, 2013), **53**(9).

126. M. Karpov, H. Guo, A. Kordts, V. Brasch, M. H. P. Pfeiffer, M. Zervas, M. Geiselmann, and T. J. Kippenberg, "Raman Self-Frequency Shift of Dissipative Kerr Solitons in

an Optical Microresonator," Physical Review Letters **116**(10), 1–5 (2016).

127. G. New, *Introduction to Nonlinear Optics* (2011).

128. R. W. Boyd, *Nonlinear Optics* (2007).

129. A. Billat, D. Grassani, M. H. P. Pfeiffer, S. Kharitonov, T. J. Kippenberg, and C. S. Brès, "Large second harmonic generation enhancement in Si_3N_4 waveguides by all-optically induced quasi-phase-matching," Nature Communications **8**(1), 1–7 (2017).

130. M. D. Maiden, D. V. Anderson, N. A. Franco, G. A. El, and M. A. Hoefer, "Solitonic Dispersive Hydrodynamics: Theory and Observation," Physical Review Letters **120**(14), 144101 (2018).

131. A. Constantin, "On the relevance of soliton theory to tsunami modelling," Wave Motion **46**(6), 420–426 (2009).

132. T. Lakoba, D. Mitra, and G. Melikidze, "Relativistic charge solitons created due to non-linear Landau damping: A candidate for explaining coherent radio emission in pulsars," Monthly Notices of the Royal Astronomical Society **480**(4), 4526–4543 (2018).

133. T. Heimburg and A. D. Jackson, "On soliton propagation in biomembranes and nerves," Proceedings of the National Academy of Sciences of the United States of America **102**(28), 9790–9795 (2005).

134. A. I. Adamu, M. S. Habib, C. R. Petersen, J. E. A. Lopez, B. Zhou, A. Schülzgen, M. Bache, R. Amezcua-Correa, O. Bang, and C. Markos, "Deep-UV to Mid-IR Supercontinuum Generation driven by Mid-IR Ultrashort Pulses in a Gas-filled Hollow-core Fiber," Scientific Reports **9**(1), 1–9 (2019).

135. C.-M. Chen and P. L. Kelley, "Nonlinear pulse compression in optical fibers: scaling laws and numerical analysis," Journal of the Optical Society of America B **19**(9), 1961 (2002).

136. K. E. Webb, Y. Q. Xu, M. Erkintalo, and S. G. Murdoch, "Generalized dispersive wave emission in fiber optics," Optics Letters **38**(2), 151–153 (2013).

137. S. Roy, D. Ghosh, S. K. Bhadra, and G. P. Agrawal, "Role of dispersion profile in controlling emission of dispersive waves by solitons in supercontinuum generation," Optics Communications **283**(15), 3081–3088 (2010).

138. W. J. Tomlinson, R. H. Stolen, and A. M. Johnson, "Optical wave breaking of pulsess in nonlinear optical fibers," Optics Letters **10**(9), 457–459 (1985).

139. W. Demtröder and K. F. Lim, *Laser Spectroscopy 1: : Basic Principles* (2012).

140. L. S. Rothman, "History of the HITRAN Database," Nature Reviews Physics (2021).

141. R. J. Hargreaves, I. E. Gordon, M. Rey, A. V. Nikitin, V. G. Tyuterev, R. V. Kochanov, and L. S. Rothman, "An accurate, extensive, and practical line list of methane for the HITEMP database," The Astrophysical Journal Supplement series **247**(19), 55 (2020).

142. B. H. Armstrong, "Spectrum line profiles:the Voigt function," Journal of Quantitative Spectroscopy and Radiative Transfer **7**(2), 61–88 (1967).

143. F. Schmidt, *Laser-Based Absorption Spectrometry* (2007).

144. E. Tagkoudi, D. Grassani, H. Guo, C. Herkommer, T. Kippenberg, and C.-S. Bres, "Efficient mid-infrared dispersive wave generation in dispersion-engineered Si_3N_4 waveguides pumped at 2 μm," in *2018 Conference on Lasers and Electro-Optics, CLEO 2018 - Proceedings* (2018).

145. D. Grassani, E. Tagkoudi, H. Guo, C. Herkommer, F. Yang, T. J. Kippenberg, and C. S. Brès, "Mid infrared gas spectroscopy using efficient fiber laser driven photonic chip-based supercontinuum," Nature Communications **10**(1), (2019).

146. S. Roy, S. K. Bhadra, and G. P. Agrawal, "Effects of higher-order dispersion on resonant dispersive waves emitted by solitons," Optics Letters **34**(13), 2072–2074 (2009).

147. S. Roy, S. K. Bhadra, and G. P. Agrawal, "Dispersive waves emitted by solitons perturbed by third-order dispersion inside optical fibers," Physical Review A - Atomic, Molecular, and Optical Physics **79**(2), 1–6 (2009).

148. R. Kitamura, L. Pilon, and M. Jonasz, "Optical constants of silica glass from extreme ultraviolet to far infrared at near room temperature," Applied Optics **46**(33), 8118–8133 (2007).

149. L. Zhang, Q. Lin, Y. Yue, Y. Yan, R. G. Beausoleil, and A. E. Willner, "Silicon waveguide with four zero-dispersion wavelengths and its application in on-chip octave-spanning supercontinuum generation," Optics Express **20**(2), 1685 (2012).

150. M. H. P. Pfeiffer, A. Kordts, V. Brasch, M. Zervas, M. Geiselmann, J. D. Jost, and T. J. Kippenberg, "Photonic Damascene process for integrated high-Q microresonator based nonlinear photonics," Optica **3**(1), 20 (2016).

151. E. Tagkoudi, D. Grassani, F. Yang, H. Guo, T. Kippenberg, and C.-S. Bres, "Gas Spectroscopy Using Low Threshold Mid-Infrared Radiation Generated in Si_3N_4 Waveguides," in *2019 Conference on Lasers and Electro-Optics, CLEO 2019 - Proceedings* (2019).

152. E. Tagkoudi, D. Grassani, F. Yang, and C. S. Brès, "Multi-gas spectroscopy using tailored mid-IR dispersive wave generated in Si_3N_4 waveguide," OSA High-brightness Sources and Light-driven Interactions Congress 2020 (EUVXRAY, HILAS, MICS), OSA 2020 **2020**(c), 7–8 (2020).

153. E. Tagkoudi, D. Grassani, F. Yang, C. Herkommer, T. Kippenberg, and C.-S. Brès, " Parallel gas spectroscopy using mid-infrared supercontinuum from a single Si_3N_4 waveguide ," Optics Letters **45**(8), 2195 (2020).

154. J. Hodgkinson and R. P. Tatam, "Optical gas sensing: A review," Measurement Science and Technology **24**(1), (2013).

155. P. Laj, J. Klausen, M. Bilde, C. Plaß-Duelmer, G. Pappalardo, C. Clerbaux, U. Baltensperger, J. Hjorth, D. Simpson, S. Reimann, P. F. Coheur, A. Richter, M. De Mazière, Y. Rudich, G. McFiggans, K. Torseth, A. Wiedensohler, S. Morin, M. Schulz, J. D. Allan, J. L. Attié, I. Barnes, W. Birmili, J. P. Cammas, J. Dommen, H. P. Dorn, D. Fowler, S. Fuzzi, M. Glasius, C. Granier, M. Hermann, I. S. A. Isaksen, S. Kinne, I. Koren, F. Madonna, M. Maione, A. Massling, O. Moehler, L. Mona, P. S. Monks, D. Müller, T. Müller, J. Orphal, V. H. Peuch, F. Stratmann, D. Tanré, G. Tyndall, A. Abo Riziq, M. Van Roozendael, P. Villani, B. Wehner, H. Wex, and A. A. Zardini, "Measuring atmospheric composition change," Atmospheric Environment **43**(33), 5351–5414 (2009).

156. M. L. Smith, E. A. Kort, A. Karion, C. Sweeney, S. C. Herndon, and T. I. Yacovitch, "Airborne Ethane Observations in the Barnett Shale: Quantification of Ethane Flux and Attribution of Methane Emissions," Environmental Science and Technology **49**(13), 8158–8166 (2015).

157. Q. He, C. Zheng, H. Liu, Y. Wang, and F. K. Tittel, " A near-infrared gas sensor system based on tunable laser absorption spectroscopy and its application in CH_4 /C_2H_2 detection ," Quantum Sensing and Nano Electronics and Photonics XIV **10111**, 1011135 (2017).

158. E. Baumann, E. V. Hoenig, E. F. Perez, G. M. Colacion, F. R. Giorgetta, K. C. Cossel, G. Ycas, D. R. Carlson, D. D. Hickstein, K. Srinivasan, S. B. Papp, N. R. Newbury, and I. Coddington, "Dual-comb spectroscopy with tailored spectral broadening in Si_3N_4 nanophotonics," Optics Express **27**(8), 11869–11876 (2019).

159. M. C. Chan, S. H. Chia, T. M. Liu, T. H. Tsai, M. C. Ho, A. A. Ivanov, A. M. Zheltikov, J. Y. Liu, H. L. Liu, and C. K. Sun, "1.2- to 2.2-μm tunable Raman soliton source based on a Cr : Forsterite laser and a photonic-crystal fiber," IEEE Photonics Technology Letters **20**(11), 900–902 (2008).

160. N. R. Newbury, I. Coddington, and W. Swann, "Sensitivity of coherent dual-comb spectroscopy," Optics Express **18**(8), 7929 (2010).

161. F. Adler, P. Masłowski, A. Foltynowicz, K. C. Cossel, T. C. Briles, I. Hartl, and J. Ye, "Mid-infrared Fourier transform spectroscopy with a broadband frequency comb," Optics Express **18**(21), 21861 (2010).

162. E. Tagkoudi, C. G. Amiot, G. Genty, and C.-S. Brès, "Extreme polarization-dependent supercontinuum generation in an uncladded silicon nitride waveguide," Optics Express **29**(14), 21348 (2021).

163. A. M. Heidt, "Pulse-preserving flat-top supercontinuum generation in all-normal dispersion photonic crystal fibers," JOSA B **27**(3), 550–559 (2010).

164. L. Zhang, Y. Yan, Y. Yue, Q. Lin, O. Painter, R. G. Beausoleil, and A. E. Willner, "On-chip two-octave supercontinuum generation by enhancing self-steepening of optical pulses," Optics Express **19**(12), 11584 (2011).

165. M. Klimczak, G. Soboń, K. Abramski, and R. Buczyński, "Spectral coherence in all-normal dispersion supercontinuum in presence of Raman scattering and direct seeding from sub-picosecond pump," Optics Express **22**(26), 31635 (2014).

166. S. Xing, S. Kharitonov, J. Hu, and C.-S. Brès, "Linearly chirped mid-infrared supercontinuum in all-normal-dispersion chalcogenide photonic crystal fibers," Optics Express **26**(15), 19627 (2018).

167. T. Le Canh, V. T. Hoang, H. Le Van, D. Pysz, V. C. Long, T. B. Dinh, D. T. Nguyen, Q. H. Dinh, M. Klimczak, R. Kasztelanic, J. Pniewski, R. Buczynski, and K. X. Dinh, "Supercontinuum generation in all-normal dispersion suspended core fiber infiltrated with water," Optical Materials Express **10**(7), 1733 (2020).

168. S. Christensen, Z. Ye, M. Bache, and V. T. Company, "Octave-Spanning Frequency Comb Generation in All-Normal-Dispersion Silicon-Rich Silicon Nitride Waveguide," Conference Proceedings - Lasers and Electro-Optics Society Annual Meeting-CLEO (2020).

169. L. E. Hooper, P. J. Mosley, A. C. Muir, W. J. Wadsworth, and J. C. Knight, "Coherent

supercontinuum generation in photonic crystal fiber with all-normal group velocity dispersion," Optics Express **19**(6), 4902–4907 (2011).

170. J. B. Mcmanus, P. L. Kebabian, and M. S. Zahniser, "Astigmatic mirror multipass absorption cells for long path length spectroscopy," Applied Optics **34**(18), (1995).

171. B. Tuzson, M. Mangold, H. Looser, A. Manninen, and L. Emmenegger, "Compact multipass optical cell for laser spectroscopy," Optics Letters **38**(3), 257 (2013).

172. J. Liu, A. S. Raja, M. H. P. Pfeiffer, C. Herkommer, H. Guo, M. Zervas, M. Geiselmann, and T. J. Kippenberg, "Double inverse nanotapers for efficient light coupling to integrated photonic devices," Optics Letters **43**(14), 3200–3203 (2018).

173. K. Van Gasse, S. Uvin, V. Moskalenko, S. Latkowski, G. Roelkens, E. Bente, and B. Kuyken, "Recent Advances in the Photonic Integration of Mode-Locked Laser Diodes," IEEE Photonics Technology Letters **31**(23), 1870–1873 (2019).

174. E. Vissers, S. Poelman, C. O. de Beeck, K. Van Gasse, and B. Kuyken, "Hybrid integrated mode-locked laser diodes with a silicon nitride extended cavity," Optics Express **29**(10), 15013–15022 (2021).

175. J. M. Dudley and S. Coen, "Fundamental limits to few-cycle pulse generation from compression of broadband supercontinuum spectra generated in photonic crystal fiber," Optics Express **12**(11), 1111–1112 (2004).

176. D. T. H. Tan, "Optical pulse compression on a silicon chip-Effect of group velocity dispersion and free carriers," Applied Physics Letters **101**(21), 13–17 (2012).

177. J. W. Choi, B. U. Sohn, G. F. R. Chen, D. K. T. Ng, and D. T. H. Tan, "Soliton-effect optical pulse compression in CMOS-compatible ultra-silicon-rich nitride waveguides," APL Photonics **4**(11), (2019).

EIRINI TAGKOUDI

CONTACT INFORMATION

etagoudi@gmail.com
https://www.linkedin.com/in/eirini-tagkoudi
Skype: Eirini Tagkoudi

STRENGTHS

- **OPTICAL ENGINEERING**
- **LASER SYSTEMS**
- **EFFECTIVE COMMUNICATION**

Design and development of experimental setups for optical fiber and waveguide testing and characterization

High-power laser operation in CW and pulsed regimes

Intercultural communication in two languages, Scientific and technical writing, Scientific presentations

EDUCATION

2017 – 2021

Ph.D. in Photonics
Swiss Federal Institute of Technology (EPFL), Lausanne, Switzerland

2013 – 2015

Master of Science (M.Sc.) in Microelectronics and Optoelectronics
University of Crete, Department of Physics, Heraklion, Greece

2008 – 2013

Bachelor of Science (B.Sc.) in Physics
University of Patras, Department of Physics, Patras, Greece
– Major in Photonics

CORE EXPERIENCE

2017 – 2021

Photonic Systems Laboratory (PHOSL)
Swiss Federal Institute of Technology (EPFL)
Doctoral Thesis: "*Supercontinuum Generation in Silicon Nitride (Si_3N_4) Waveguides for Middle-infrared Spectroscopy*".
Design and development of versatile supercontinuum (SC) sources based on different designs of dispersion-engineered Si_3N_4 waveguides with applications in spectroscopy. A new type of compact, middle-infrared source that consists of a femtosecond 2 µm fiber laser and a 5 mm long chip has been developed. The on-chip generated mid-IR light can successfully detect the presence and the concentration of greenhouse gases such as methane, ethane, and acetylene. In addition, this device sets a new benchmark for efficiency with up to 35 % power conversion and milliwatt-level output powers.

2015 – 2016

Photonic Materials and Devices Laboratory (PMDL)
Foundation for Research and Technology-Hellas (FORTH) - Institute of Electronic Structure & Laser (IESL)
Research Assistant – Development of a power-routing photonic device based on a tapered multicore optical fiber and a magnetic fluid overlayer that exhibits magnetic field intensity and rotational sensitivity. Development of a pressure and humidity sensor based on fiber-Bragg grating (FBGs) inscription.

2013 – 2015

Master Thesis: "*Magneto-rheological devices in Microstructured Optical Fibers (MOFs)* ".

Design and development of magnetic field sensors based on ferrofluid infiltrated microstructured optical fibers (MOFs). Two different MOF designs have been used for the sensing devices: multicapillary and penta MOFs.

2011 –2012	**Laser, Nonlinear and Quantum Optics Laboratory (LNLQO-Lab)**
	Department of Physics, University of Patras & Institute of Chemical Engineering Sciences (ICE-HT)

<u>Bachelor Thesis:</u> "*Synthesis, Characterization, and Investigation of the Nonlinear Optical Response of Magnetic Iron Oxide Nanoparticles (MIONs) with polymeric shell through Z-Scan Technique*".

Experimental investigation and systematic measurements of the third-order nonlinear susceptibility $\chi^{(3)}$ of chemically synthesized polymer-coated magnetic iron oxide nanoparticles (MIONs) using the Z-Scan technique. Excitation with nanosecond and picosecond laser pulses at 532 nm and 1064 nm suggests that the synthesized MIONs constitute a promising nonlinear optical material.

ADDITIONAL EXPERIENCE

2017 – 2021	**Photonic Systems Laboratory (PHOSL), EPFL**
	– Teaching Assistant in Technologies de l'information course
	– Reviewing papers for scientific journals
2013 – 2015	**Photonic Materials and Devices Laboratory (PMDL), FORTH - IESL**
	– Co-supervised the thesis of an undergraduate student
	– Teaching Assistant in Advanced Physics Laboratory course

TECHNICAL EXPERTISE

RESEARCH TOOLS	**OPTICAL ENGINEERING**: Design and development of experimental setups for optical fiber and waveguide testing and characterization, Development of compact optical devices for novel applications
	LASER SYSTEMS: High-power ultrafast laser system operation & safety, Operation in continuous-wave (CW) and pulsed regimes, Free-space optical alignment, Use of optical measurement equipment for laser and device characterization (power meters, spectrometers, oscilloscopes, optical and RF spectrum analyzers, optical amplifiers, autocorrelators), Interferometry Techniques: Michelson and Mach-Zehnder interferometer building, Z-Scan Technique
	SPECTROSCOPY: Molecular fingerprinting using custom-made lasers, HITRAN database analysis
	INTEGRATED PHOTONICS: On-chip waveguide coupling, Exploiting nonlinear optical phenomena in silicon nitride platform, Design and development of on-chip light sources based on parametric wavelength conversion
	FIBER SENSING: Design and development of compact sensing devices based on microstructured optical fibers and optofluidics as well as tapered optical fiber magnetic field sensors, Fiber Bragg grating (FBG) sensors for humidity and pressure
	FIBER OPTICS: Optical fiber handling and processing (optical fiber stripping, cleaving, splicing, tapering, and connectorization), Fiber lasers, Optical fiber testing and characterization, Fiber Bragg Grating (FBG) inscription

CHARACTERIZATION TECHNIQUES: X-ray Diffraction (XRD), Dynamic Light Scattering (DLS), Scanning Electron Microscopy (SEM), Refractive Index measurements using Abbe refractometer

MATERIAL SYNTHESIS: Chemical synthesis of Magnetic Iron Oxide Nanoparticles (MIONs) coated with polymeric shell based on a hydrolytic precipitation reaction

PROGRAMMING & SOFTWARE	Matlab, C_{++} OriginLab, COMSOL Multiphysics Microsoft Office suite, Adobe suite
INTERPERSONAL SKILLS	SCIENCE COMMUNICATION: Communicating with a non-specialist audience and explaining complex scientific topics to the general public during the EPFL Open Days event, including displays and hands-on experiments with children EFFECTIVE COMMUNICATION: Strong presentation and public speaking skills, Intercultural communication in two languages TEAMWORK: Excellent collaboration with colleagues, sharing ideas for a common goal

LANGUAGES

- English (Excellent Knowledge, C1)
- Greek (Native)
- French (Basic Knowledge, A2)
- German (Basic Knowledge, A2)

PUBLICATIONS

PEER-REVIEWED JOURNAL ARTICLES

- **E.Tagkoudi**, C. Amiot, G.Genty, C.S.Brès, "*Extreme polarization-dependent supercontinuum generation in an uncladded silicon nitride waveguide*", **Optics Express**, vol. 29, 14, pp. 21348-21357, (2021)
- **E.Tagkoudi**, D.Grassani, F.Yang, C.Herkommer, T.J.Kippenberg, C.S.Brès, "*Parallel gas spectroscopy using mid-infrared supercontinuum from a single Si_3N_4 waveguide*", **Optics Letters**, vol. 45, 8, pp. 2195-2198, (2020), highlighted in the top 10 downloads in Optics Letters for April 2020
- D.Grassani, **E.Tagkoudi**, H.Guo, C.Herkommer, F.Yang, T.J.Kippenberg, C.S.Brès "*Mid-infrared gas spectroscopy using efficient fiber laser driven photonic chip-based supercontinuum*", **Nature Communications** vol. 10, no.1553, (2019)
- **E. Tagoudi**, K. Milenko and S. Pissadakis, "*Intercore Coupling Effects in Multicore Optical Fiber Tapers Using Magnetic Fluid Out-Claddings*", **Journal of Lightwave Technology**, vol. 34, 23, (2016), highlighted as the front cover of the Journal of Lightwave Technology IEEE/OSA, for the issues 21-24, (2016)

CONFERENCE PAPERS

- **E. Tagkoudi** et al., "*Extreme polarization dependent infrared supercontinuum generation in uncladded silicon nitride waveguide*", European Conference on Lasers and Electro-Optics (CLEO-Europe) (2021)
- **E. Tagkoudi** et al., "*Multi-gas spectroscopy using tailored mid-IR dispersive wave generated in Si_3N_4 waveguide*", High-brightness Sources and Light-driven Interactions Congress, (2020)
- **E. Tagkoudi** et al., "*Gas Spectroscopy Using Low Threshold Mid-Infrared Radiation Generated in Si_3N_4 Waveguides*", Conference on Lasers and Electro-Optics (CLEO), San Jose, CA, USA, (2019)
- **E. Tagkoudi** et al. "*Efficient mid-infrared dispersive wave generation in dispersion-engineered Si_3N_4 waveguides pumped at 2 μm*", *Conference on Lasers and Electro-Optics (CLEO),* San Jose, CA, USA, (2018)
- **E. Tagoudi** et al. "*Power coupling in multicore optical fiber tapers utilizing out-cladding ferrofluids*", SPIE Photonics Europe (pp. 98860G-98860G), International Society for Optics and Photonics, (2016)

- **E. Tagoudi** et al., "*Ferrofluid infiltrated multicapillary microstructured optical fibers for endoscopic applications*",European Conference on Lasers and Electro-Optics (CLEO-Europe), p. CH.P.26, OSA, (2015)

SCHOLARSHIPS & AWARDS

2018	Best Poster Award in EPFL Photonics Day
2013 –2015	Master Scholarships Program by the State Scholarships Foundation (I.K.Y.) within the National Strategic Reference Framework (NSRF 2007-2013)

PERSONAL DETAILS

- Date of birth: 14 July 1990
- Nationality: Greek
- Swiss driving license: Category B
- Swiss residence permit: Type B
- Activities: Running, Hiking, Pilates